WIND REVERSALS AND NON-OBERBECK-BOUSSINESQ EFFECTS IN RAYLEIGH-BÉNARD CONVECTION

Samenstelling promotiecommissie:

Prof. Dr. M. J. Peters (voorzitter)	Universiteit Twente
Prof. Dr. D. Lohse (promotor)	Universiteit Twente
Prof. Dr. S. Grossmann (co-promotor)	Phillips-Universität Marburg
Prof. Dr. G. Ahlers	University of California, Santa Barbara
Prof. Dr. H. J. H. Clercx	Technische Universiteit Eindhoven
Prof. Dr. Ir. J. W. M. Hilgenkamp	Universiteit Twente
Prof. Dr. Ir. A. A. van Steenhoven	Technische Universiteit Eindhoven
Prof. Dr. P. Tong	Hong Kong University
Prof. Dr. Ir. J. J. W. van der Vegt	Universiteit Twente

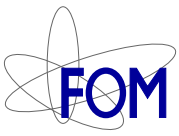

The research described in this thesis is part of the research program of the Stichting voor Fundamenteel Onderzoek der Materie (FOM), which is financially supported by the Nederlandse Organisatie voor Wetenschappelijk Onderzoek (NWO). It was carried out at the Physics of Fluids research group of the faculty of Science and Technology of the University of Twente.

Publisher:
Francisco Fontenele Araujo Jr.
University of Twente, Physics of Fluids
P.O. Box 217, 7500 AE
Enschede, The Netherlands
http://pof.tnw.utwente.nl

ISBN: 978-90-365-2491-9

WIND REVERSALS AND NON-OBERBECK-BOUSSINESQ EFFECTS IN RAYLEIGH-BÉNARD CONVECTION

PROEFSCHRIFT

ter verkrijging van
de graad van doctor aan de Universiteit Twente,
op gezag van de rector magnificus,
prof. dr. W. H. M. Zijm,
volgens besluit van het College voor Promoties
in het openbaar te verdedigen
op donderdag 7 juni 2007 om 15.00 uur

door

Francisco Fontenele Araujo Junior

geboren op 16 februari 1978

te Belo Horizonte, Brazilië.

Dit proefschrift is goedgekeurd door de promotor:

Prof. Dr. D. Lohse

en de co-promotor:

Prof. Dr. S. Grossmann

To my mother Helena and
to my sisters Sandra and Helenice.

Contents

1 Introduction

Convection, from the Latin *convehere* (to carry with), is the transport of a physical quantity by coupling with a velocity field. Thermal convection, in particular, is concerned with the interplay between *heat*, *buoyancy*, and *fluid motion*. A classical example is provided by the emissions of warm rising and cold falling fluid in a container heated from below and cooled from above. Depending on the strength of the thermal driving, such emissions may even induce a *large-scale circulation* of fluid. Some basic questions arising in this scenario are: How irregular is the spatiotemporal dynamics of the large-scale circulation? Does it exhibit any trace of long memory? How sensitive is the flow to variations in the intrinsic properties of the fluid? Are such changes capable of breaking the top-down symmetry of the boundary-layers? These questions are addressed in the present thesis.

1.1 Heat, buoyancy, and fluid motion

Fluid motion in the presence of temperature gradients is an important phenomenon in nature and industrial processes. Among the many examples, perhaps the dynamics of the earth's atmosphere is the most appealing one to our daily life. After all, weather effects are perceived over a wide range of scales, encompassing cloud structures that span countries, storms localized to city areas, and gusts of wind that can be felt on a human scale.

Despite the beauty and the practical challenges posed by atmospheric fluid dynamics, most progress in the understanding of convective flows has been achieved by the study of reduced systems. A particularly simple instance is furnished by a liquid heated from below. Given the long-standing relevance of this practice in basic sciences and in culinary as a whole, it is not surprising that meticulous experiments were first reported by a Frenchman: Henri Bénard (1874–1939).

In 1900, Bénard [1] considered a metallic dish filled with a thin layer of *liquid*, whose upper surface was left in *free* contact with the ambient air. By maintaining the dish sufficiently warm at constant temperature T_b, he was able to observe beautiful hexagonal patterns on the upper surface of the liquid.

Inspired by Bénard's experiments, Lord Rayleigh (John William Strutt, 1842–1919) considered in 1916 a rather artificial convection scenario: a *horizontally infinite* layer of fluid bounded by *free-slip* surfaces. From the theoretical viewpoint such configuration seems a reasonable attempt to capture the essence of the phenomenon, but strictly speaking one might wonder about the motivation behind the choice of free-slip surfaces. To quote Lord Rayleigh [2]:

> "(...) we have to consider boundary conditions. Those have been chosen which are the simplest from the mathematical point of view, and they deviate from those obtaining in Bénard's experiments, where, indeed, the conditions are different at the two boundaries."

In this spirit, Rayleigh imposed a constant temperature T_b at the bottom plane. However, in contrast with Bénard's experiments, he assumed that the top surface was maintained at *constant* temperature $T_t < T_b$. Then, on the basis of a linear stability analysis of the hydrodynamic equations, Rayleigh achieved two major results: (i) he identified the combination of parameters that describe the competition between buoyancy and drag [see Eq. (1.1) below], and (ii) he determined the *onset* of convection. At the end, a real *tour de force*.

The significant differences between the boundary conditions adopted by Rayleigh and by Bénard clearly exemplify that a theoretically tractable problem is not necessarily realistic from the experimental point of view. But should one ignore Rayleigh's analysis? Certainly not. In fact, it is convenient to combine the strengths of Rayleigh's mathematical considerations with realistic constraints of Bénard's experiments. Such strategic combination leads to the so-called *Rayleigh-Bénard* setup.

Rayleigh-Bénard convection

The Rayleigh-Bénard setup consists of a fluid-filled container heated from below and cooled from above. By definition, the sidewalls are adiabatic, and the bottom and top plates are maintained at constant temperatures T_b and T_t, respectively. *Closed* systems of this kind are extremely valueable from the standpoint of fundamental science, since one can *control* three important aspects: the geometry of the container (e.g., cylindrical or rectangular), the type of fluid (liquid or gas), and the strength $\Delta \equiv T_b - T_t$ of the thermal driving (gentle or vigorous).

The geometry of the container is usually represented by the aspect ratio:

$$\Gamma \equiv \frac{D}{L},$$

where D and L are characteristic lengths along the horizontal and vertical directions, respectively. In the original experiments by Bénard, for instance, the metallic dish had aspect ratio $\Gamma \approx 100$. In the present thesis, however, we shall be concerned with situations in which $D \approx L$, i.e., $\Gamma \approx 1$.

Chosen the aspect ratio, the next step consists in specifying the base state of the working fluid. Although some arbitrariness may be involved here, it is convenient to define the base state in terms of the mean temperature T_m between the bottom and top plates $T_m \equiv (T_b + T_t)/2$. In this way, given T_m and the mean pressure P_m, the mean density $\rho_m = \rho(T_m, P_m)$ immediately follows from the equation of state of the fluid. In the same spirit, reference values for transport coefficients such as kinematic viscosity ν and thermal diffusivity κ are defined as $\nu_m = \nu(T_m, P_m)$ and $\kappa_m = \kappa(T_m, P_m)$. With these considerations, the fluid may be represented by a single characteristic parameter measuring its relative propensity to diffuse vorticity and heat. Such parameter is the Prandtl number:

$$Pr \equiv \frac{\nu_m}{\kappa_m}.$$

Now, as regards the strength of the thermal forcing, a measure of the competition between buoyancy and viscous drag is provided by the Rayleigh number:

$$Ra \equiv \frac{\beta_m g L^3 \Delta}{\nu_m \kappa_m}, \tag{1.1}$$

where $\beta_m = \beta(T_m, P_m)$ is the thermal expansivity of the fluid and g the gravitational acceleration. Qualitatively, the fluid is set in motion when buoyancy overcomes viscous drag, i.e., when the Rayleigh number is larger

than a certain critical value Ra_c. Quantitatively, Ra_c has a strong dependence on the boundary conditions. For instance, if a horizontally infinite layer of fluid is bounded by free-slip surfaces, then $Ra_c = 27\pi^4/4$ as showed by Lord Rayleigh [2]. On the other hand, if the surfaces are solid (i.e., no-slip), then $Ra_c \approx 1708$ [3]. In any scenario, for $Ra < Ra_c$ the fluid remains at rest. In such static regime, the vertical heat flux is entirely due to *conduction* $Q_0 \equiv \Lambda_m \Delta / L$.

In the convective regime ($Ra > Ra_c$), two coupled responses are of particular interest: (i) the speed of the circulation dynamics, and (ii) the strength of the heat transport. The speed U of the flow is traditionally expressed in terms of the Reynolds number:

$$Re \equiv \frac{L\,U}{\nu}.$$

Likewise, the heat transport is characterized by comparing the convective flux Q with the conductive flux Q_0. The ratio between them is the so-called Nusselt number:

$$Nu \equiv \frac{Q}{Q_0}.$$

Since both U and Q depend on the the properties of the fluid, on the strength of the thermal driving, and on the geometry of container, a major question in thermal convection is: How do Re and Nu depend on Ra, Pr, and Γ? In recent years there has been considerable progress in the understanding of this issue, both from the experimental and theoretical sides. Notwithstanding the extensive literature in the field, the present thesis is devoted to the regime of high Rayleigh numbers. In particular, we shall focus on typical flow structures in the range $10^8 \leqslant Ra \leqslant 10^{12}$.

1.2 Boundary layers, plumes, and the wind

Three typical structures in Rayleigh-Bénard convection are: boundary-layers (BLs), plumes, and the wind.

Thermal boundary-layers, for instance, are very thin regions in which the vertical temperature profile undergoes sharp variations. As shown in figure 1.1, they are adjacent to the heating and cooling plates, where the presence of hot and cold volumes of fluid induces the formation of unstable buoyant structures. These buoyant structures are usually referred to as plumes.

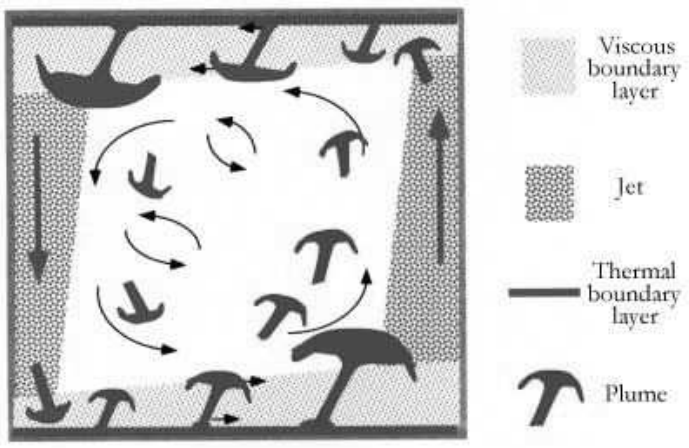

Figure 1.1: Boundary layers, plumes, and the wind according to Kadanoff [4]: *"A major point of the cartoon is to list and show the many different structures that work together to make the intricate motion of the convective system."*

Figure 1.1 suggests that the dynamics of plumes induces a large-scale circulation (also known as *the wind*). But the wind also acts back on the plume formation process. In fact, the *three*-dimensional dynamics of the large-scale circulation is very peculiar: it oscillates azimuthally and every once in a while its orientation is reversed. But how irregular in time are such reversals? Do azimuthal oscillations show any trace of long memory? We shall answer these questions in chapters 2 and 3, respectively.

Another issue involving boundary layers, plumes, and the wind concerns their dependence on the Rayleigh number. Of special importance is the manner by which high Rayleigh numbers are achieved. Though the temperature difference Δ can be increased in a controlled way, the working fluid can experience significant changes in its intrinsic properties: the larger the Δ, the more pronounced the contrast between the fluid properties at the bottom and at the top plates. Peculiarities deriving from such temperature dependence of the transport coefficients are usually referred to as non-Oberbeck-Boussinesq (NOB) effects. But how sensitive is the flow to NOB effects? Are they capable of breaking the top-down symmetry of the boundary-layers? We shall discuss these issues in chapters 4 and 5.

1.3 A guide through the chapters

To answer the questions raised hitherto, the present thesis is organized in two parts. The first one is devoted to the spatiotemporal dynamics of the wind (chapters 2 and 3), the second to non-Oberbeck-Boussinesq effects (chapters 4 and 5). Since each chapter was conceived as an individual article [5–8], the exposition is presumably self-contained. However, the experienced reader might consider a different sequence of topics that best suits his/her own interests. To this end, a brief overview is sketched below.

In chapter 2, we propose a model for the irregular cessation and subsequent reversal of the wind [5]. Our approach is deterministic. On the basis of a force balance between buoyancy and viscous drag, we derive a dynamical system for the motion of a single plume. Chaotic wind reversals generated by the model are then characterized in terms of the velocity fluctuations and the mean frequency of reversals.

Chapter 3 is concerned with the azimuthal dynamics of the wind [6]. Starting from the inviscid hydrodynamic equations, we introduce phenomenological terms representing viscous dissipation and thermal forcing (boundary-layer and plume contributions are not included). Then, by numerically solving the extended equations of motion, we show that: (i) the wind azimuthally oscillates with a time scale comparable to the large eddy turnover time, and (ii) the azimuthal angle has a long memory that lasts for hundreds of eddy turnover times.

Chapters 4 and 5 are devoted to flows in which the strength of thermal driving induces changes in the properties of the fluid [7, 8]. On the basis of boundary-layer equations with *variable transport coefficients*, we show that the top-down symmetries of the velocity, temperature, and density profiles are broken. Two different fluids are considered: water (chapter 4) and gaseous ethane under high pressure (chapter 5). The latter exhibits a more pronounced and opposite symmetry breaking as compared to the former. In both cases, our theoretical results are in reasonable agreement with experimental measurements.

Finally, chapter 6 addresses our general conclusions, including shortcomings of our methods and questions that remain open.

References

[1] H. BÉNARD, Les tourbillons cellulaires dans une nappe liquide, *Rev. Gen. Sci. Pures Appl.* **12**, 1261 (1900).

[2] LORD RAYLEIGH, On convection currents in a horizontal layer of fluid, when the higher temperature in on the under side, *Philos. Mag.* **32**, 529 (1916).

[3] S. CHANDRASEKHAR, *Hydrodynamic and Hydromagnetic Stability*, Dover, New York, 1981.

[4] L. P. KADANOFF, Turbulent heat flow: Structures and scaling, *Phys. Today* **54**, 34 (2001).

[5] F. FONTENELE ARAUJO, S. GROSSMANN, and D. LOHSE, Wind reversals in turbulent Rayleigh-Bénard convection, *Phys. Rev. Lett.* **95**, 084502 (2005).

[6] C. RESAGK, R. DU PUITS, A. THESS, F. V. DOLZHANSKY, S. GROSSMANN, F. FONTENELE ARAUJO, and D. LOHSE, Oscillations of the large scale wind in turbulent thermal convection, *Phys. Fluid* **18**, 095105 (2006).

[7] G. AHLERS, E. BROWN, F. FONTENELE ARAUJO, D. FUNFSCHILLING, S. GROSSMANN, and D. LOHSE, Non-Oberbeck-Boussinesq effects in strongly turbulent Rayleigh-Bénard convection, *J. Fluid Mech.* **569**, 409 (2006).

[8] G. AHLERS, F. FONTENELE ARAUJO, D. FUNFSCHILLING, S. GROSSMANN, and D. LOHSE, Non-Oberbeck-Boussinesq Effects in Gaseous Rayleigh-Bénard Convection, *Phys. Rev. Lett.* **98**, 054501 (2007).

2
Wind reversals*

The phenomenon of irregular cessation and subsequent reversal of the large-scale circulation in turbulent Rayleigh-Bénard convection is theoretically analyzed. The force and thermal balance on a single plume detached from the thermal boundary layer yields a set of coupled nonlinear equations, whose dynamics is related to the Lorenz equations. For Prandtl and Rayleigh numbers in the range $10^{-2} \leqslant \mathrm{Pr} \leqslant 10^{3}$ and $10^{7} \leqslant \mathrm{Ra} \leqslant 10^{12}$, the model has the following features:

1. Chaotic reversals may be exhibited at $\mathrm{Ra} \geqslant 10^{7}$.
2. The Reynolds number based on the root mean square velocity scales as $\mathrm{Re}_{\mathrm{rms}} \sim \mathrm{Ra}^{[0.41 \cdots 0.47]}$ (depending on Pr), and as $\mathrm{Re}_{\mathrm{rms}} \sim \mathrm{Pr}^{-[0.66 \cdots 0.76]}$ (depending on Ra).
3. The mean reversal frequency follows an effective scaling law $\omega/(\nu_{\mathrm{m}}\,\mathrm{L}^{-2}) \sim \mathrm{Pr}^{-(0.64\pm0.01)}\,\mathrm{Ra}^{0.44\pm0.01}$.

The phase diagram of the model is sketched, and the observed transitions are discussed.

2.1 Introduction

One important issue in turbulent Rayleigh-Bénard convection is the interplay between the large-scale circulation (the so-called wind) [1] and the dynamics of plumes detached from the thermal boundary layers [2]. In particular, such interplay seems to be relevant in the process of circulation reversals, which occur in an irregular time sequence [3–8]. Re-

*Published as: F. Fontenele Araujo, S. Grossmann, D. Lohse. Wind reversals in turbulent Rayleigh-Bénard convection, *Phys. Rev. Lett.* **95**, 084502 (2005)

markably, similar reversals are also observed in the wind direction of the atmosphere [9] and in the magnetic polarity of the earth [10].

In principle, two reversal scenarios are possible: Reversal through cessation of the convection roll, and reversal through its azimuthal rotation. With two temperature sensors placed close to each other near the sidewall [4, 5], one can detect roll reversals, but not distinguish between the two scenarios. With several sensors placed along the azimuth of the cell, Cioni *et al.* [6] succeeded to detect reversal through azimuthal rotation of the roll. Reversal through rotation was also detected in refs. [7, 8]. However, with an ingenious multi-probe setup, Brown, Nikolaenko, and Ahlers [8] were able to distinguish between the rotation and cessation scenarios,and many reversals through cessation were detected. Reversal through cessation was also observed in *two-dimensional* numerical simulations of the Boussinesq equations (see fig. 8 of ref. [11] and fig. 12 of ref. [12]), where the rotation scenario is of course impossible.

Since reversal through cessation is a more surprising scenario, the aim of the present work is to reveal its physical mechanism. Qualitatively, the picture is as follows [13]: If an uprising hot plume gets too fast because of a temperature surplus, it fails to cool down sufficiently when passing the top plate. It then is still warmer than the ambient fluid when advected down along the sidewall. By buoyancy it therefore looses speed and counteracts the large-scale circulation. Indeed, the downward wind may be counteracted so strongly that it stops or even reverses its direction. This mechanism can be effective only for sufficiently strong wind, i.e., for sufficiently large Reynolds number, because for slow motion the thermal diffusivity κ_m has enough time to reduce the temperature surplus of the originally warmer plume relative to its neighbourhood. Then its power to reverse the circulation by buoyancy is gone.

2.2 The model

In order to quantify the cessation mechanism discussed above, let us first characterize the size of a circulating plume. As shown in figure 2.1, a single plume will be understood as a thermal structure of width λ (the thickness of the thermal boudary-layer from which it originated) and length L (the height of the convection container). In addition, its volume is assumed to scale as $\lambda^2 L$, with a typical cross-section area λ^2, and surface area λL.

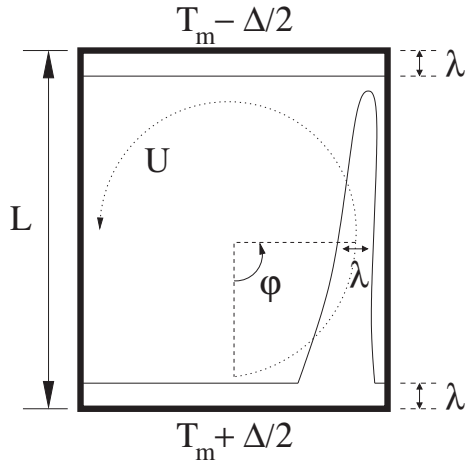

Figure 2.1: Sketch of the motion of a single plume of width λ and height L. In an aspect-ratio-one container, the circulation radius is given by $L/2$.

Supposing that such a plume circulates with velocity $U(t)$, it is reasonable to expect that its dynamics is essentially a matter of balance between buoyancy and drag.

In the Boussinesq approximation the buoyancy force (per mass) is given by $\mathbf{f}_b = -\beta_m (T - T_m)\,\mathbf{g}$, where β_m is the isobaric thermal expansion coefficient, T the plume temperature, T_m the mean temperature, and g the gravitational acceleration. On the other hand, the drag force (per mass) on the plume has the strength $f_d = \frac{1}{2} C(Re)\, U^2\, L^{-1}$, where $C(Re)$ is the drag coefficient, and the Reynolds number is defined by $Re = L\,U\,\nu_m^{-1}$. Here, $C(Re)$ is taken as [14]:

$$C(Re) = \sqrt{\left(\frac{6}{b}\right)^3}\left[\sqrt{\frac{3b^3}{8}}\,\frac{1}{Re} + \sqrt{1 + \frac{3b^3}{8\,Re^2}}\,\right], \tag{2.1}$$

where $b = 8.4$ is the Kolmogorov constant. Equation (2.1) describes the transition from the strongly decreasing drag $\sim 1/Re$ in the viscous regime to the Re-independent drag in the turbulent regime. As pointed out in ref. [14], it pretty well agrees with experimental data.

Now, let us consider the thermal interaction between a single plume and its surrounding. Strictly speaking, the surrounding consists of the fluid as well as the sidewalls, and the top and bottom plates. We do not distinguish between all these and describe the temperature of the plume

surrounding $T_s(\varphi)$ by a time-independent profile:

$$T_s(\varphi) \;=\; T_m + \frac{\Delta}{2}\cos\varphi, \tag{2.2}$$

where Δ is the temperature difference between the horizontal plates. We Fourier expand the temperature variable of the plume:

$$T(\varphi,t) \;=\; T_m + \sum_{n=1}^{\infty}\left[A_n(t)\,\sin(n\varphi) + B_n(t)\cos(n\varphi)\right], \tag{2.3}$$

where $A_n(t)$ and $B_n(t)$ are the amplitudes.

2.3 Equations of motion

In order to derive the equations of motion for a single plume, we follow an analogy with the Malkus waterwheel [15, 16]. On the basis of this analogy, our intent is to acquire an understanding of the wind dynamics through nonlinear model equations.

To begin, let us consider the balance of forces (per mass) on the plume:

$$\frac{dU}{dt} \;=\; f_b(\varphi,t)\,\sin\varphi - f_d. \tag{2.4}$$

Substituting the previous relations into (2.4), and integrating the resultant expression with respect to φ from 0 to 2π, one readily finds:

$$\frac{dU}{dt} \;=\; \frac{1}{2}\,\beta_m\,g\,A_1 - \frac{1}{2}C(Re)\,\frac{U^2}{L}. \tag{2.5}$$

Remarkably, the temporal behavior of U is coupled to the amplitude of the first temperature mode A_1 only.

The temporal change of the plume temperature is given by advection and by diffusion. For the latter, we assume a relaxation ansatz for the temperature deviation $T - T_s$ from the surrounding, with the diffusive time scale $\tau_\kappa = \lambda L/\kappa_m$, i.e.,

$$\frac{\partial T}{\partial t} + \frac{U}{L/2}\,\frac{\partial T}{\partial \varphi} \;=\; -\,\frac{T - T_s}{\tau_\kappa}. \tag{2.6}$$

The physics behind the definition of τ_κ is that the thermal loss is proportional to the plume surface, and inversely proportional to the thermal diffusivity.

Substituting (2.2) and (2.3) into (2.6), and equating the coefficients of each harmonic separately, one obtains:

$$\frac{dA_1}{dt} = -\frac{\kappa_m}{\lambda L} A_1 + \frac{2}{L} U B_1, \tag{2.7}$$

$$\frac{dB_1}{dt} = -\frac{\kappa_m}{\lambda L} B_1 + \frac{\kappa_m \Delta}{2\lambda L} - \frac{2}{L} U A_1. \tag{2.8}$$

We write the three coupled ODEs (2.5), (2.7), and (2.8) in nondimensional form. The dimensionless variables are $X = 2^{-1} Nu^{-2} \kappa_m^{-1} L U$, $Y = 2 r \Delta^{-1} A_1$, $Z = (Ra_c^{-1} - 2B_1 \Delta^{-1}) r$, $\tau = 2 Nu \kappa_m L^{-2} t$, and the dimensionless control parameters read:

$$\sigma = \frac{9}{4} \frac{Pr}{Nu}, \qquad \text{and} \qquad r = \frac{1}{18 Nu} \frac{Ra}{Ra_c}, \tag{2.9}$$

where $Pr = \nu_m/\kappa_m$ is the Prandtl number, $Ra = \beta_m g L^3 \Delta/(\nu_m \kappa_m)$ the Rayleigh number, and $Ra_c = 1708$. The Nusselt number Nu comes from the relation $\lambda/L = 1/(2\,Nu)$. Then, the system of equations (2.5), (2.7) and (2.8) becomes:

$$\frac{dX}{d\tau} = \sigma Y - \sigma X \left[1 + \sqrt{1 + \frac{27}{2 b^3 \sigma^2} X^2} \right], \tag{2.10}$$

$$\frac{dY}{d\tau} = r X - Y - X Z, \tag{2.11}$$

$$\frac{dZ}{d\tau} = -Z + X Y. \tag{2.12}$$

This system resembles the Lorenz equations [17, 18], which have also been used to describe *laminar* flow confined in a toroidal loop [19, 20]. Here equations (2.10)-(2.12) have been derived to model plume reversals in the *turbulent* regime. They will be referred to as the *modified* Lorenz equations. There are two essential differences as compared to the standard Lorenz system*: (i) The parameters σ and r are related to the Nusselt number, which is known to follow a nonuniversal (Pr-dependent) scaling with Re [21–24]. This is a key difference, since in the Lorenz equations $\sigma = Pr$ and $r = Ra/Ra_c$. (ii) The ordinary differential equation for X has a *new* nonlinear term, due to the turbulent drag on the plume.

*What however our modified Lorenz system has in common with the original one is that it is not suited to make statements on the heat flux in the turbulent regime.

2.4 Phase diagram

To investigate the dynamical properties of the system (2.10)-(2.12), we have scanned the parameter space $\mathrm{Ra} \times \mathrm{Pr}$ in the range $10^7 \leqslant \mathrm{Ra} \leqslant 10^{12}$, $10^{-2} \leqslant \mathrm{Pr} \leqslant 10^3$. Technically, our numerical scheme was based on a fourth-order Runge-Kutta method [25], with adaptive stepsize control in time, and increments of 0.1 for $\log_{10}(\mathrm{Pr})$ and $\log_{10}(\mathrm{Ra})$. The Nu-input required for coefficients (2.9) was provided by Grossmann-Lohse theory [21–24], and as initial condition we adopted $(X = 1, Y = 1, Z = 1)$. As for check with other initial values see below.

An insight into the structure of the phase diagram can be acquired by considering some representative times series of $X(\tau)$. In particular, for fixed Pr and increasing Ra, three examples are shown in figure 2.2: first, a state of uniform circulation [cf. plate (a)]; then emergence of chaotic reversals [plate (b)]; and, ultimately, periodic reversals [plate (c)].

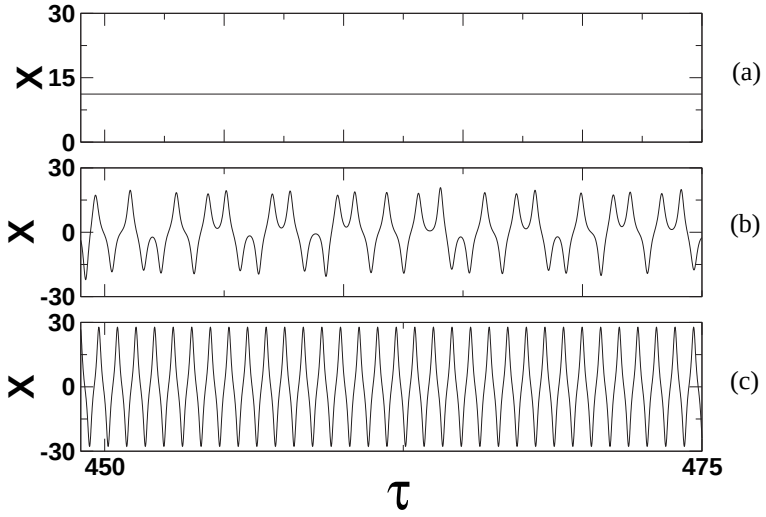

Figure 2.2: Time series of the dimensionless plume velocity X, for $\mathrm{Pr} = 0.1$ at (a) $\mathrm{Ra} = 10^{10.8}$ (uniform circulation), (b) $\mathrm{Ra} = 10^{10.9}$ (chaotic reversals), and (c) $\mathrm{Ra} = 10^{11.0}$ (periodic reversals).

Figure 2.3 shows the phase diagram in $\mathrm{Ra}\times\mathrm{Pr}$ space, displaying a sharp onset between the steady and the reversal domain. The onset of reversals can be understood in terms of the typical time scales of the system: the thermal diffusion time τ_κ and the turnover time $\tau_U = \pi L/\langle U \rangle$, where $\langle\cdot\rangle$ denotes the time average. Qualitatively, it is reasonable to expect wind re-

versals when $\tau_U \ll \tau_\kappa$, because in such case the circulation is so fast that the plume has no time to lose its temperature contrast. Indeed, we find that the ratio $\tau_U/\tau_\kappa = 2\pi \mathrm{Nu}\,\mathrm{Pr}^{-1}\langle \mathrm{Re}\rangle^{-1}$ is a monotonically decreasing function of Ra for constant Pr, roughly proportional to $\mathrm{Ra}^{-1/6}$. The overall form of the onset curve well resembles its counterpart in the phase diagram of the Lorenz model cf. Dullin *et al.* [26]. We emphasize that the onset curve remains unchanged for a variety of initial conditions.

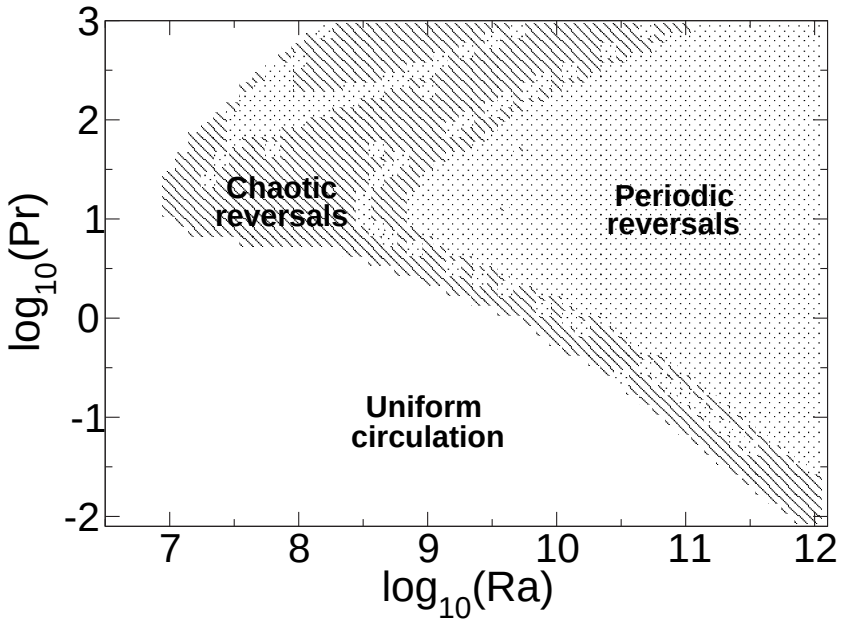

Figure 2.3: Phase diagram in the Ra $\times$ Pr plane: at sufficiently large Ra, the state of uniform circulation (blank region) gives place to chaotic (stripped region) or periodic (dotted region) wind reversals. Note the small periodic islands in the chaotic range.

2.5 Reynolds number

We now come to the dependence of the variance of the Reynolds number $\mathrm{Re}_{\mathrm{rms}} = \mathrm{L}\,u_{\mathrm{rms}}\,\nu_m^{-1}$ based on the root mean square velocity $u_{\mathrm{rms}} = \sqrt{\langle (U - \langle U\rangle)^2\rangle}$. Figure 2.4 shows $\mathrm{Re}_{\mathrm{rms}}(\mathrm{Ra},\mathrm{Pr})$: In plate (a), the Ra-scaling exponent increases from 0.41 to 0.47 for increasing Pr from 0.7 to 316; in plate (b), the Pr-scaling exponent decreases from -0.66 to -0.76 for falling Ra from 10^{12} to 10^9. Experimentally, a similar Pr-dependence has been reported [27] for the Reynolds numbers based on the maximum wind ve-

locity, on the oscillation frequency of the large-scale circulation, and on the rms velocity.

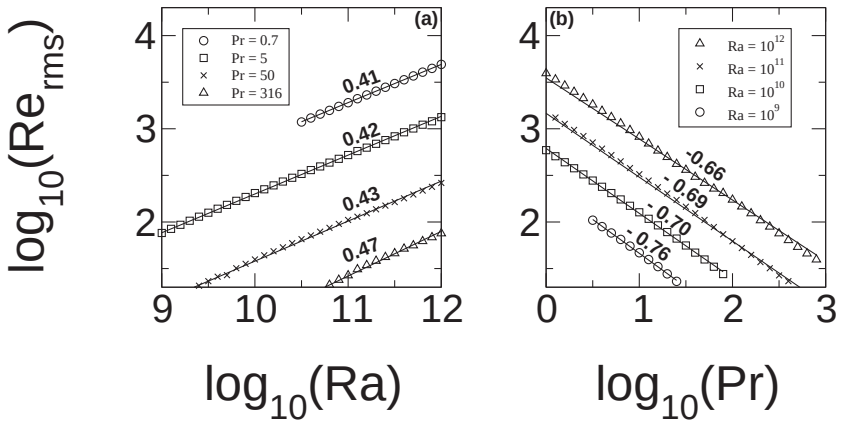

Figure 2.4: Reynolds number variance $\mathrm{Re}_{\mathrm{rms}}$ based on the root mean square velocity as function of (a) Ra and (b) Pr.

2.6 Mean reversal frequency

The abrupt change of $X(\tau)$ with τ [cf. figure 2.2(b)] suggests that the wind switching can be considered as an almost instantaneous event represented by the moment at which it occurs. Here, we follow Sreenivasan *et al.* [4] and define t'_n as the interval between an arbitrary origin in time and the *n*th wind reversal. Similarly as in [4], we also find a linear relation $t'_n \sim n$, which suggests a mean interval $\bar{t}'$ between reversals. In this way, we define $\omega = 1/\bar{t}'$ as the mean reversal frequency, and its dimensionless counterpart as $\tilde{\omega} = \omega\, L^2/\nu_m$.

According to figure 2.5, $\tilde{\omega} \sim \mathrm{Pr}^{-(0.65\pm0.01)}\, \mathrm{Ra}^{0.44\pm0.01}$. However, recent experiments with water [28] have revealed that the occurrence of cessations is reasonably independent of Ra, for $10^9 \leqslant \mathrm{Ra} \leqslant 10^{11}$. The disagreement between our theory and experimental measurements [28] suggests that a model based on only 3-modes is quantitatively inadequate. From the qualitative viewpoint, our simple *deterministic* system well mimics the dynamics of reversals, and is a complementary approach to the stochastic model of noise-induced switchings between two metastable states [4]. Here, the Lorenz attractor itself captures the bistable transitions, but a more quantitative description of the reversal phenomenon (also including the rotation scenario) would involve a subtle combination of deter-

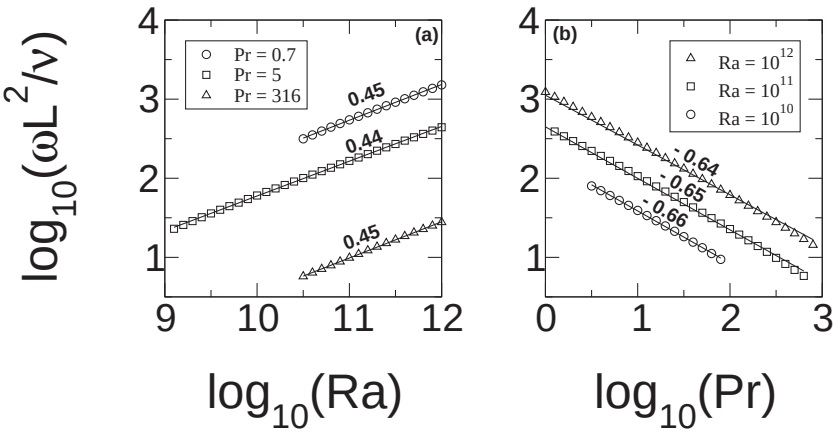

Figure 2.5: Mean reversal frequency as function of (a) Ra at fixed Pr and (b) Pr for given Ra.

ministic chaos and noise. A successful model in this direction has been recently proposed by Brown & Ahlers [29].

Acknowledgments

We thank G. Ahlers, K. R. Sreenivasan, and J. Niemela for fruitful exchange. This work is part of the research programme of Stichting FOM, which is financially supported by NWO.

References

[1] R. KRISHNAMURTI and L. N. HOWARD, Large scale flow generation in turbulent convection, *Proc. Natl. Acad. Sci.* **78**, 1981 (1981).

[2] H. D. XI, S. LAM, and K.-Q. XIA, From laminar plumes to organized flows: the onset of large-scale circulation in turbulent thermal convection, *J. Fluid Mech.* **503**, 47 (2004).

[3] R. BENZI, Flow Reversal in a Simple Dynamical Model of Turbulence, *Phys. Rev. Lett.* **95**, 024502 (2005).

[4] K. R. SREENIVASAN, A. BERSHADSKI, and J. NIEMELA, Mean wind and its reversals in thermal convection, *Phys. Rev. E* **65**, 056306 (2002).

[5] J. NIEMELA, L. SKRBEK, K. R. SREENIVASAN, and R. J. DONNELLY, The wind in confined thermal turbulence, *J. Fluid Mech.* **449**, 169 (2001).

[6] S. CIONI, S. CILIBERTO, and J. SOMMERIA, Strongly turbulent Rayleigh-Bénard convection in mercury: comparison with results at moderate Prandtl number, *J. Fluid Mech.* **335**, 111 (1997).

[7] Y. TSUJI, T. MIZUNO, T. MASHIKO, and M. SANO, Mean Wind in Convective Turbulence of Mercury, *Phys. Rev. Lett.* **94**, 034501 (2005).

[8] E. BROWN, A. NIKOLAENKO, and G. AHLERS, Reorientation of the Large-Scale Circulation in Turbulent Rayleigh-Bénard Convection, *Phys. Rev. Lett.* **95**, 084503 (2005).

[9] E. VAN DOORN, B. DHRUVA, K. R. SREENIVASAN, and V. CASSELLA, Statistics of wind direction and its increments, *Phys. Fluids* **12**, 1529 (2000).

[10] G. A. GLATZMEIER, R. C. COE, L. HONGRE, and P. H. ROBERTS, The role of Earth's mantle in controlling the frequency of geomagnetic reversals, *Nature* **401**, 885 (1999).

[11] U. HANSEN, D. A. YUEN, and S. E. KROENING, Mass and heat-transfer in strongly time-dependent thermal convetion at infinite Prandtl number, *Geophys. Astrophys. Fluid Dyn.* **63**, 67 (1992).

[12] A. FURUKAWA and A. ONUKI, Convective heat transport in compressible fluids, *Phys. Rev. E* **66**, 016302 (2002).

[13] S. GROSSMANN and D. LOHSE, Rayleigh-Prandtl number dependent phase diagram for strong thermal convection, *in High Rayleigh Number Convection, International Workshop, September 3-5, Ilmenau, Germany* (2001).

[14] D. LOHSE, Crossover from high to low Reynolds number turbulence, *Phys. Rev. Lett.* **73**, 3223 (1994).

[15] S. H. STROGATZ, *Nonlinear dynamics and chaos*, Perseus Press, Reading, 1994.

[16] M. KOLÁR and G. GUMBS, Theory for the experimental observation of chaos in a rotating waterwheel, *Phys. Rev. A* **45**, 626 (1992).

[17] E. N. LORENZ, Deterministic nonperiodic flow, *J. Atmos. Sci* **20**, 130 (1963).

[18] J. B. MCLAUGHLIN and P. C. MARTIN, Transition to turbulence in a statically stressed fluid system, *Phys. Rev. A* **12**, 186 (1975).

[19] M. GORMAN, P. J. WIDMANN, and K. A. ROBBINS, Chaotic Flow Regimes in a Convection Loop, *Phys. Rev. Lett.* **52**, 2241 (1984).

[20] P. EHRHARD and U. MÜLLER, Dynamical behavior of natural convection in a single-phase loop, *J. Fluid Mech.* **217**, 487 (1990).

[21] S. GROSSMANN and D. LOHSE, Scaling in thermal convection: A unifying view, *J. Fluid. Mech.* **407**, 27 (2000).

[22] S. GROSSMANN and D. LOHSE, Thermal convection for large Prandtl number, *Phys. Rev. Lett.* **86**, 3316 (2001).

[23] S. GROSSMANN and D. LOHSE, Prandtl and Rayleigh number dependence of the Reynolds number in turbulent thermal convection, *Phys. Rev. E* **66**, 016305 (2002).

[24] S. GROSSMANN and D. LOHSE, Fluctuations in turbulent Rayleigh-Bénard convection: The role of plumes, *Phys. Fluids* **16**, 4462 (2004).

[25] W. PRESS, S. TEUKOLSKY, W. VETTERLING, and B. FLANNERY, *Numerical Recipes*, Cambridge University Press, Cambridge, 1986.

[26] H. R. DULLIN, S. SCHMIDT, P. H. RICHTER, and S. GROSSMANN, Extended phase diagram of the Lorenz model, *ArXiv: nlin/0504024* (2005).

[27] S. LAM, X. D. SHANG, S. Q. ZHOU, and K.-Q. XIA, Prandtl-number dependence of the viscous boundary layer and the Reynolds-number in Rayleigh-Bénard convection, *Phys. Rev. E* **65**, 066306 (2002).

[28] E. BROWN and G. AHLERS, Rotations and cessations of the large-scale circulation in turbulent Rayleigh-Bénard Convection, *J. Fluid Mech.* **568**, 351 (2006).

[29] E. BROWN and G. AHLERS, Large-Scale Circulation Model for Turbulent Rayleigh-Bénard Convection, *Phys. Rev. Lett.* **98**, 134501 (2007).

3
Wind oscillations*

The large scale "wind of turbulence" of thermally driven flow is analyzed for very large Rayleigh numbers between $4 \cdot 10^{11}$ and $7 \cdot 10^{11}$ and Prandtl number of 0.71 (air at 40°C) and aspect ratios order of one. The wind direction near the upper plate is found to horizontally oscillate with a typical time scale very similar to the large eddy turnover time. The temporal autocorrelation of the wind direction reveals an extremely long memory of the system for the direction. We then apply and extend the dynamical model of Gledzer, Dolzhansky, and Obukhov to the flow, which is based on the Boussinesq equations in the bulk and which can be solved exactly in the inviscid and unforced limit, but which completely ignores the boundary layer and plume dynamics. Nevertheless, the model correctly reproduces both the azimuthal oscillations of the wind and its very long memory. It is therefore concluded that the boundary layers and the plumes are not necessary to account for the azimuthal dynamics the wind. The oscillations rather occur as intrinsic precession of the bulk flow.

3.1 Introduction

Turbulent Rayleigh-Bénard convection is characterized by a subtle interplay between small-scale turbulence and large-scale structures occupying the whole fluid domain. In spite of considerable experimental and theo-

*Published as: C. Resagk, R. du Puits, A. Thess, F. V. Dolzhansky, S. Grossmann, F. Fontenele Araujo, D. Lohse. Oscillations of the large scale wind in turbulent thermal convection, *Phys. Fluids* **18**, 095105 (2006). F.F.A. is responsible for sections 3.4.2 – 3.5

retical effort, the spatial and temporal dynamics of these large scales are not very well understood. The present work is an attempt to contribute to the understanding by conducting experiments at very high Rayleigh numbers and proposing a six-dimensional dynamical model to explain the temporal dynamics of the large scale flow.

The large scale wind or "wind of turbulence" is believed to be a crucial feature of turbulent Rayleigh-Bénard (RB) convection of aspect ratio order of one [1–28]. This wind is fed and driven by the thermal plumes detaching from the boundary layers but also acts back on the plume formation process [6, 12, 13]. In the 90's the "flywheel picture" [11] has been developed for the large scale wind. In recent years however it became clear that at least in cylindrical Rayleigh-Bénard cells (of aspect ratio order of one) the internal dynamics of the wind is more complicated: The *horizontal* direction of the wind near the thermal plate oscillates in time [20, 29]. This is remarkable as the driving buoyancy has a *vertical* component only. The temporal correlations of the wind direction oscillations are found to be very long, namely, hundreds of large eddy turnover times. The existence of a time-periodic behavior in the RB cell had been noticed before, first by the identification of a peak in the temperature power spectrum [3, 30], but the frequency of this oscillation had been associated with periodic plume emission [6, 12, 13, 19, 31]. In contrast, the results of ref. [20] suggest that the origin of the distinguished frequency is the horizontal oscillation of the large scale wind.

Beyond the horizontal oscillations, the large scale wind can also reorientate after cessation [15, 21, 29, 32, 33]. As compared to the "wiggling" of the large scale wind, this cessation scenario is rare [29]. In ref. [21] some of us have already developed a dynamical model for reorientation by cessation, which however did not yet allow for any azimuthal degree of freedom. For very large Rayleigh number (beyond 10^{11} for an aspect ratio 1/2 cell and even higher for an aspect ratio 1 cell) the large scale wind may even break down [26, 27], as the driving plumes may have cooled down before they reach the other side of the cell.

In this chapter we will provide further experimental evidence for the oscillations of the wind direction. We will study the dependence of this oscillations on the aspect ratio Γ. Tong, Xia, and coworkers [19] have reported that the oscillations are much stronger for $\Gamma = 2$ as compared to the $\Gamma = 1$ case and are even absent for $\Gamma = 1/2$. However, from recent work [25, 26, 34–36] it is known that the flow structure and the large scale wind can drastically change when changing the aspect ratio from 1 to 1/2, namely, from a one-roll scenario to a two-roll scenario. Therefore

we decided to change the aspect ratio only slightly – keeping it order of 1 – and detect the corresponding change in the oscillation frequency. The experiments are performed with the seven meter high "Barrel of Ilmenau" [37] which allows for a good spatial resolution of the flow boundary layer dynamics. The setup unfortunately implies that the Rayleigh number is changed together with the aspect ratio. The Rayleigh number in our experiments is a factor of 100 to 1000 larger than in the experiments by Funfschilling and Ahlers [20], namely $4 \cdot 10^{11}$ to $7 \cdot 10^{11}$. Also the Prandtl number is different, namely $\mathrm{Pr} = 0.71$ instead of 6 as in ref. [20]. Nevertheless, the orientation of the large scale convection roll again shows oscillations on a time scales similar to the large eddy turnover time and extremely long memory effects, just as seen in ref. [20].

In the second part of this chapter we will analyze the dynamics of the wind orientation within a dynamical model developed by Dolzhansky, Gledzer, and Obukhov [38, 39]. This model is based on the inviscid, incompressible Boussinesq equations. It has the advantage that in a triaxial ellipsoidal geometry with free-slip boundary conditions it can be solved exactly. When introducing phenomenological forcing and dissipation, it can still easily – namely by reducing the dynamics to a set of six coupled ordinary differential equations – be solved numerically over thousands of large eddy turnovers, which is crucial when studying the long time dynamics and inaccessible in any full numerical simulation of the Boussinesq equations.

Admittedly, the employed geometry and boundary conditions are different from any real flow situation in a Rayleigh-Bénard cell. In particular, all the boundary layers with the detaching plumes are not represented in this model, neither is the corner-flow in the corners of the cylindrical cell [24]. It is the more remarkable that the dynamics of the large scale wind orientation has many similarities with the experimentally measured dynamics. We find comparable oscillations of the wind orientation with an extremely long memory.

Our findings lead us to the conclusion that the horizontal oscillations are *intrinsic to the bulk dynamics* and *not caused* by periodic ejections of plumes from the boundary layers. We therefore call them "inertial oscillations". This picture was already suggested in ref. [20] where the horizontal motion of plumes near the top and bottom plates were studied and where it was found that the orientation of plumes (and thus presumably the orientation of the mean wind) oscillates. Unlike the authors of ref. [20] we have access to the velocity field and can therefore probe the bulk flow directly. However, clearly the plume ejection and dynamics must be *coupled*

to the dynamics of the large scale convection role. And they also of course drive the convection as demonstrated in [18]. However, from the point of view of the horizontal wind oscillations our results suggest that they can be viewed as passive objects, being advected with the flow.

The triaxial ellipsoidal geometry of our flow model allows to analytically study the aspect ratio dependence. Formally, the model equations are analog to the equations that describe the precession of a heavy top. For the limiting case of convection in a sphere the equations reduce to the Lorenz-equations [40–43].

The chapter is organized as follows: In section 3.2 we present our experimental results. Section 3.3 begins with a re-derivation of Dolzhansky, Gledzer, and Obukhov's dynamical model [38, 39], first, as it hitherto has not been accessible to the western literature, and second, to highlight certain assumptions which must be made when deriving the equations. Third, we also extend the model to include the pressure. We then introduce a phenomenological forcing and a phenomenological damping to the model and connect the forcing and damping strengths to the experimental findings for the Nusselt and Reynolds number as functions of the Rayleigh and Prandtl numbers. In section 3.4 we study the general properties of the extended Dolzhansky-Gledzer-Obukhov model, including those of limiting cases. In section 3.5 we present the model results, in particular for the dynamics of the orientation of the large scale wind and compare them with the experimental findings. Section 3.6 contains the discussion and conclusions.

3.2 Experiments

3.2.1 Experimental setup and procedure

The experiments are performed in the "Barrel of Ilmenau". A sketch of the barrel is shown in figure 3.1. It is a nearly cylindrical container with a mean diameter $D = 7.15$ m. For our experiments we have chosen three different heights L for the container, corresponding to aspect ratios $\Gamma = D/L = 1.13$, $\Gamma = 1.24$, and $\Gamma = 1.36$, respectively. The cross section of the cylinder is slightly elliptical due to weak nonuniformities in shape and size of the elements of which the apparatus is made. The working fluid is air, whose Prandtl number $Pr = \nu_m/\kappa_m$ (ratio between the kinematic viscosity ν_m and the thermal diffusivity κ_m) is approximately 0.71. A temperature difference of $\Delta = 40$K is established between the electrically heated

bottom and a water cooled free hanging cooling plate. In this context, the Rayleigh number,

$$Ra = \frac{\beta_m g L^3 \Delta}{\nu_m \kappa_m},$$

where β_m denotes the thermal expansion coefficient and g the gravitational acceleration, ranges between $Ra = 4.3 \cdot 10^{11}$ and $Ra = 7.3 \cdot 10^{11}$, depending on the aspect ratio, see table 3.1. Details of the experimental apparatus are described in ref. [37].

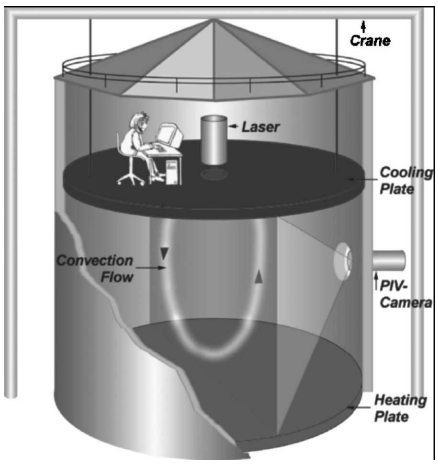

Figure 3.1: Sketch of the "barrel of Ilmenau" in which the experiments were performed. The lower plate is heated. The upper (cooling) plate can be moved up and down, thus varying the height of the cell and the aspect ratio.

We simultaneously measure the two horizontal velocity components at a fixed distance $z = 0.01L$ from the cooling plate using laser Doppler velocimetry. According to ref. [44], this is about three times the thickness of the kinetic boundary layer. The measurement is made through a small glass window in the center of the cooling plate. The time series for the horizontal velocity components $V_x(t) = V(t)\cos\phi(t)$ and $V_y(t) = V(t)\sin\phi$ are converted into the polar representation for the horizontal velocity, resulting in a time dependence of the horizontal velocity amplitude $V(t)$ and the azimuthal angle $\phi(t)$.

3.2.2 Experimental results on the large-scale wind dynamics

Typical time series for the horizontal velocity amplitude $V(t)$ and the azimuthal angle $\phi(t)$ are shown in figure 3.2. While $V(t)$ looks turbulent and does not show any signature of order and regularity, *periodic* structures are clearly visible in the behavior of $\phi(t)$, signalling a periodic oscillation of the direction of the large scale wind. It is interesting that the absence of periodicity in V is in contrast to recent findings of Xi *et al* [45] who found oscillations both in V and in ϕ. This difference is probably due to the fact that the Rayleigh number in the present work is by two orders of magnitude higher than in ref. [45].

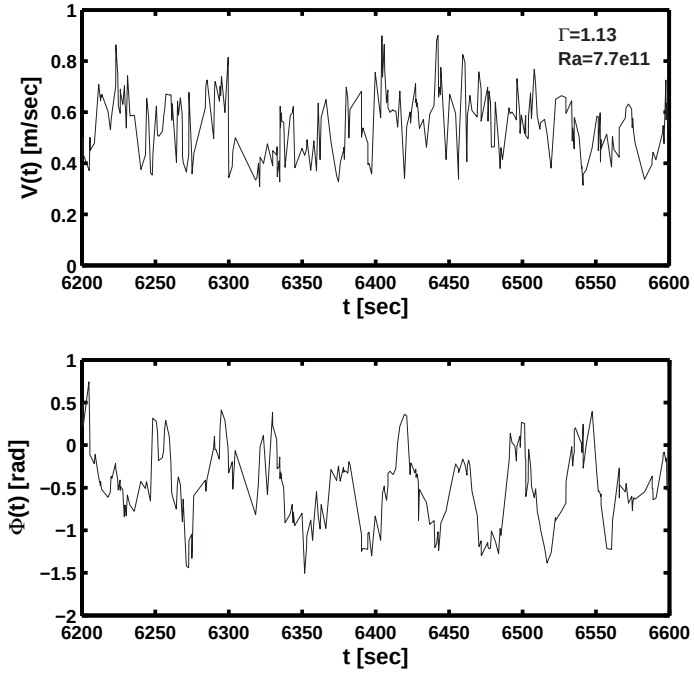

Figure 3.2: Coherent oscillations observed in turbulent Rayleigh-Bénard convection in air: Time series of the horizontal velocity amplitude $V(t)$ (upper plate) and azimuthal angle $\phi(t)$ (lower plate) for $\Gamma = 1.13$ and $Ra = 7.3 \times 10^{11}$ as obtained from two-dimensional laser Doppler velocimetry measurements near the cooling plate. The time series for the other two aspect ratios are similar in their appearance.

This visual impression is quantified by inspection of the respective au-

tocorrelation functions $C_V(\tau)$ and $C_\phi(\tau)$, both shown in figure 3.3. Indeed, the autocorrelation function of the horizontal velocity does not indicate any periodicity. The time series of the horizontal velocity can therefore be characterized by its temporal average $\overline{V}$ (given in table 3.1), superimposed by strong turbulent fluctuations. In contrast, the autocorrelation function of the azimuthal angle displays a distinct periodicity with well defined correlation time τ_c, as summarized in table 3.1. As expected, the correlation time τ_c is approximately equal to the large eddy turnover time

$$\tau_{let} = \frac{2D+2L}{\overline{V}} = \frac{2D(1+\Gamma^{-1})}{\overline{V}}. \tag{3.1}$$

Both τ_c and τ_{let} show the same trend as function of Ra and Γ.

But in addition to the large eddy turnover time, a very long correlation timescale of more than 1000 seconds (more than 15 minutes) can clearly be recognized from the autocorrelation of the azimutal angle, see figures 3.3 (b), (d), and (f). 1000 seconds corresponds to about 20 large eddy turnover times. This is a long and unexpected time correlation, reflecting long memory of the large scale wind's azimuthal direction. It resembles similar results by Funfschilling and Ahlers [20] at much smaller Rayleigh numbers between $7 \cdot 10^7$ and $3 \cdot 10^9$. The autocorrelation time of the azimutal angle seems to be longer in the experiments with aspect ratios $\Gamma = 1.24$ and $\Gamma = 1.36$ than in the experiment with the smallest aspect ratio $\Gamma = 1.13$.

The increase in the angular autocorrelation for times larger than 1000s (see insets of figures 3.3b,d, and f) presumably originates from the fact that the roll orientation is limited to a finite set of angles $[0, 2\pi]$, i.e., it is an artifact of limiting the angle to this finite set.

In the next sections we will show that the main experimental results – the horizontal oscillations of the wind's direction near the upper plate with their large memory – are reflected in a simple dynamical model based on the inviscid, incompressible Boussinesq equations.

3.3 Formulation of the model

In this section we will re-derive and extend the dynamical model of Dolzhansky, Gledzer, and Obukhov [38, 39]. The formulation of the model will consist of four steps. In subsection 3.3.1 we define the geometry and the hydrodynamical equations, namely, the inviscid Boussinesq equations. In

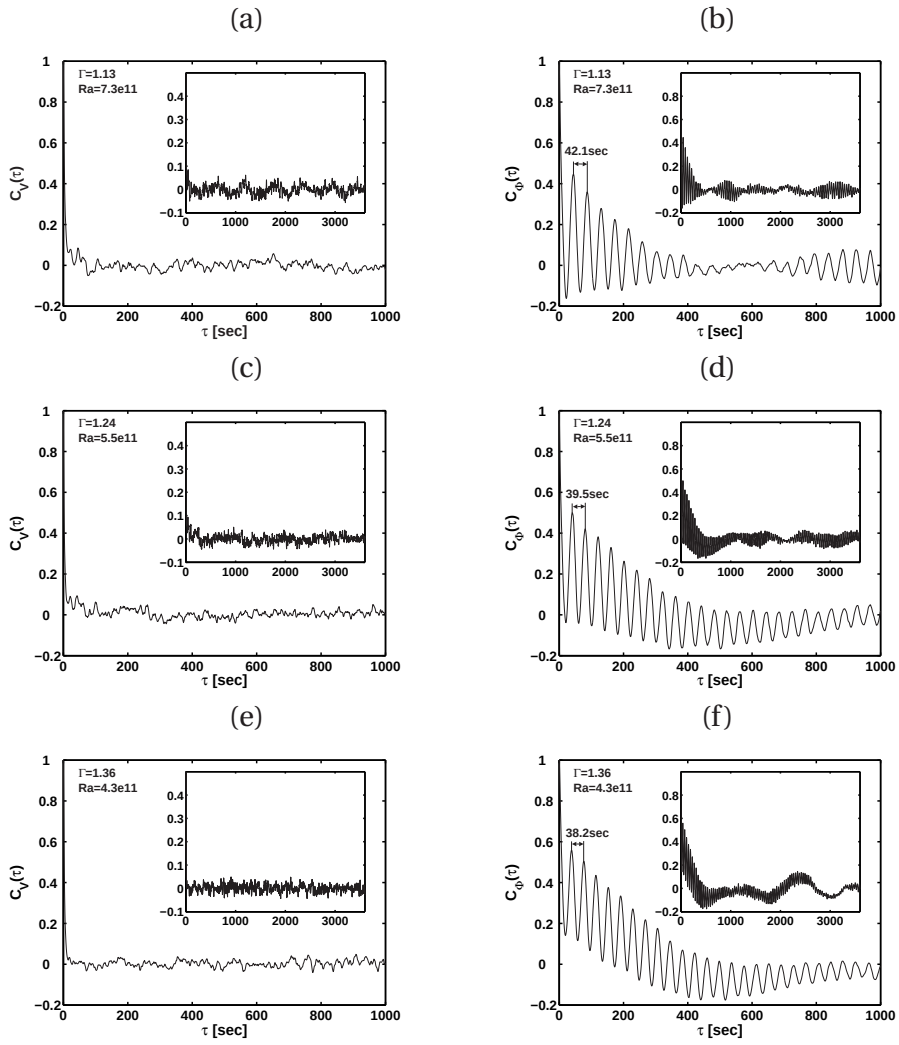

Figure 3.3: Autocorrelation functions of the velocity amplitude (a), (c), (e) and of the azimuthal angle (b), (d), (f) as obtained from experimental velocity data. In (a) and (b) the aspect ratio $\Gamma = 1.13$, and the corresponding Rayleigh number is $\mathrm{Ra} = 7.3 \times 10^{11}$. In (c) and (d) $\Gamma = 1.24$ and $\mathrm{Ra} = 5.5 \times 10^{11}$. In (e) and (f) $\Gamma = 1.36$ and $\mathrm{Ra} = 4.3 \times 10^{11}$. Note that the periodic fine-structures in the autocorrelation function of the azimuthal angle persist up to about $\tau = 1000\,\mathrm{s}$ which corresponds to more than 15 minutes and more than 20 large eddy turnover times. This demonstrates the long memory of the azimuthal direction of the large scale wind. The insets show the autocorrelation functions on longer timescale.

Γ	Ra	$\overline{V}(m/s)$	$\tau_{let}(s)$	$\tau_c(s)$	σ_ϕ [rad]
1.13	7.3×10^{11}	0.544	49.55	42.1	0.5124
1.24	5.5×10^{11}	0.585	44.16	39.5	0.4394
1.36	4.3×10^{11}	0.649	38.23	38.2	0.3844

Table 3.1: Summary of experimentally determined mean velocities $\overline{V}$, correlation times τ_c and rms-fluctuations σ_ϕ of the angle ϕ. For comparision we also give the large eddy turnover time τ_{let} as defined in equation (3.1). It approximately equals τ_c and shows the same trend as function of Ra and Γ. Notice that the mean velocity *increases* with decreasing Rayleigh number probably because of its nontrivial (and presently unknown) dependence on the aspect ratio.

subsection 3.3.2 we show that in the chosen geometry a family of solutions to these equations exist [38, 39] with a particular space dependence. The Ansatz, which is linear in space coordinates, reduces the partial differential equations to ordinary differential equations for the time dependent amplitudes. In subsection 3.3.3 we then extend the model by adding phenomenological terms representing dissipation and thermal forcing. Finally, in section 3.3.4, we connect the nondimensional parameters of our model to the Rayleigh and Prandtl numbers of real turbulent convective flows by making use of Grossmann & Lohse's phenomenological scaling theory [9, 44, 46, 47], which sufficiently well describes the experimentally measured dependences of the Nusselt and Reynolds numbers on the Rayleigh and Prandtl numbers, $Nu(Ra, Pr)$ and $Re(Ra, Pr)$.

3.3.1 Non-dissipative and non-diffusive Boussinesq dynamics in an ellipsoid

Following Dolzhansky, Gledzer, and Obukhov [38, 39], we consider inviscid and non-diffusive flow in the interior of a triaxial ellipsoid

$$\frac{x^2}{a^2} + \frac{y^2}{b^2} + \frac{z^2}{c^2} = 1, \tag{3.2}$$

which is characterized by its semi-axes a, b, and c. Assume that the fluid is heated in such a way that throughout the volume a linear temperature profile

$$T_{quiescent} = -\gamma z, \quad -c\sqrt{1 - \frac{x^2}{a^2} - \frac{y^2}{b^2}} \leqslant z \leqslant +c\sqrt{1 - \frac{x^2}{a^2} - \frac{y^2}{b^2}} \tag{3.3}$$

is imposed. T denotes the deviation of the fluid temperature from some reference value T_0.

As both the viscosity and the thermal diffusivity of the fluid are assumed to be zero, the flow dynamics is governed by the inviscid, incompressible Boussinesq equations

$$\frac{\partial \boldsymbol{V}}{\partial t} + (\boldsymbol{V}\cdot\nabla)\boldsymbol{V} = -\frac{\nabla P}{\rho} + \beta_m g T\,\mathbf{k}, \tag{3.4}$$

$$\frac{\partial T}{\partial t} + (\boldsymbol{V}\cdot\nabla)T = 0, \tag{3.5}$$

where β_m is the coefficient of thermal expansion, g the acceleration of gravity, and $\mathbf{k}$ the unit normal vector in z-direction.

3.3.2 Ansatz for the velocity and temperature fields

Dolzhansky, Gledzer, and Obukhov [38, 39] observed that under free-slip boundary conditions above equations admit a family of exact solutions of the form

$$\begin{aligned}\boldsymbol{V}(x,y,z,t) = {} & u(t)\left(\frac{c}{a}\frac{y}{b}\,\mathbf{k} - \frac{b}{a}\frac{z}{c}\,\mathbf{j}\right) + v(t)\left(\frac{a}{b}\frac{z}{c}\,\mathbf{i} - \frac{c}{b}\frac{x}{a}\,\mathbf{k}\right)\\ & + w(t)\left(\frac{b}{c}\frac{x}{a}\,\mathbf{j} - \frac{a}{c}\frac{y}{b}\,\mathbf{i}\right),\end{aligned} \tag{3.6}$$

$$T(x,y,z,t) = -\varphi(t)\frac{x}{a} - \chi(t)\frac{y}{b} - \psi(t)\frac{z}{c}, \tag{3.7}$$

provided that the set of coefficients $(u, v, w, \varphi, \chi, \psi)$ satisfies the equations

$$\dot{u} = \frac{b^2-c^2}{b^2+c^2}\,\frac{a}{bc}\,vw - \beta_m g c\,\frac{a}{b^2+c^2}\,\chi, \tag{3.8}$$

$$\dot{v} = \frac{c^2-a^2}{c^2+a^2}\,\frac{b}{ac}\,wu + \beta_m g c\,\frac{b}{c^2+a^2}\,\varphi, \tag{3.9}$$

$$\dot{w} = \frac{a^2-b^2}{a^2+b^2}\,\frac{c}{ab}\,uv, \tag{3.10}$$

$$\dot{\varphi} = v\,\frac{1}{b}\,\psi - w\,\frac{1}{c}\,\chi, \tag{3.11}$$

$$\dot{\chi} = w\,\frac{1}{c}\,\varphi - u\,\frac{1}{a}\,\psi, \tag{3.12}$$

$$\dot{\psi} = u\,\frac{1}{a}\,\chi - v\,\frac{1}{b}\,\varphi. \tag{3.13}$$

This choice restricts the considered class of flows strongly. In particular, the linear dependence of the temperature profile on the spatial coordinates is not a good approximation to the profile in real convection. Nevertheless the model is capable of reproducing our experimental results, as will be shown in the next section. Before we solve this set of six ODEs for the velocity amplitudes $u(t), v(t), w(t)$ and the temperature amplitudes $\varphi(t), \chi(t), \psi(t)$, we briefly recall how to derive them.

The velocity field consists of a superposition of three subfields

$$\mathbf{V}_1 \;=\; u(t)\left(\frac{c}{a}\frac{y}{b}\mathbf{k} - \frac{b}{a}\frac{z}{c}\mathbf{j}\right), \text{etc.} \tag{3.14}$$

These twodimensional subfields possess velocity potentials $\Phi_1(y, z, t)$, with $V_{1,y} = -\partial_z\Phi_1$ and $V_{1,z} = \partial_y\Phi_1$, etc., which guarantees incompressibility, with

$$\Phi_1(y, z, t) \;=\; \frac{1}{2}\left(\frac{c}{a}\frac{y^2}{b} - \frac{b}{a}\frac{z^2}{c}\right), \text{etc.} \tag{3.15}$$

The lines of spatially constant Φ_1 are ellipses. Thus, free-slip boundary conditions are valid, while the normal component $\mathbf{V}_1 \cdot \mathbf{n}_1 = 0$ vanishes at the surface, i.e., along the ellipses, since:

$$\mathbf{n}_1 \;=\; \frac{\nabla\Phi_1}{|\nabla\Phi_1|} \;=\; \frac{(\partial_y\Phi_1, \partial_z\Phi_1)}{\sqrt{(\partial_y\Phi_1)^2 + (\partial_z\Phi_1)^2}} \;=\; \frac{(V_{1,z}, -V_{1,y})}{|\mathbf{V}_1|}.$$

Of course, the nonlinearity $\mathbf{V}\cdot\nabla\mathbf{V}$ couples the three subfields $\mathbf{V}_{1,2,3}$.

The terms on the left-hand side of the Navier-Stokes equation (3.4) are linear in x, y, z by this ansatz. Therefore, also the thermal driving has to be linear in the space variables, enforcing the linear temperature field eq. (3.7), with three time dependent amplitudes $\varphi(t), \chi(t), \psi(t)$. The time derivatives $\dot\varphi, \dot\chi, \dot\psi$ can be calculated from (3.5) using

$$\begin{aligned}\mathbf{V}\cdot\nabla \;=\; &\left(v\frac{a}{b}\frac{z}{c} - w\frac{a}{c}\frac{y}{b}\right)\partial_x + \left(w\frac{b}{c}\frac{x}{a} - u\frac{b}{a}\frac{z}{c}\right)\partial_y \\ &+ \left(u\frac{c}{a}\frac{y}{b} - v\frac{c}{b}\frac{x}{a}\right)\partial_z\,.\end{aligned} \tag{3.16}$$

Inserting this into eq. (3.5) the coefficients of $\mathbf{i}$, $\mathbf{j}$, and $\mathbf{k}$ immediately result in the three equations (3.11), (4.4), and (3.13) for the temperature amplitudes. – Note that T in eq.(3.5) not necessarily has to be of first order in x, y, z to satisfy that equation. The linearity comes from matching the linear $\mathbf{V}$ in eq. (3.4).

Next we have to derive the three equations (3.8), (3.9), (3.10) for $\dot{u}, \dot{v}$, and $\dot{w}$. For this we start from the vorticity equation instead of eq. (3.4) by taking the curl of the Navier-Stokes equation. The vorticity field

$$\boldsymbol{\omega} = \nabla \times \mathbf{V} = \frac{u(t)}{a}\left(\frac{b}{c}+\frac{c}{b}\right)\mathbf{i} + \frac{v(t)}{b}\left(\frac{a}{c}+\frac{c}{a}\right)\mathbf{j} + \frac{w(t)}{c}\left(\frac{a}{b}+\frac{b}{a}\right)\mathbf{k} \quad (3.17)$$

is constant in space but varies with time. Clearly, up to geometrical factors the vorticity amplitudes in the three spatial directions are given by $u(t)/a$, $v(t)/b$, $w(t)/c$. Since the spatial components of the velocity field are superpositions (e.g. in direction $\mathbf{i}$ the amplitude is $v(t)\frac{a}{b}\frac{z}{c} - w(t)\frac{a}{c}\frac{y}{b}$), we have to consider the u, v, w as measures for the vorticity rather than for the velocity.

The equation of motion for the vorticity reads (remember that $\boldsymbol{\omega}$ is space independent)

$$\partial_t \boldsymbol{\omega} - \boldsymbol{\omega} \cdot \nabla \mathbf{V} \;=\; \beta_m g \nabla T \times \mathbf{k}\,. \quad (3.18)$$

The right-hand side is a vector in the $(\mathbf{i}, \mathbf{j})$-plane, $(-\beta_m g\chi/b)\mathbf{i} + (\beta_m g\varphi/a)\mathbf{j}$. Inserting eq. (3.17) into the lhs of eq. (3.18), the three components $\mathbf{i}$, $\mathbf{j}$, and $\mathbf{k}$ directly and immediately imply eqs. (3.8), (3.9), and (3.10).

The set of six ODEs (3.8) to (3.13) thus represents the vorticity and temperature equations of motion. Solving them gives all amplitudes and, via (3.6), (3.17), and (3.7), the fields $\mathbf{V}(t)$, $\boldsymbol{\omega}(t)$, and $T(t)$. Note the formal argument [48] that the vorticity equation for incompressible fluid flow is sufficient to calculate also $\mathbf{V}$: knowing the sources $\nabla \cdot \mathbf{V} = 0$ together with the vortices $\nabla \times \mathbf{V} = \boldsymbol{\omega}$ the field is determined. We calculate the sources and vortices at time $t + dt$ from the known ones at time t with the vorticity equation of motion. Finally one can use the Navier-Stokes equation (3.4) to evaluate the pressure force field

$$\nabla P \;=\; \rho\left[\beta_m g T \mathbf{k} - \partial_t \mathbf{V} - (\mathbf{V} \cdot \nabla)\mathbf{V}\right],$$

which by a line integration gives the pressure field itself.

It is straightforward to calculate

$$-\frac{1}{\rho}\partial_x P \;=\; -\frac{1}{\rho}\nabla P \cdot \mathbf{i} \;=\; \left[\partial_t \mathbf{V} + (\mathbf{V} \cdot \nabla)\,\mathbf{V} - \beta_m g T \mathbf{k}\right] \cdot \mathbf{i}$$

by inserting $\mathbf{V}$, T, and $\mathbf{V} \cdot \nabla$ from eqs. (3.6), (3.7), and (3.16). The result is ordered according to contributions proportional to x/a, y/b, z/c. For the derivatives $\dot{u}, \dot{v}, \dot{w}$ the equations of motion (3.8) - (3.10) are used. Doing

the same for $-\frac{1}{\rho}\partial_y P$ and $-\frac{1}{\rho}\partial_z P$ one finds linear forms in $\tilde{x}_i = \left(\frac{x}{a}, \frac{y}{b}, \frac{z}{c}\right)$ for each of them, without any constant term. Therefore the pressure is a quadratic form, which can be written as

$$\frac{P}{\rho} = \frac{1}{2} p_{ij} \tilde{x}_i \tilde{x}_j \,, \qquad \text{sum over } i,j = 1,2,3 \,, \qquad p_{ij} = p_{ji} \,. \tag{3.19}$$

There are no linear terms in $\tilde{x}_i$, since no constant terms appear in ∇P. Comparing then the pressure gradient obtained from (3.19) with the before calculated gradient components, one finds the following matrix kernel for the *kinematic* pressure P/ρ:

$$p_{11} = a^2 \left(\frac{v^2}{b^2} + \frac{w^2}{c^2} \right), \tag{3.20}$$

$$p_{12} = -\frac{2ab}{a^2+b^2} uv, \tag{3.21}$$

$$p_{13} = -\frac{2ac}{a^2+c^2} uw - \frac{a^2 c}{a^2+c^2} \beta_m g \varphi, \tag{3.22}$$

$$p_{22} = b^2 \left(\frac{u^2}{a^2} + \frac{w^2}{c^2} \right), \tag{3.23}$$

$$p_{23} = -\frac{2bc}{b^2+c^2} vw - \frac{b^2 c}{b^2+c^2} \beta_m g \chi, \tag{3.24}$$

$$p_{33} = c^2 \left(\frac{u^2}{a^2} + \frac{v^2}{b^2} \right) - c \beta_m g \psi. \tag{3.25}$$

The construction rules of the matrix elements are rather evident. Note that the p_{ij} have units of $m^2 s^{-2}$, i.e., the matrix elements are quadratic in the velocity amplitudes u, v, w or, since the $\beta_m \varphi, \beta_m \chi, \beta_m \psi$ are dimensionless, they are given in terms of gc, which also has dimension $m^2 s^{-2}$.

From this pressure tensor (3.20)–(3.25) together with eq.(3.19) one can evaluate the physical pressure P at any position in the ellipsoidal volume. The main axes of the ellipsoid, in particular, with $(x, 0, 0)$, $(0, y, 0)$, and $(0, 0, z)$, allow to measure $u^2, v^2,$ and w^2 as well as ψ. Measuring even the pressure correlations will allow us to compare with the 4th-order moments of the velocity amplitudes u, v, w.

The system of ODEs (3.8)-(3.13) for the amplitudes has two conserved quantities, namely the total energy

$$E = \frac{1}{2} \left(\frac{b^2+c^2}{a^2} u^2 + \frac{c^2+a^2}{b^2} v^2 + \frac{a^2+b^2}{c^2} w^2 \right) + \beta_m g c \psi, \tag{3.26}$$

consisting of kinetic and potential energy, and the volume integral of the potential vorticity $(\nabla \times \boldsymbol{V}) \cdot \nabla T$ which is well known in geophysical fluid dynamics [49] and is proportional to

$$\Pi = \frac{b^2+c^2}{a} u\varphi + \frac{c^2+a^2}{b} v\chi + \frac{a^2+b^2}{c} w\psi. \tag{3.27}$$

The units are $[E] = m^{-2}s^{-2}$ and $[\Pi] = m^2 s^{-1}K$.

The equations of motion (3.8) to (3.13) for the amplitudes can be written in compact form, if we define a diagonal matrix $\hat{J}$ with elements $J_u = b^2 + c^2$, $J_v = a^2 + c^2$, $J_w = a^2 + b^2$ and introduce the three-component objects $\boldsymbol{\Omega} = (u/a, v/b, w/c)$ and $\boldsymbol{\Theta} = (\varphi, \chi, \psi)$. $\boldsymbol{\Omega}$ comprises the vorticity amplitudes and $\boldsymbol{\Theta}$ those of the temperature field. The equations of motion then become

$$\hat{J}\dot{\boldsymbol{\Omega}} = \boldsymbol{\Omega} \times \hat{J}\boldsymbol{\Omega} + \beta_m g c \mathbf{k} \times \boldsymbol{\Theta}, \tag{3.28}$$

$$\dot{\boldsymbol{\Theta}} = \boldsymbol{\Omega} \times \boldsymbol{\Theta}. \tag{3.29}$$

As has been shown by Dolzhansky [38] the mathematical structure of this system is identical to the equations for a heavy top in classical mechanics. This analogy can be further highlighted by introducing the auxiliary vector $\mathbf{L} = \hat{J}\boldsymbol{\Omega}$ in which case the first equation becomes $\dot{\mathbf{L}} = \boldsymbol{\Omega} \times \mathbf{L} + \beta_m g c \mathbf{k} \times \boldsymbol{\Theta}$ while the second remains unchanged. The analogy to the dynamics of the heavy top becomes evident when $\boldsymbol{\Omega}$, $\mathbf{L}$, and $\boldsymbol{\Theta}$ are identified with the angular velocity, angular momentum, and unit vector pointing from the support of the top to its center of mass. The conserved quantities can then be written as

$$E = \frac{1}{2}\, \boldsymbol{\Omega} \cdot \hat{J} \cdot \boldsymbol{\Omega} + \beta_m g c \psi \tag{3.30}$$

and

$$\Pi = \boldsymbol{\Omega} \cdot \hat{J} \cdot \boldsymbol{\Theta}. \tag{3.31}$$

3.3.3 Phenomenological representation of dissipation, diffusion, and forcing

In order to incorporate viscous friction, thermal diffusion, and heating into the equations (3.28) and (3.29), we add two linear dissipative terms with coefficients ξ and μ describing the inverse of a viscous and thermal decay time, respectively. The heating is modelled by a thermal volume

forcing, described by a source term in the equation for $\boldsymbol{\Theta}$. We thus arrive at the system

$$\hat{\jmath}\dot{\boldsymbol{\Omega}} = \boldsymbol{\Omega} \times \hat{\jmath}\boldsymbol{\Omega} + \beta_m g c \mathbf{k} \times \boldsymbol{\Theta} - \xi \hat{\jmath}\boldsymbol{\Omega}, \tag{3.32}$$

$$\dot{\boldsymbol{\Theta}} = \boldsymbol{\Omega} \times \boldsymbol{\Theta} - \mu(\boldsymbol{\Theta} - \boldsymbol{\Theta}_0), \tag{3.33}$$

where $\boldsymbol{\Theta}_0 = \gamma c \mathbf{k}$ and $\gamma > 0$ being a constant temperature gradient imposed in the z direction. This corresponds to unstable stratification.

It should be emphasized that ξ and μ are phenomenological coefficients with unit s^{-1}, which represent kinematic viscosity and thermal diffusivity, but whose values are not derived from first principles. Strictly speaking, they should be obtained by comparison with either direct numerical simulation of the full three-dimensional problem or with experiments. For weakly nonlinear flow close to the threshold of instability of the time-independent and quiescent solution $\boldsymbol{\Omega} = 0$, $\boldsymbol{\Theta} = \boldsymbol{\Theta}_0$ (to be evaluated in section 4.1) $\xi \sim \nu_m/\ell^2$ and $\mu \sim \kappa_m/\ell^2$ where ν_m is the kinematic viscosity, κ_m the thermal diffusivity of the fluid and ℓ a characteristic length of the ellipsoid, e.g. $\ell = c$. For turbulent convection, however, which is the central focus of the present work, the phenomenological parameters should be interpreted in terms of a turbulent viscosity ν_T and a turbulent diffusivity κ_T as $\xi \sim \nu_T/\ell^2$ and $\mu \sim \kappa_T/\ell^2$. We should also remark that the heating term in (3.33) describes a situation which is different from a real Rayleigh-Bénard problem. Indeed, the phenomenological term in (3.33) corresponds to a term $-\mu(\gamma z + T)$ on the right-hand side of eq. (3.5) which describes a spatially nonuniform *internal* heating (cooling) as opposed to the *external* heat input in real convection. In the time-independent and quiescent state $\boldsymbol{\Omega} = 0, \boldsymbol{\Theta} = \boldsymbol{\Theta}_0$ there is no heat flux. The convective heat transport can be accomplished by a simple elementary operation which consists of (i) taking a system with equilibrium distribution $T = -\gamma z$ ($\boldsymbol{\Theta} = \boldsymbol{\Theta}_0$), (ii) instantly moving all fluid particles such that the temperature distribution is inverted, i.e. $T = +\gamma z$ ($\boldsymbol{\Theta} = -\boldsymbol{\Theta}_0$, which corresponds to turning the fluid upside down), and (iii) letting the temperature relax back to thermal equilibrium. This process transports heat from the hot ($z < 0$) to the cold ($z > 0$) region of the system. Notice that the impossibility to transfer heat from a cold to a hot "reservoir" as stated by the second law of thermodynamics is embodied in the relation $\dot{\boldsymbol{\Theta}}^2 = 2\mu\boldsymbol{\Theta} \cdot (\boldsymbol{\Theta}_0 - \boldsymbol{\Theta})$ which, after time averaging in a statistically steady state implies $0 = \langle \boldsymbol{\Theta} \cdot (\boldsymbol{\Theta}_0 - \boldsymbol{\Theta}) \rangle$ and thereby excludes $\langle \boldsymbol{\Theta} \cdot \boldsymbol{\Theta}_0 \rangle < 0$ (where $\langle . \rangle$ denotes time averaging).

Let us convert the equations of motion into a non-dimensional form by measuring lengths in units of the vertical semi-axis c of the ellipsoid, times in units of the viscous decay time ξ^{-1}, and by introducing non-dimensional variables (denoted by an asterisk) according to $\mathbf{\Omega} = \xi\mathbf{\Omega}^*$, $\hat{J} = c^2\hat{J}^*$, $\mathbf{\Theta} = \gamma c\mathbf{\Theta}^*$. Furthermore, we represent the two horizontal axes of the ellipsoid as

$$a = \Gamma(1+\epsilon)\,c, \tag{3.34}$$

$$b = \Gamma(1-\epsilon)\,c, \tag{3.35}$$

where Γ is the aspect ratio and ϵ a parameter which characterizes the horizontal eccentricity h of the ellipsoid. More precisely, for the eccentricity h of an ellipse with major axis a and minor axis b it holds

$$h = \sqrt{1-\left(\frac{b}{a}\right)^2} = \sqrt{1-\left(\frac{1-\epsilon}{1+\epsilon}\right)^2}. \tag{3.36}$$

Inserting such definitions into eq. (3.32) and (3.33), and dropping the asterisks leads to the following dimensionless model

$$\hat{J}\dot{\mathbf{\Omega}} = \mathbf{\Omega}\times\hat{J}\mathbf{\Omega} + \frac{R}{\sigma}\,\mathbf{k}\times\mathbf{\Theta} - \hat{J}\mathbf{\Omega}, \tag{3.37}$$

$$\dot{\mathbf{\Theta}} = \mathbf{\Omega}\times\mathbf{\Theta} - \frac{1}{\sigma}(\mathbf{\Theta}-\mathbf{k}). \tag{3.38}$$

Here, the elements of the diagonal matrix $\hat{J}$ are now given by $J_u = 1 + \Gamma^2(1-\epsilon)^2$, $J_v = 1+\Gamma^2(1+\epsilon)^2$, $J_w = 2\Gamma^2(1+\epsilon^2)$. The thermal forcing parameter

$$R = \frac{\beta_m g\gamma}{\xi\mu} \tag{3.39}$$

and the viscous-diffusive time-scale ratio

$$\sigma = \frac{\xi}{\mu} \tag{3.40}$$

will be refered to as the pseudo-Rayleigh and the pseudo-Prandtl numbers, respectively. Their relation to the “real" (molecular) Rayleigh and Prandtl numbers will be discussed in the next subsection.

In terms of the four dimensionless parameters (Γ, ϵ, R, σ), the equations of motion read [39]:

$$\dot{u} = \frac{(1-\epsilon^2)\Gamma^2 - 1}{1+(1-\epsilon)^2\Gamma^2} vw - \frac{R}{[1+(1-\epsilon)^2\Gamma^2]\sigma}\chi - u, \tag{3.41}$$

$$\dot{v} = \frac{1-(1+\epsilon)^2\Gamma^2}{1+(1+\epsilon)^2\Gamma^2} uw + \frac{R}{[1+(1+\epsilon)^2\Gamma^2]\sigma}\varphi - v, \tag{3.42}$$

$$\dot{w} = \frac{2\epsilon}{(1+\epsilon^2)} uv - w, \tag{3.43}$$

$$\dot{\varphi} = v\psi - w\chi - \frac{1}{\sigma}\varphi, \tag{3.44}$$

$$\dot{\chi} = w\varphi - u\psi - \frac{1}{\sigma}\chi, \tag{3.45}$$

$$\dot{\psi} = u\chi - v\varphi - \frac{1}{\sigma}(\psi - 1). \tag{3.46}$$

3.3.4 Pseudo-Nusselt and pseudo-Reynolds numbers

For a given set of control parameters (R, σ, Γ, ϵ) and initial conditions $\mathbf{\Omega}(0)$, $\mathbf{\Theta}(0)$ equations (3.37) and (3.38) uniquely determine the temporal evolution of $\mathbf{\Omega}$ and $\mathbf{\Theta}$ from which the three-dimensional velocity and temperature fields can be reconstructed at any instant using eq. (3.6) and (3.7). Once a solution is known, we can define two global quantities to characterize the dynamical state, namely the pseudo-Nusselt and the pseudo-Reynolds numbers.

We define a pseudo-Nusselt number by observing that convection reduces the temperature difference $\Delta_0 = 2\gamma c$ of the quiescent state to a lower value $\Delta = 2\gamma c\,\langle\psi\rangle$ (nondimensional ψ). Therefore, the ratio $Nu = \Delta_0/\Delta$ is a measure of the effectiveness of "convective smoothing" of the basic temperature gradient. We are led to the expression:

$$Nu = \langle\psi\rangle^{-1}. \tag{3.47}$$

In terms of the solution of (3.37) and (3.38), it is also convenient to introduce the time-averaged velocity $\overline{V}$:

$$\overline{V} \equiv \xi\, c\, \langle \mathbf{\Omega}\cdot\hat{J}\mathbf{\Omega}\rangle^{1/2}, \tag{3.48}$$

and the corresponding Reynolds number:

$$Re = \frac{\overline{V}\,2c}{\nu_m}. \tag{3.49}$$

Note that $\langle \mathbf{\Omega} \cdot \hat{\jmath} \mathbf{\Omega} \rangle^{1/2}$ is the dimensionless mean-velocity. Its explicit dependence on σ and R can be written as:

$$\langle \mathbf{\Omega} \cdot \hat{\jmath} \mathbf{\Omega} \rangle^{1/2} = \frac{\overline{V}}{c} \sqrt{\frac{R}{\beta_m \gamma g \sigma}}, \tag{3.50}$$

since $\xi = \sqrt{\beta_m \gamma g \sigma / R}$, cf. eqs. (3.39) and (3.40).

In order to calibrate our model, we connect the pseudo-Rayleigh and pseudo-Prandtl numbers R and σ appearing in eq. (3.37) and (3.38) with the physical control parameters of convection, namely the Rayleigh number

$$Ra = \frac{16 \beta_m g \gamma c^4}{\nu_m \kappa_m} \tag{3.51}$$

and the Prandtl number

$$Pr = \frac{\nu_m}{\kappa_m}. \tag{3.52}$$

The factor of 16 in the definition of Ra takes care of the fact that the Rayleigh number is defined in terms of the total height of the system, which equals $2c$.

To accomplish the calibration we propose to compare the pseudo-Nusselt and pseudo-Reynolds numbers for the particular case of a sphere ($\Gamma = 1$, $\epsilon = 0$) with the Nusselt and Reynolds numbers $Nu_{RB}(Ra, Pr)$ and $Re_{RB}(Ra, Pr)$ for Rayleigh-Bénard convection inside a circular cylinder with aspect ratio one. The latter two quantities have the property $Nu_{RB} = 1$, $Re_{RB} = 0$ for $Ra \leqslant Ra_c$ where Ra_c is the critical Rayleigh number for the linear instability in a circular cylinder. Although the exact functional dependence of $Nu_{RB}(Ra, Pr)$ and $Re_{RB}(Ra, Pr)$ is partially unknown, a natural choice of the calibration is to require that the pseudo-Nusselt and pseudo-Reynolds numbers of our model be equal to those of the full Rayleigh-Bénard problem. This leads to the implicit definition $Nu(R, \sigma, 1, 0) = Nu_{RB}(Ra, Pr)$, and $Re(R, \sigma, 1, 0) = Re_{RB}(Ra, Pr)$ which determines the functions $R(Ra, Pr)$ and $\sigma(Ra, Pr)$. Since we are interested in the regime of turbulent convection, far above the threshold of the primary instability, we will not attempt to compute those functions for the whole range of Rayleigh and Prandtl numbers. We rather invoke Grossmann & Lohse's unifying scaling theory [9, 44, 46, 47]. This theory predicts the functional dependence of the Nusselt and Reynolds numbers for turbulent convection in a cylindrical convective cell with aspect ratio $\Gamma = 1$ in the form $Nu_s(Ra, Pr)$ and $Re_s(Ra, Pr)$, using a limited number of parameters determined from a series of experiments. We use the index s to denote

the quantities of the Grossmann-Lohse scaling theory. We can now calibrate our model for the turbulent regime by defining R and σ as solutions of $Nu(R,\sigma,1,0) = Nu_s(Ra,Pr)$ and $Re(R,\sigma,1,0) = Re_s(Ra,Pr)$. Then, our model is used to calculate the dynamics of the system for aspect ratios different from unity and for nonzero eccentricities, in R and σ ranges of interest.

3.4 General properties of the model

Before numerically solving the model equations (3.37) and (3.38), in this section we discuss some of their general properties and limiting cases. In subsection 3.4.1 we show that the model contains an analog of the Rayleigh-Bénard instability. In subsection 3.4.2 we demonstrate that for flow in a sphere (i.e., $h = \epsilon = 0$ and $\Gamma = 1$) the Lorenz equations are recovered.

3.4.1 Linear stability

Equations (3.37) and (3.38) admit a steady solution $\boldsymbol{\Omega} = \mathbf{0}$, $\boldsymbol{\Theta} = \mathbf{k}$ which corresponds to a quiescent state and a linear vertical temperature profile. To analyse the stability of this state we decompose the total temperature profile in the form $\boldsymbol{\Theta} = \mathbf{k} + \delta\boldsymbol{\Theta}$ and consider the evolution of infinitesimal perturbations $\delta\boldsymbol{\Omega}$, $\delta\boldsymbol{\Theta}$ of velocity and temperature, respectively. The resulting system

$$\hat{J}\,\delta\dot{\boldsymbol{\Omega}} = \frac{R}{\sigma}\,\mathbf{k}\times\delta\boldsymbol{\Theta} - \hat{J}\,\delta\boldsymbol{\Omega}, \tag{3.53}$$

$$\delta\dot{\boldsymbol{\Theta}} = \delta\boldsymbol{\Omega}\times\mathbf{k} - \frac{1}{\sigma}\delta\boldsymbol{\Theta}, \tag{3.54}$$

admits solutions with exponential time dependence of the form $\delta\boldsymbol{\Omega}(t) = \mathbf{A}\,e^{st}$, $\delta\boldsymbol{\Theta} = \mathbf{B}\,e^{st}$, where $s(R,\sigma,\Gamma,\epsilon) = \alpha + i\omega$ denotes the complex eigenvalue of the perturbation, α its growth rate, and ω its frequency. The eigenvalue problem reads:

$$s\hat{J}\mathbf{A} = \frac{R}{\sigma}\,\mathbf{k}\times\mathbf{B} - \hat{J}\mathbf{A}, \tag{3.55}$$

$$s\mathbf{B} = \mathbf{A}\times\mathbf{k} - \frac{1}{\sigma}\mathbf{B}. \tag{3.56}$$

The critical pseudo-Rayleigh number R_c is characterized by the condition $\alpha = 0$. For R below R_c, the growth rate α is negative and above R_c it is positive. The condition $\alpha = 0$ yields the threshold R_c of instability as function

of σ, Γ, and ϵ, i.e., $R_c = R_c(\sigma, \Gamma, \epsilon)$. It turns out that R_c does not depend on σ and has two branches, which can be written in the form:

$$R_{c,\pm} = 1 + \Gamma^2(1 \pm \epsilon)^2. \tag{3.57}$$

The two critical pseudo-Rayleigh numbers correspond to modes aligned with the two horizontal axes of the ellipsoid. A closer examination of these eigenmodes shows that the instability sets in as a convective roll whose axis is aligned with the longer of the two horizontal axes of the ellipsoid (axis a in our case). The threshold of the instability is independent of the pseudo-Prandtl number as it is in the real Rayleigh-Bénard instability. Steady states and secondary instabilities for special values of the geometry parameters have been discussed by Gledzer et al. [39].

3.4.2 Convection in a sphere and its relation to the Lorenz model

The particular case $\Gamma = 1$, $\epsilon = 0$ corresponding to a sphere deserves particular emphasis. In this case we have $\hat{J}\boldsymbol{\Omega} = 2\boldsymbol{\Omega}$ and $\boldsymbol{\Omega} \times \hat{J}\boldsymbol{\Omega} = 0$ so that the basic equations simplify to

$$2\dot{\boldsymbol{\Omega}} = \frac{R}{\sigma}\,\mathbf{k} \times \boldsymbol{\Theta} - 2\boldsymbol{\Omega}, \tag{3.58}$$

$$\dot{\boldsymbol{\Theta}} = \boldsymbol{\Omega} \times \boldsymbol{\Theta} - \frac{1}{\sigma}(\boldsymbol{\Theta} - \mathbf{k}). \tag{3.59}$$

A few conclusions can be drawn immediately. First, the 3-component of (3.58) is $\dot{w} = -w$, i.e., $w(t)$ decays to zero with decay rate 1 (in physical units with the kinetic decay ξ). Second, from 3.59 one finds $d(\boldsymbol{\Theta} \cdot \boldsymbol{\Omega})/dt = \boldsymbol{\Theta} \cdot \dot{\boldsymbol{\Omega}} + \dot{\boldsymbol{\Theta}} \cdot \boldsymbol{\Omega} = -(1 + \sigma^{-1})\boldsymbol{\Theta} \cdot \boldsymbol{\Omega}$, i.e., also $\boldsymbol{\Theta} \cdot \boldsymbol{\Omega} \to 0$ (in physical units with a decay rate $\xi + \mu$). Thus, after a short (molecular) transient time, only 5 variables and one constraint remain. We can simplify further, because after the transient regime it is $u(t) = \text{const}\, v(t)$. Proof: $d(u/v)/dt = v^{-2}(v\dot{u} - u\dot{v}) = v^{-2}(-R/2\sigma)(v\chi + u\varphi) = 0$. The last equality holds, because $(u\varphi + v\chi) = \boldsymbol{\Omega} \cdot \boldsymbol{\Theta} = 0$, if w has decayed. Thus, $u(t) = \text{const}\, v(t)$ move on a line. We choose this line as the u-axis and have $v = 0$. To satisfy $\boldsymbol{\Omega} \cdot \boldsymbol{\Theta} = 0 = u\varphi$, we have to take $\varphi = 0$.

The remaining equations for $\boldsymbol{\Omega} = (u, 0, 0)$ and $\boldsymbol{\Theta} = (0, \chi, \psi)$ are:

$$\frac{du}{dt} = -\frac{R\chi}{2\sigma} - u, \qquad \frac{d\chi}{dt} = -u\psi - \frac{\chi}{\sigma}, \qquad \frac{d\psi}{dt} = u\chi - \frac{(\psi - 1)}{\sigma}. \tag{3.60}$$

This set of 3 equations for the 3 variables is equivalent to the Lorenz equations [40, 41] for the particular case $b = 1$:

$$\frac{dX}{d\tau} = -\sigma X + \sigma Y, \qquad \frac{dY}{d\tau} = rX - XZ - Y, \qquad \frac{dZ}{d\tau} = XY - Z. \tag{3.61}$$

They are obtained by the substitutions $u = \sigma^{-1} X$, $\chi = -2R^{-1} Y$, $\psi = 1 - 2R^{-1} Z$, $t = \sigma\tau$, and $r = R/2$. The underlying stationary solutions:

$$X = Y = \pm\sqrt{r-1}, \tag{3.62}$$

$$Z = r - 1, \tag{3.63}$$

can be connected to (3.47) and (3.50) as follows. First, using equation (3.63) one obtains $\langle\psi\rangle = 2/R$ and hence R is related to (3.47) as:

$$R = 2\,Nu. \tag{3.64}$$

Second, from equation (3.62), the dimensionless mean-velocity can be written as:

$$\langle \boldsymbol{\Omega} \cdot \hat{\jmath}\boldsymbol{\Omega} \rangle^{1/2} = \left\langle \frac{2X^2}{\sigma^2} \right\rangle^{1/2} = \frac{1}{\sigma}\sqrt{R-2}.$$

Since $\langle \boldsymbol{\Omega} \cdot \hat{\jmath}\boldsymbol{\Omega} \rangle^{1/2}$ is given by (3.50), let:

$$\frac{\overline{V}}{c}\sqrt{\frac{R}{\beta_m\,\gamma\,g\,\sigma}} = \frac{1}{\sigma}\sqrt{R-2}.$$

Here, using (3.49), (3.51), (3.52), and (3.64) one finally obtains:

$$\sigma = \left[(1 - Nu^{-1})\,\frac{Ra}{4\,Pr\,Re^2} \right]^{1/4}. \tag{3.65}$$

3.4.3 Role of the geometrical parameters

We comment on the role of the geometrical parameters Γ and ϵ:

1. Since the Rayleigh number Ra can be varied by changing the height of the container (cf. section 3.2), Γ and Ra are intrinsically coupled. This imposes constraints in the model's four-dimensional parameter space Γ, ϵ, σ, R, most notably in the $\Gamma \times R$ subspace.

2. For a given aspect ratio, ϵ acts as a *free* perturbation parameter. In particular, $\epsilon = 0$ is a *sufficient* condition for the exponential time-decay of the velocity amplitude $w(t)$, which weakens the w-related nonlinearities in eqs. (3.41)-(3.46) and leads to simplifications similar to those discussed in section 3.4.2 (e.g. $u(t)/v(t) = \text{const.}$, etc.). In fact, only for sufficiently large ϵ the w-nonlinearities are capable to disturb the constancy of the ratio $u(t)/v(t)$ and lead to azimuthal dynamics [see eq. (3.72)].

In view of the above considerations, the following question arises: Is there an ϵ-range for which coherent oscillations (resembling those seen in experiment and discussed in section 3.2) set in? A proper answer to this question would require a comprehensive scan of the parameter space, which is not the aim of the present chapter. Instead, we will focus the numerical analysis of the model on the dynamics of the azimuthal angle $\phi(t)$ for a limited range of aspect ratios, namely, those which we have also studied in experiment, $1.13 \leqslant \Gamma \leqslant 1.36$.

3.5 Comparing the numerical with the experimental results

3.5.1 Calibration of the parameters σ and R

We now want to integrate the dynamical equations (3.37) and (3.38) for parameters corresponding to the experimental situation discussed in section 3.2. To calibrate the parameters σ and R, we employ eqs. (3.64)-(3.65) and invoke the Grossmann-Lohse theory for the dependences $Nu(Ra, Pr)$ and $Re(Ra, Pr)$. The resulting model parameters R, σ, ξ, and μ for the three aspect ratios and Rayleigh numbers studied in section 3.2 are listed in table 3.2.

3.5.2 Modulus and azimuthal angle of the large scale roll

We want to compare the model results with the experimental measurements of the modulus and direction of the horizontal large scale wind, measured a little bit below the center of the upper plate. In general, the components of the velocity field $\mathbf{V}(x, y, z, t) = V_x\,\mathbf{i} + V_y\,\mathbf{j} + V_z\,\mathbf{k}$ can be

Parameter	Experiment 1	Experiment 2	Experiment 3
2c [cm]	6.32×10^2	5.76×10^2	5.25×10^2
γ [K cm^{-1}]	6.32×10^{-2}	6.94×10^{-2}	7.61×10^{-2}
Ra	7.3×10^{11}	5.5×10^{11}	4.2×10^{11}
Re	7.87×10^4	6.95×10^4	6.15×10^4
Nu	4.96×10^2	4.54×10^2	4.15×10^2
R	9.92×10^2	9.07×10^2	8.29×10^2
σ	2.54	2.51	2.50
ξ [s^{-1}]	2.30×10^{-2}	2.51×10^{-2}	2.74×10^{-2}
μ [s^{-1}]	9.05×10^{-3}	9.96×10^{-3}	1.10×10^{-2}

Table 3.2: Model parameters for the three experiments studied in section 3.2: $Pr = 0.71$, $\Delta = 40\,K$, $\gamma = \Delta/(2c)$, $\beta_m = (300\,K)^{-1}$, and $g = 981\,cm/s^2$. The model parameters R and σ are calibrated via Grossmann-Lohse theory [cf. eqs. (3.64)-(3.65)]. The phenomenological viscous and thermal decay rates $\xi = \sqrt{\beta_m\, g\, \gamma\, \sigma\, R^{-1}}$ and $\mu = \xi\, \sigma^{-1}$ are determined by eqs. (3.39)-(3.40). The first three rows of the table contain the input-data from the experiments, whereas the remaining seven rows show the results of the calibration procedure.

written as

$$V_x(y,z,t) = \frac{(1+\epsilon)}{(1-\epsilon)}\,(z\,v - y\,w)\,\xi\,c, \tag{3.66}$$

$$V_y(x,z,t) = \frac{(1-\epsilon)}{(1+\epsilon)}\,(x\,w - z\,u)\,\xi\,c, \tag{3.67}$$

$$V_z(x,y,t) = \frac{1}{(1-\epsilon^2)}\,(y\,u - x\,v)\,\xi\,c. \tag{3.68}$$

For points along the vertical center axis of the ellipsoid, i.e., $(x = 0, y = 0, -1 \leqslant z \leqslant 1)$, the velocity components are simplified to

$$V_x(0,z,t) = \frac{(1+\epsilon)}{(1-\epsilon)}\,z\,v\,\xi\,c, \tag{3.69}$$

$$V_y(0,z,t) = -\frac{(1-\epsilon)}{(1+\epsilon)}\,z\,u\,\xi\,c, \tag{3.70}$$

$$V_z(0,0,t) = 0. \tag{3.71}$$

The horizontal velocities at the top ($z = 1$) and bottom ($z = -1$) of the vertical center axis are componentwise anticorrelated, i.e.,

$$(V_x(0,1,t), V_y(0,1,t), 0) \;=\; -(V_x(0,-1,t), V_y(0,-1,t), 0),$$

just as expected and seen in experiment [20]. The azimuthal angle of the large scale velocity projected into the x,y-plane is

$$\phi(t) = \arctan\left(\frac{V_y}{V_x}\right) = \arctan\left[-\frac{(1-\epsilon)^2}{(1+\epsilon)^2}\frac{u}{v}\right]. \tag{3.72}$$

3.5.3 Numerical integration of the model ODEs

The coupled ODEs (3.41)-(3.46) for the six amplitudes $u, v, w, \varphi, \chi, \psi$ have been numerically integrated. The control parameters are Γ, ϵ characterizing the geometry of the container (here the ellipsoid) and R, σ as the external control parameters. R and σ correspond to the choices of the Rayleigh number Ra and the Prandtl number Pr, as discussed. The numerical scheme is based on the fourth-order Runge-Kutta method with adaptive stepsize control in time [50]. We obtain time series for the six amplitudes $u(t)$, $v(t)$, $w(t)$, $\phi(t)$, $\chi(t)$, and $\phi(t)$ from which we calculate the modulus and azimutal angle of the horizontal velocity, as described in subsection 3.5.2. To validate the computer code, we have integrated the equations of motion for $\epsilon = 0$ and $\Gamma = 1$ and compared the results with the analytically known properties discussed in section 3.4.2. E.g., indeed we find that for large t the mode $w(t)$ decays exponentially and that the ratio $u(t)/v(t)$ is constant as a function of time, etc.

3.5.4 Dependence on the eccentricity

We now come to the case of finite eccentricity $\epsilon > 0$. Table 3.3 provides a rough impression about the role of ϵ in the dynamics of the direction $\phi(t)$ of the large scale horizontal wind.

Starting at small values ($\epsilon < 0.02$), no angular dynamics is observed. As discussed above, such absence of rotation can be traced to the exponential decay of $w(t)$. For $0.02 < \epsilon < 0.06$, a periodic or chaotic dynamics emerge (e.g. as in figure 3.4(a)). Increasing ϵ even further – from 0.06 to 0.7 – the angle becomes unbounded, i.e., the effective change of $\phi(t)$ covers multiples of 2π rotations (e.g. as in figure 3.4(b)).

Ultimately, for $\epsilon \uparrow 1$ the angular dynamics becomes bounded again, because the ellipsoid tends to degenerate into an ellipse with vertical semi-axis c and horizontal semi-axis a, while the other horizontal semi-axis

ϵ	$\phi(t)$
$[0.00; 0.02]$	constant
$[0.02; 0.04]$	periodic, bounded
$[0.04; 0.06]$	periodic/chaotic, bounded
$[0.06; 0.7]$	chaotic/periodic, unbounded
$[0.7; 1.0[$	periodic/constant, bounded

Table 3.3: Dynamics of the azimuthal angle $\phi(t)$ as function of the perturbation parameter ϵ, for $1.13 \leqslant \Gamma \leqslant 1.24$.

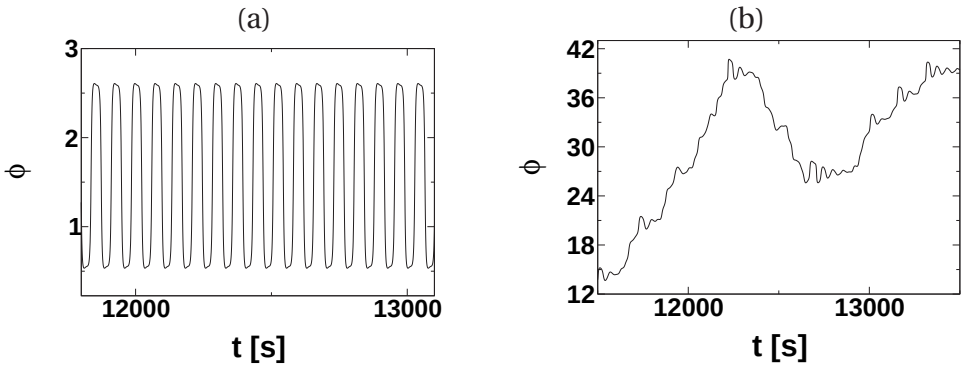

Figure 3.4: Horizontal angle ϕ [rad] dynamics for $\Gamma = 1.36$. In (a) the eccentricity parameter is $\epsilon = 0.03$ and the angle oscillates with period 71 sec. In (b) $\epsilon = 0.3$ and the angular dynamics is chaotic and unbounded.

vanishes $b = 0$. In this extreme case, ϕ is obviously constant. Therefore, since we are particularly interested in the case of small eccentricity and bounded angular dynamics, we set $\epsilon = 0.054$ in all our subsequent computations corresponding to the sequence periodic/chaotic-bounded in table 3.

3.5.5 Model results on the large-scale wind dynamics

Velocity field visualization

In figure 3.5 we show a snapshot of the velocity field, projected into the yz-plane. This kind of visualization best reveals the basic structure of the flow: an elliptical large-scale circulation with decreasing magnitude to-

wards the origin $(x = 0, y = 0, z = 0)$, where the fluid remains at rest [cf. equation (3.6)].

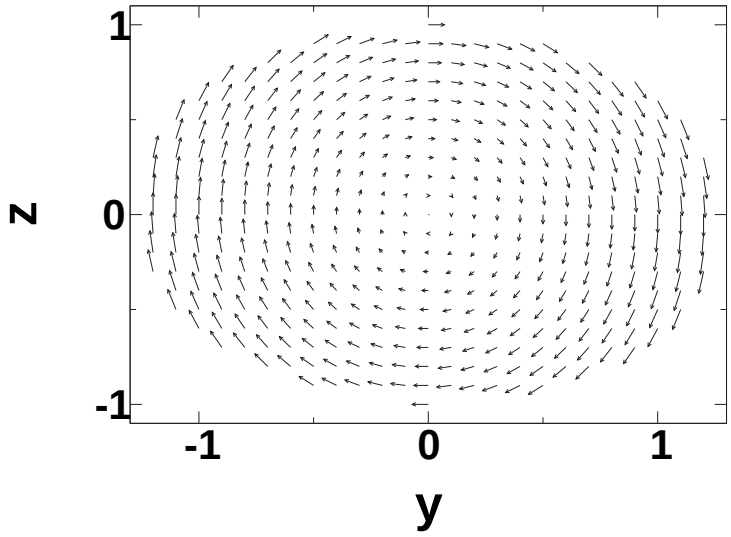

Figure 3.5: Velocity field projected into the yz-plane of an ellipsoid with aspect ratio $\Gamma = 1.36$ and eccentricity parameter $\epsilon = 0.054$. Snapshot taken at $t = 500$.

In particular, for points along z-axis, the velocity components V_x and V_y (the latter visible in fig. 3.5) involve two amplitudes only, namely: u and v [see equations (3.69)-(3.71)]. Thus, in consistence with the experimental measurements discussed in section 3.2, we fix $(x = 0, y = 0, z = 0.99)$ as the probing position and then compute the resultant velocity.

Dependence of the mean velocity on the aspect ratio Γ

Denote the amplitude of the horizontal velocity at $(x = 0, y = 0, z = 0.99)$ by $V(t) = \sqrt{V_x^2(t) + V_y^2(t)}$. We consider a typical behavior of $V(t)$: For $\Gamma = 1.36$ and $\epsilon = 0.054$, figure 3.6 shows that $V(t)$ oscillates around the mean value $\overline{V} \approx 0.4$ m/s. A Fourier analysis reveals that more than one frequency is involved.

We now focus on how the mean and root-mean-square velocities vary with Γ. As shown in table 3.4, the numerical results for the mean velocity have the same order of magnitude of the experimental values presented

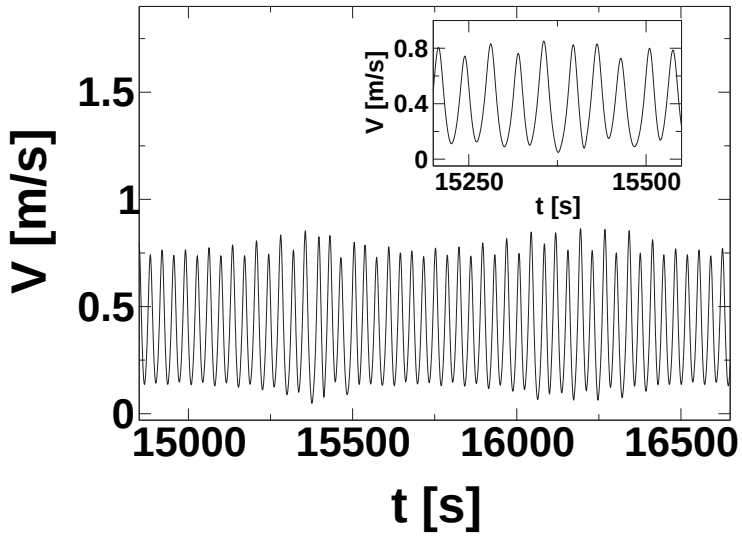

Figure 3.6: Time series of the velocity amplitude for $\Gamma = 1.36$ and $\epsilon = 0.054$. The time series for the other two aspect ratios look similiar.

in section 3.2. However, concerning the aspect-ratio-dependence of $\overline{V}$, the trends observed in theory and experiment are different: According to the model, $\overline{V}$ decreases as Γ is increased, while the experimental measurements show the opposite – a monotonic increase of $\overline{V}$ with Γ. We cannot explain this difference yet.

Experiment	Γ	$\overline{V}_{exp}$ [m/s]	$\overline{V}$ [m/s]	V_{rms} [m/s]
1	1.13	0.544	0.525	0.287
2	1.24	0.585	0.475	0.256
3	1.36	0.649	0.428	0.233

Table 3.4: Comparison between the theoretically computed velocities and the experimental measurements. The respective parameter sets are listed in table 3.2, with $\epsilon = 0.054$ supplemented in all cases.

Dynamics of the azimuthal angle of the horizontal wind

Figure 3.7 shows a typical time series $\phi(t)$ for aspect ratio $\Gamma = 1.13$ and $\epsilon = 0.054$. In this case, the azimuthal angle is confined to the interval $[0, \pi]$, with oscillations around the mean value $\langle\phi\rangle \approx \pi/2$. Note that when ϕ approaches its largest/smallest values in the interval an almost π-rotation is triggered. Such event occurs in a relatively short time scale ($\approx 0.1\xi^{-1} \approx 4s$), and as shown in the inset of figure 3.7 such fast rotation is not an artificial jump due to discontinuities of the arctan function in eq. (3.72).

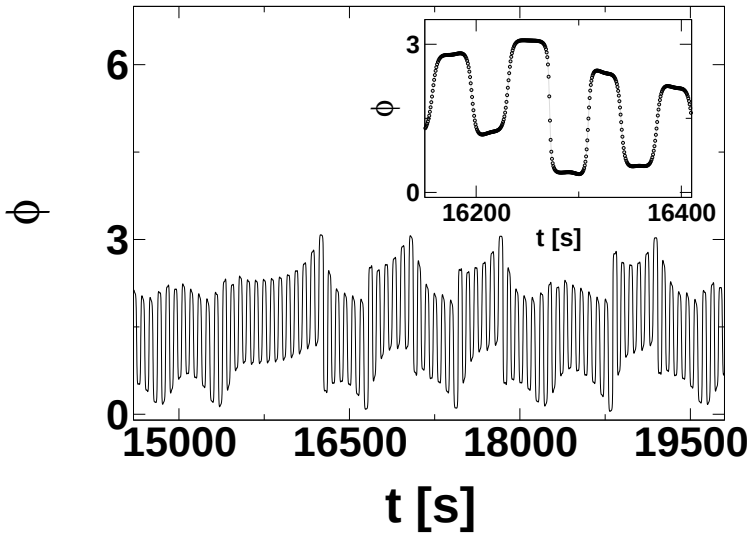

Figure 3.7: Time series of the azimuthal angle of the large scale circulation for $\Gamma = 1.13$ and $\epsilon = 0.054$. The time series for the other two aspect ratios look similiar.

Autocorrelation of the direction of the horizontal wind

To analyse the temporal behavior of the orientation $\phi(t)$ of the vertical plane of the large scale flow further, we consider its autocorrelation function defined by

$$C_\phi(\tau) = \frac{\langle \delta\phi(t)\, \delta\phi(t+\tau)\rangle}{\langle [\delta\phi(t)]^2\rangle},$$

where $\delta\phi(t) = \phi(t) - \langle\phi\rangle$ denotes the fluctuation of the angle, and τ the delay time (dimensionalized by ξ^{-1}).

Figures 3.8b, d, and f show the behavior of the autocorrelation function for the three different sets of Rayleigh numbers and aspect ratios which we have studied in the experiments of section 3.2, see figure 3.3b, d, and f. The figures 3.8b, d, and f are the main theoretical result of this chapter: First, the figures show the oscillations of the horizontal wind direction on a time-scale comparable to the large eddy turnover time. Second, just as found in experiment (section 3.2), the wind direction displays long memory lasting for hundreds of large eddy turnover times.

In table 3.5 the typical times between two peaks obtained from the model (τ_p^{model}) are compared with the values measured experimentally (τ_p^{exp}). We find that the peak-to-peak times calculated from the model are the same order of magnitude as the measured values. That the values do not agree is of course not surprising, given the approximations of the model, in particular, given the different velocity boundary conditions (free-slip in the model versus no-slip in the experiment).

Experiment	τ_p^{model} [s]	τ_p^{exp} [s]
1	70.1	42.1
2	68.2	39.5
3	72.8	38.2

Table 3.5: Comparison between the peak-to-peak times obtained from the model τ_p^{model} and the experimental measurements τ_p^{exp}. The parameter sets of the three experiments are listed in table 3.2.

For completeness, we also show the speed autocorrelation $C_V(\tau)$, see figures 3.8a, c, and e. In contrast to the experimental results, see figures 3.3a, c, and e, it also shows memory effects. Given that our theoretical model does not include small scale velocity fluctuations caused by plumes and the turbulence activity, this shortcoming had to be expected. The correlation time of the velocity autocorrelation is half of that of the angular autocorrelation. This could already be concluded from the time series for the speed and the angle, see the insets of figures 3.6 and 3.7: While the angle covers half a period, the modulus of the velocity covers a full period.

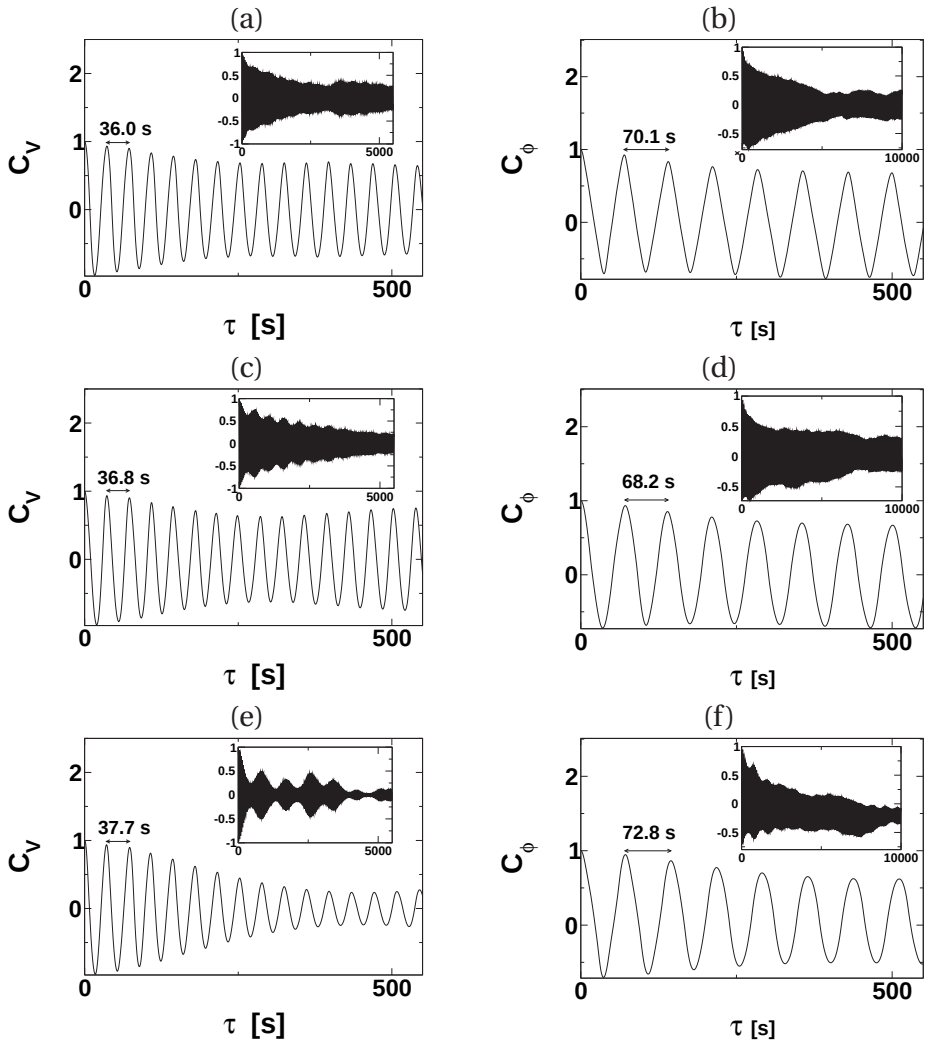

Figure 3.8: Autocorrelation functions $C_V(\tau)$ of the speed $V(t)$ (plates (a), (c), and (e)) and $C_\phi(\tau)$ of the azimuthal angle $\phi(t)$ of the vertical plane of the wind, resulting from the model equations. In (a) and (b) the Rayleigh number is $Ra = 7.3 \times 10^{11}$ and the aspect ratio $\Gamma = 1.13$; in (c) and (d) $Ra = 5.5 \times 10^{11}$ and $\Gamma = 1.24$; in (e) and (f) $Ra = 4.3 \times 10^{11}$ and $\Gamma = 1.36$. This figure is to be compared with the experimental result shown in figure 3.3. Both experimental and theoretical angle correlations signal that s (i) the oscillatory behavior of the wind direction and (ii) long memory effects. The correlations in the theoretical speed correlation $C_V(\tau)$ reflects the lack of small scale fluctuations in our model equations.

3.6 Discussion and conclusions

In summary, we have analyzed the wind of turbulence in thermally driven turbulence both experimentally and within a model for very large Rayleigh numbers $\mathrm{Ra} \approx 4 \cdot 10^{11} - 7 \cdot 10^{11}$ and $\mathrm{Pr} = 0.71$. The most important result of this chapter is that the oscillations of the large scale wind can be well described with a simple model for the *bulk* flow dynamics only. The boundary layers and the plumes detaching from them are not needed to account for the properties of the oscillations. We therefore call them "inertial oscillations". The analogy between the experimental and the numerical results for the oscillations of the large scale wind direction holds with respect to their typical frequency, their typical amplitude, and also their extremely large angular auto-correlation time, i.e., the very long memory of the large-scale wind for its flow. The figures demonstrating the analogy between experiment and the simple inertial model are in particular figures 3.3b, d, f and figures 3.8b, d, f, respectively.

Our finding that the oscillations of the flow direction are intrinsic to the large scale wind are consistent with Funfschilling and Ahlers's earlier experimental results for much lower Rayleigh number and different Prandtl numbers [20], but at variance with earlier speculations which seek the origin of the oscillations in details of the BL and plume interaction with the bulk flow: Our inertial model does not know anything of the plumes or the boundary layers. Our results differ from recent measurements by Xi et al [45] in that we see oscillations only in the angle of the large-scale flow, not in its magnitude. It is possible that these oscillations are of different origin and only the angular oscillations are inertial in their nature.

In this sense the weak side of the dynamical model, namely its obviously unphysical properties such as free-slip boundary conditions and therefore the absense of any realistic boundary layer dynamics, also turns out to be at the same time the strong side of the model: We show that the BL and the plumes do not seem to be necessary to account for the wind direction oscillations. They simply occur as intrinsic precession of the bulk flow. We have however to admit that being able to reproduce a phenomenon does not necessarily mean the model is based on the right mechanism. It is therefore necessary to apply the model to other experiments in future in order to assess its predictive power in a comprehensive manner.

Acknowledgments

The authors thank Guenter Ahlers for stimulating discussions. A.T., R. d. P. and C. R. acknowledge the Deutsche Forschungsgemeinschaft (DFG) for financial support of the experimental work at Ilmenau University of Technology in frame of the "Interdisziplinäre Turbulenzinitiative". F. F. A., S. G., and D. L. thank the Stichting voor Fundamenteel Onderzoek der Materie (FOM), which is financially supported by the Nederlandse Organisatie voor Wetenschappelijk Onderzoek (NWO), for financial support.

References

[1] R. KRISHNAMURTI and L. N. HOWARD, Large scale flow generation in turbulent convection, *Proc. Natl. Acad. Sci.* **78**, 1981 (1981).

[2] M. SANO, X. Z. WU, and A. LIBCHABER, Turbulence in helium-gas gree-convection, *Phys. Rev. A* **40**, 6421 (1989).

[3] B. CASTAING, G. GUNARATNE, F. HESLOT, L. KADANOFF, A. LIBCHABER, S. THOMAE, X. Z. WU, S. ZALESKI, and G. ZANETTI, Scaling of hard thermal turbulence in Rayleigh-Bénard convection, *J. Fluid Mech.* **204**, 1 (1989).

[4] G. ZOCCHI, E. MOSES, and A. LIBCHABER, Coherent structures in turbulent convection: an experimental study, *Physica A* **166**, 387 (1990).

[5] E. D. SIGGIA, High Rayleigh number convection, *Annu. Rev. Fluid Mech.* **26**, 137 (1994).

[6] E. VILLERMAUX, Memory-induced low frequency oscillations in closed convection boxes, *Phys. Rev. Lett.* **75**, 4618 (1995).

[7] Y. B. XIN, K.-Q. XIA, and P. TONG, Measured velocity boundary layers in turbulent convection, *Phys. Rev. Lett.* **77**, 1266 (1996).

[8] S. CIONI, S. CILIBERTO, and J. SOMMERIA, Strongly turbulent Rayleigh-Bénard convection in mercury: comparison with results at moderate Prandtl number, *J. Fluid Mech.* **335**, 111 (1997).

[9] S. GROSSMANN and D. LOHSE, Scaling in thermal convection: A unifying view, *J. Fluid. Mech.* **407**, 27 (2000).

[10] X. L. QIU and P. TONG, Large-scale coherent rotation and oscillation in turbulent thermal convection, *Phys. Rev. E* **61**, R6075 (2000).

[11] L. P. KADANOFF, Turbulent heat flow: Structures and scaling, *Phys. Today* **54**, 34 (2001).

[12] X. L. QIU and P. TONG, Onset of coherent oscillations in turbulent Rayleigh-Bénard convection, *Phys. Rev. Lett* **87**, 094501 (2001).

[13] X. L. QIU and P. TONG, Large scale velocity structures in turbulent thermal convection, *Phys. Rev. E* **64**, 036304 (2001).

[14] J. NIEMELA, L. SKRBEK, K. R. SREENIVASAN, and R. J. DONNELLY, The wind in confined thermal turbulence, *J. Fluid Mech.* **449**, 169 (2001).

[15] K. R. SREENIVASAN, A. BERSHADSKI, and J. NIEMELA, Mean wind and its reversals in thermal convection, *Phys. Rev. E* **65**, 056306 (2002).

[16] R. VERZICCO, Turbulent thermal convection in a closed domain: viscous boundary layer and mean flow effects, *Eur. Phys. J. B* **35**, 133 (2003).

[17] K.-Q. XIA, C. SUN, and S. Q. ZHOU, Particle image velocimetry measurement of the velocity field in turbulent thermal convection, *Phys. Rev. E* **68**, 066303 (2003).

[18] H. D. XI, S. LAM, and K.-Q. XIA, From laminar plumes to organized flows: the onset of large-scale circulation in turbulent thermal convection, *J. Fluid Mech.* **503**, 47 (2004).

[19] X. L. QIU, X. D. SHANG, P. TONG, and K.-Q. XIA, Velocity oscillations in turbulent Rayleigh-Bénard convection, *Phys. Fluids.* **16**, 412 (2004).

[20] D. FUNFSCHILLING and G. AHLERS, Plume motion and large scale circulation in a cylindrical Rayleigh-Bénard cell, *Phys. Rev. Lett.* **92**, 194502 (2004).

[21] F. FONTENELE ARAUJO, S. GROSSMANN, and D. LOHSE, Wind reversals in turbulent Rayleigh-Bénard convection, *Phys. Rev. Lett.* **95**, 084502 (2005).

[22] Y. TSUJI, T. MIZUNO, T. MASHIKO, and M. SANO, Mean Wind in Convective Turbulence of Mercury, *Phys. Rev. Lett.* **94**, 034501 (2005).

[23] E. BROWN, D. FUNFSCHILLING, and G. AHLERS, Reorientation of the large-scale circulation in turbulent Rayleigh-Bénard convection, *Phys. Rev. Lett.* **95**, 084503 (2005).

[24] C. SUN, K. Q. XIA, and P. TONG, Three-dimensional flow structures and dynamics of turbulent thermal convection in a cylindrical cell, *Phys. Rev. E* **72**, 026302 (2005).

[25] C. SUN, H. D. XI, and K. Q. XIA, Azimuthal symmetry, flow dynamics, and heat transport in turbulent thermal convection in a cylinder with an aspect ratio of 0.5, *Phys. Rev. Lett.* **95**, 074502 (2005).

[26] G. STRINGANO and R. VERZICCO, Mean flow structure in thermal convection in a cylindrical cell of aspect-ratio one half, *J. Fluid Mech.* **548**, 1 (2006).

[27] G. AMATI, K. KOAL, F. MASSAIOLI, K. R. SREENIVASAN, and R. VERZICCO, Turbulent thermal convection at high Rayleigh numbers for a constant-Prandtl-number fluid under Boussinesq conditions, *Phys. Fluids* **17**, 121701 (2005).

[28] M. VAN REEUWIJK, H. J. J. JONKER, and K. HANJALIC, Identification of the wind in Rayleigh-Bénard convection, *Phys. Fluids* **17**, 051704 (2005).

[29] E. BROWN, D. FUNFSCHILLING, A. NIKOLAENKO, and G. AHLERS, Heat transport by turbulent Rayleigh-Bénard convection: Effect of finite top- and bottom conductivity, *Phys. Fluids* **17**, 075108 (2005).

[30] F. HESLOT, B. CASTAING, and A. LIBCHABER, Transition to turbulence in helium gas, *Phys. Rev. A* **36**, 5870 (1987).

[31] X. L. QIU and P. TONG, Temperature oscillations in turbulent Rayleigh-Benard convection, *Phys. Rev. E* **66**, 026308 (2002).

[32] U. HANSEN, D. A. YUEN, and S. E. KROENING, Mass and heat-transfer in strongly time-dependent thermal convetion at infinite Prandtl number, *Geophys. Astrophys. Fluid Dyn.* **63**, 67 (1992).

[33] A. FURUKAWA and A. ONUKI, Convective heat transport in compressible fluids, *Phys. Rev. E* **66**, 016302 (2002).

[34] P. E. ROCHE, B. CASTAING, B. CHABAUD, and B. HEBRAL, Prandtl and Rayleigh numbers dependences in Rayleigh-Bénard convection, *Europhys. Lett.* **58**, 693 (2002).

[35] F. CHILLA, A. RASTELLO, S. CHAUMAT, and B. CASTAING, Long relaxation times and tilt sensitivity in Rayleigh Benard turbulence, *Euro. Phys. J. B* **40**, 223 (2004).

[36] R. VERZICCO and R. CAMUSSI, Numerical experiments on strongly turbulent thermal convection in a slender cylindrical cell, *J. Fluid Mech.* **477**, 19 (2003).

[37] R. DU PUITS, C. RESAGK, A. TILGNER, F. H. BUSSE, and A. THESS, Structure of thermal boundary layers in turbulent Rayleigh-Bénard convection, *J. Fluid Mech.* **572**, 231 (2007).

[38] F. V. DOLZHANSKY, On the hydrodynamic interpretation of the equations for the movement of a heavy top (in Russian), *Izv. Akad. Nauk, Fiz. Atmos. Okeana* **13**, 201 (1977).

[39] E. B. GLEDZER, F. V. DOLZHANSKY, and A. M. OBUKHOV, *Systems of hydrodynamic type and their applications (in Russian)*, Nauka, Moscow, 1981.

[40] E. N. LORENZ, Deterministic nonperiodic flow, *J. Atmos. Sci* **20**, 130 (1963).

[41] C. SPARROW, *The Lorenz equations: bifurcations, chaos, and strange attractors*, Springer-Verlag, Berlin, Heidelberg, 1982.

[42] S. H. STROGATZ, *Nonlinear dynamics and chaos*, Perseus Press, Reading, 1994.

[43] S. WIGGENS, *Introduction to Applied Nonlinear Dynamical Systems and Chaos*, Springer Verlag, Heidelberg, 1990.

[44] S. GROSSMANN and D. LOHSE, Prandtl and Rayleigh number dependence of the Reynolds number in turbulent thermal convection, *Phys. Rev. E* **66**, 016305 (2002).

[45] H.-D. XI, Q. ZHOU, and K.-Q. XIA, Azimuthal motion of the mean wind in turbulent thermal convection, *Phys. Rev. E* **73**, 056312 (2006).

[46] S. GROSSMANN and D. LOHSE, Thermal convection for large Prandtl number, *Phys. Rev. Lett.* **86**, 3316 (2001).

[47] S. GROSSMANN and D. LOHSE, Fluctuations in turbulent Rayleigh-Bénard convection: The role of plumes, *Phys. Fluids* **16**, 4462 (2004).

[48] U. BROSA and S. GROSSMANN, Hydrodynamic vector potentials, *Eur. Phys. J. B* **26**, 121 (2002).

[49] J. PEDLOSKY, *Geophysical fluid dynamics*, Springer-Verlag, Berlin, Heidelberg, 1987.

[50] W. PRESS, S. TEUKOLSKY, W. VETTERLING, and B. FLANNERY, *Numerical Recipes*, Cambridge University Press, Cambridge, 1986.

4

Non-Oberbeck-Boussinesq effects in water*

Non-Oberbeck-Boussinesq (NOB) effects on the Nusselt number Nu and Reynolds number Re in strongly turbulent Rayleigh-Bénard convection in liquids were investigated both experimentally and theoretically. In the experiment, the heat current, the temperature difference, and the temperature at the horizontal mid-plane were measured. Three cells of different heights L, all filled with water and all with aspect ratio Γ close to 1, were used. For each L, about 1.5 decades in the Rayleigh number Ra were covered, together spanning the range $10^8 \leqslant \mathrm{Ra} \leqslant 10^{11}$. For the largest temperature difference between the bottom and top plates of $\Delta = 40$K the kinematic viscosity and the thermal expansion coefficient, due to their temperature dependence, varied by more than a factor of two. The Oberbeck-Boussinesq (OB) approximation of temperature independent material parameters thus was no longer valid. The ratio χ of the temperature drops across the bottom and top thermal boundary layers became as small as $\chi = 0.83$, as compared to the ratio $\chi = 1$ in the OB case. Nevertheless, the Nusselt number Nu was found to be only slightly smaller (at most 1.4%) than in the next larger cell with the same Rayleigh number, where the material parameters were still nearly height-independent. The Reynolds numbers in the OB and NOB case agreed with each other within the experimental resolution of

*Published as: G. Ahlers, E. Brown, F. Fontenele Araujo, D. Funfschilling, S. Grossmann, D. Lohse. Non-Oberbeck-Boussinesq effects in strongly turbulent Rayleigh-Bénard convection, *J. Fluid Mech.* **569**, 409-445, (2006). F.F.A. is responsible for section 4.6.

about 2%, showing that NOB effects for this parameter were small as well. Thus Nu and Re are rather insensitive against even significant deviations from OB conditions. Theoretically, we first account for the robustness of Nu with respect to NOB corrections: the NOB effects in the top boundary layer cancel those which arise in the bottom boundary layer as long as they are linear in the temperature difference Δ. The net effects on Nu are proportional to Δ^2 and thus increase only slowly and still remain minor despite drastic material parameter changes. We then extend the Prandtl-Blasius boundary-layer theory to NOB Rayleigh-Bénard flow with temperature dependent viscosity and thermal diffusivity. This allows the calculation of the shift of the bulk temperature, the temperature drops across the boundary layers, and the ratio χ without introducing any fitting parameter. The calculated quantities are in very good agreement with experiment. When in addition we use the experimental finding that for water the sum of the top and bottom thermal boundary-layer widths (based on the slopes of the temperature profiles at the plates) remains unchanged under NOB effects within experimental resolution, the theory also gives the measured small Nusselt-number reduction for the NOB case. In addition, it predicts an increase by about 0.5% of the Reynolds number, which is also consistent with the experimental data. By theoretically studying hypothetical liquids, for which only one of the material parameters is temperature dependent, we shed further light on the origin of NOB corrections in water: While the NOB deviation of χ from its OB value $\chi = 1$ mainly originates from the temperature dependence of the viscosity, the NOB correction of the Nusselt number primarily originates from the temperature dependence of the thermal diffusivity. Finally, we give the predictions from our theory for the NOB corrections if glycerol is used as operating liquid.

4.1 Introduction

Controlled experiments on Rayleigh-Bénard (RB) convection are normally done with relatively small temperature differences Δ between the top and the bottom plate, so that the Oberbeck-Boussinesq (OB) approximation

can be used. That approximation assumes that the material properties such as the kinematic viscosity ν, the thermal diffusivity κ, the heat conductivity Λ, the isobaric specific heat capacity c_p, and the isobaric thermal expansion coefficient β can be considered to be temperature independent and thus to have constant values all over the cell [1, 2]. However, in order to achieve large Rayleigh numbers Ra, one would like to make Δ as large as possible. One of the relatively well analyzed effects due to deviations from OB conditions is that the temperature drops across the top and the bottom thermal boundary layers [3, 4] become different, i.e., an asymmetry with respect to the mid-plane of the cell shows up. However, it is unclear what the associated NOB effects on the Nusselt number Nu and the Reynolds number Re are. Nonetheless,it is often argued in very general terms that NOB effects are responsible for some measured large Ra peculiarities in Nu or Re. The lack of our understanding of possible NOB effects at large Ra on Nu and Re measurements are the more unsatisfactory, as it is this large Ra regime where the crossover to an ultimate scaling regime $Nu \sim Ra^{1/2}$ is expected [5]. In helium gas beyond $Ra \approx 10^{11}$ Chavanne *et al.* [6, 7] find a steeper increase of the logarithmic slope of the $Nu(Ra)$ curve as compared to Niemela *et al.* [8, 9] and associate this finding with the ultimate Kraichnan regime. However, there is a major controversy on whether these and other large Ra data are "contaminated" by NOB effects or not [6–13].

The aim of this chapter is to first present systematic measurements of NOB effects on the Nusselt number Nu, the Reynolds number Re, and on the center temperature T_c of the cell, and then to theoretically understand these NOB effects. We do so by extending the Prandtl-Blasius boundary layer theory to the case of temperature dependent viscosity and thermal diffusivity and apply it to NOB Rayleigh-Bénard flow. Our results hold for liquids, whose specific heat capacity c_p and density ρ except for buoyancy are temperature independent in sufficiently good approximation, and if the flow is incompressible.

For small Ra close to the transition to convection and pattern formation NOB effects were treated theoretically by various authors, and most systematically by Busse [14]. They were examined experimentally [15–20]; and reviewed in ref. [21].

The outline of the chapter is as follows: In Sect. 4.2 we introduce our notations and define quantitative measures of NOB effects. These include different thicknesses of the thermal boundary layers (BL) as well as different temperature drops at the bottom and the top plates. In section 4.3 we present our experimental results for the various measures of NOB effects,

in particular for Nu and Re. We find robustness of Nu and Re towards NOB effects which we try to rationalize in section 4.4. In section 4.5 we briefly review the model of Wu & Libchaber [3] and Zhang *et al.* [4], who analyzed NOB effects on RB flow with cryogenic helium gas and with glycerin, both experimentally and theoretically. We compare the predictions of their model with our data for water. Although they correctly predict the robustness of Nu with respect to NOB effects and even account for the very small Nu *decrease* for the NOB case, it turns out that one of the basic assumptions of the model is not fulfilled. In Section 4.6 we apply an extended Prandtl-Blasius boundary layer theory to the NOB Rayleigh-Bénard flow, giving excellent agreement for the center temperature, the Nusselt number, and the Reynolds number with the measured data. Section 4.7 contains the conclusions.

4.2 Characterization of non-Oberbeck-Boussinesq effects

4.2.1 Control parameters

What fluid properties should be used to define the non-dimensional numbers of non-Oberbeck-Boussinesq Rayleigh-Bénard flow? Since the commonly used control parameters are the temperatures T_b and T_t at the bottom and top plates, the immediate choice of a reference temperature to characterize the typical material properties is the mean temperature $T_m = (T_t + T_b)/2$. The overall temperature drop is $\Delta = T_b - T_t$. The corresponding definition of the parameters describing the thermal convection is the Rayleigh number

$$Ra_m = \frac{\beta_m g \Delta L^3}{\nu_m \kappa_m} \equiv Ra, \tag{4.1}$$

the Prandtl number

$$Pr_m = \nu_m/\kappa_m \equiv Pr, \tag{4.2}$$

and, as a response of the system, the Reynolds number of the resulting large-scale circulation (the “wind")

$$Re_m = \frac{UL}{\nu_m} \equiv Re. \tag{4.3}$$

Here U is the mean velocity of the large scale wind in the bulk of the fluid. We assume that there is only one such velocity scale, or, to be more precise, that the velocity of the wind is the same close to the top and close to

the bottom of the cell. The label m indicates that the material parameters are those at the mean temperature T_m. In the following we shall skip the label m of Ra, Pr, Re, and later also of the Nusselt number Nu. Whenever these nonlabelled dimensionless parameters are used, the respective material properties are meant as those at the mean temperature T_m of the external control temperatures. The actual time averaged temperature in the bulk is called T_c. It is different from T_m due to NOB effects, $T_c \neq T_m$.

The notation used in this chapter is shown in figure 4.1. The fluid properties such as ν, κ, and β carry the same index as the corresponding temperature at which they are considered, e.g., $\nu_t = \nu(T_t)$ for the kinematic viscosity at the top plate, and so on.

4.2.2 Temperature profile

Wu & Libchaber [3] have shown that for NOB thermal convection in cryogenic helium the temperature drop across the top BL Δ_t is smaller than the temperature drop across the bottom BL Δ_b. In contrast, for NOB thermal convection in glycerol Zhang *et al.* [4] showed that the opposite is the case, i.e., $\Delta_t > \Delta_b$. In general, the ratio of the temperature drops is described by the parameter[†]

$$\chi = \chi_\Delta = \Delta_b/\Delta_t. \tag{4.4}$$

Just as in large Ra Rayleigh-Bénard flow under OB conditions, we have no indication that for the time averaged profile there is a temperature drop across the bulk (center) of the RB cell, and therefore we assume that the total temperature difference between the cold top plate temperature T_t and the hot bottom plate temperature $T_b = T_t + \Delta$ consists only of the temperature drops across the thermal boundary layers,

$$\Delta = \Delta_t + \Delta_b\ . \tag{4.5}$$

The time averaged temperature in the center of the cell then is $T_c = T_t + \Delta_t = T_b - \Delta_b$. It deviates from T_m and expresses the response of the system to the NOB effects, while T_m is just the arithmetic mean of the external control parameters. Depending on the fluid, T_c may be larger or smaller than T_m.

Equations (4.4) and (4.5) can be solved for the temperature drops Δ_b and Δ_t across the bottom and top thermal BLs,

$$\Delta_b = \frac{\chi}{1+\chi}\Delta, \tag{4.6}$$

[†]Note that the parameter x of Wu & Libchaber [3] is $x = \chi^{-1}$.

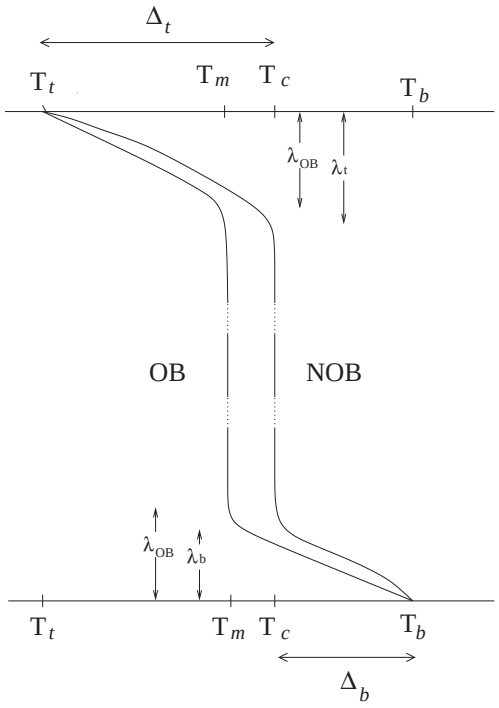

Figure 4.1: Sketch of temperature profile details: The time averaged temperature versus height z in the OB and NOB cases, respectively. The height of the cell is L. The temperature at the top plate $z = L$ is T_t and the one at the bottom plate $z = 0$ is T_b. The mean temperature is $T_m = (T_t + T_b)/2$. The thickness of the top thermal BL is λ_t, that of the bottom thermal BL is λ_b. The respective temperature drops are Δ_t and Δ_b. The time averaged temperature in the center is T_c. For water as the working fluid this center or bulk temperature T_c is larger than the mean temperature T_m. While $\lambda_{t,b}$ in the OB case are equal, under NOB conditions in the case of water the bottom BL is thinner as the top one, $\lambda_b < \lambda_t$. The z-dependence of Λ implies a (numerically small) curvature of the temperature profiles in the BLs. For $T_c > T_m$ the top BL width becomes larger and the bottom BL width smaller if OB is no longer valid. As will be discussed later, the sum of both widths at least for water seems to be the same as the corresponding sum under OB conditions. The relations between the slope-based BL thicknesses λ^{sl} and the profile based thicknesses $\lambda^{99\%}$ ("99% rule") will be shown to be $\lambda^{sl}_{t,b} < \lambda^{99\%}_{t,b}$, as is apparent from the graph, cf. also subsection 4.6.2, in particular Figure 4.15.

$$\Delta_t = \frac{1}{1+\chi}\Delta. \tag{4.7}$$

The temperature profile in the container is sketched in figure 4.1. In section 4.6 it will be *calculated* within an extended Prandtl-Blasius boundary layer theory.

4.2.3 Heat flux

The heat flux can be evaluated from the local heat-conservation equation

$$\rho c_p(\partial_t\theta + u_i\partial_i\theta) = \partial_i(\Lambda\partial_i\theta), \tag{4.8}$$

where θ is the temperature deviation from a convenient reference temperature, e.g. T_m. $\partial_i ...$ means $\partial .../\partial x_i$, $i = x, y, z$ are the three coordinates, and summation over repeated equal indices is assumed. By starting from Eq. (4.8) we have already assumed that the variation of the entropy per mass s with pressure p to a good approximation does not contribute, more precisely that $|\frac{dT}{dz}| \gg |\frac{T}{c_p}\left(\frac{\partial s}{\partial p}\right)_T \frac{dp}{dz}|$. Using $\frac{dp}{dz} = -\rho g$, the right hand side of this inequality can be rewritten as $\rho g(\partial T/\partial p)_s \equiv a_g$. Thus we assume that a_g, the adiabatic temperature change with pressure, is much smaller than the applied temperature gradient Δ/L [22–24]. Indeed, for our experiment with water described in Sect. 4.3 we typically have $a_g L/\Delta \approx 10^{-6}$ for this so called Schwarzschild parameter, i.e., it is negligibly small. Note that for gases close to the critical point the Schwarzschild correction in general cannot be neglected [13, 22, 23, 25, 26].

We area and time average $\langle ... \rangle_A$ equation (4.8). The label A indicates planes z =constant, parallel to the top and bottom plates of the container. In addition, we assume that plane averaged products of the type $\langle \rho c_p \partial_z(u_z\theta)\rangle_A$ or $\langle \Lambda\partial_z\theta\rangle_A$ can be approximated by their respective factorizations $\langle \rho c_p\rangle_A \langle \partial_z(u_z\theta)\rangle_A$ and $\langle\Lambda\rangle_A \partial_z \langle\theta\rangle_A$. We then obtain

$$\partial_z\left[\langle \rho c_p\rangle_A \langle u_z\theta\rangle_A - \Lambda(z)\partial_z\langle\theta\rangle_A\right] = \langle u_z\theta\rangle_A \partial_z\langle\rho c_p\rangle_A \approx 0. \tag{4.9}$$

In the second (approximate) equality, $\approx$, we have used the fact that for liquids the mass density ρ and the isobaric specific heat capacity c_p per mass to a good approximation are temperature and therefore height independent. For the case of water between 20°C and 60°C, on which we will focus, this is given with a precision of 1.6% and 0.07%, respectively, see table 4.1. Thus in the following we always consider ρ and c_p as being constant. All obtained results are considered as applicable to liquids, which share these properties ρ = constant and c_p = constant.

T	ρ	c_p	β	Λ	κ	ν	Pr
$T_t = 20.000$	0.99809	4.175	2.05	0.5975	0.1448	1.004	6.94
$T_{\bar{t}} = 30.911$	0.99532	4.169	3.14	0.6162	0.1494	0.794	5.31
$T_m = 40.000$	0.99220	4.169	3.88	0.6297	0.1528	0.669	4.38
$T_c = 41.822$	0.99150	4.169	4.02	0.6322	0.1534	0.648	4.23
$T_{\bar{b}} = 50.911$	0.98761	4.173	4.64	0.6434	0.1563	0.557	3.57
$T_b = 60.000$	0.98316	4.178	5.21	0.6529	0.1590	0.485	3.05

Table 4.1: Fluid parameters for the medium cell of height $L = 24.76\ cm$ in the local gravity field (Santa Barbara) $g = 979,1\ cm\ s^{-1}$, with the top temperature $T_t = 20.00^oC$ and the bottom temperature $T_b = 60.00^oC$. The units are as follows: $[T] = {}^oC$, $[\rho] = 10^3\ kg\ m^{-3}$, $[c_p] = 10^3 J\ kg^{-1}K^{-1}$, $[\beta] = 10^{-4}\ K$, $[\Lambda] = W\ m^{-1}K^{-1}$, $[\nu] = 10^{-6}m^2s^{-1}$, and $[\kappa] = 10^{-6}m^2s^{-1}$. The corresponding Rayleigh number is $Ra = 2.26 \cdot 10^{10}$ and the Prandtl number is $Pr = 4.38$, both based on the fluid parameters at the mean temperature $T_m = 40.00^oC$. This corresponds closely to the last data point for the medium cell in figure 4.9. The value $\chi = 0.833$ is obtained from the measured center temperature $T_c = 41.822^oC$. The mean temperatures $T_{\bar{t}}$ and $T_{\bar{b}}$ in the thermal top and bottom BLs are $T_{\bar{t}} = T_t + \Delta_t/2$ and $T_{\bar{b}} = T_b - \Delta_b/2$; the temperature drops follow from $\Delta_t = T_c - T_t$ and $\Delta_b = T_b - T_c$.

Eq. (4.9) then means that the expression in rectangular brackets is z-independent and therefore defines the conserved thermal current

$$\langle u_z\theta\rangle_A - \kappa(z)\partial_z\langle\theta\rangle_A \equiv J\,. \tag{4.10}$$

Here $\kappa(z) = \Lambda(z)/\rho c_p$ is the thermal diffusivity. J is z-independent and interpreted as the thermal flux, connected with the heat flux Q by $J = Q/\rho c_p$. Making the thermal flux J or the heat flux Q dimensionless, we obtain the Nusselt number

$$Nu_m = Nu \equiv \frac{Q}{\Lambda_m\Delta/L} = \frac{J}{\kappa_m\Delta/L} = \frac{L}{\kappa_m\Delta}\left[\langle u_z\theta\rangle_A - \kappa(z)\partial_z\langle\theta\rangle_A\right]\,. \tag{4.11}$$

Again, Nu without label m refers to the flux as being nondimensionalized with the material parameter κ_m taken at the mean temperature T_m of the control temperatures at the plates.

4.2.4 Thermal boundary-layer thicknesses

As under OB conditions the boundary layer thickness in the NOB case can be defined in two ways. A theoretically convenient definition is via the slope of the temperature profile at the plate. As the thickness λ^{sl} of the boundary layer we take that distance from the plate, where the tangent to the temperature profile at $z = 0$ (or correspondingly at $z = L$) reaches the center temperature T_c.

From eq. (4.11) we have $Q = -\Lambda(T(z = 0))\, \partial_z \langle\theta\rangle_A (0)$. For given heat current Q the slopes at the top and bottom are different, because the Λ's are different due to their temperature dependence. For $z > 0$ but in the immediate vicinity of the plates, where the convective contribution in (4.11) is still negligible, the slope $\partial_z \langle\theta\rangle_A$ already varies with z since $\Lambda(T(z))$ varies. Thus there is a curvature in the NOB profile which is absent in the OB case where Λ is height (z) independent.

Going e.g. from the bottom plate $z = 0$ into the interior of the RB cell, $\Lambda(z)$ decreases according to the material properties of water, given in Table 4.1. Therefore the slope $\partial_z \langle\theta\rangle_A$ increases and $\partial z/\partial \langle\theta\rangle$ as its inverse decreases. The profile thus first bends downwards (more parallel to the plate surface) before near the bulk range it more or less sharply bends upwards to merge into the constant center temperature T_c. This characterictic additional curvature of the profile, which *increases* the angle under which the temperature profile hits the bottom plate surface, is a signature of NOB conditions in the thermal boundary layer. In comparison to the OB case the slope $\partial \langle\theta\rangle / \partial(-z) = Q/\Lambda$ is smaller in the NOB case, since Λ is larger at the bottom temperature T_b. In contrast, at the cooler top plate the slope becomes larger under NOB conditions because of the smaller Λ, and thus the angle to the plate surface here decreases. This breaks the symmetry of the temperature profile in the z-direction about the horizontal midplane of the cell. In figure 4.1 we have sketched the BL temperature profiles for the OB and NOB cases. (Near onset of convection this broken midplane symmetry is one of the important factors for pattern formation under NOB conditions, which is different from the OB case, cf. [14].) These findings about the temperature profile changes are still open for experimental verification.

Now, by definition, the flux conservation equation (4.11) for the heat flux Q or thermal flux J implies a relation between the ratios of these BL thicknesses $\lambda_b^{sl}, \lambda_t^{sl}$ and the corresponding temperature drops Δ_b, Δ_t. Namely, applying equation (4.10) or (4.11) at the two plates $z = 0$ and

$z = L$ gives

$$\kappa_t \frac{\Delta_t}{\lambda_t^{sl}} = \kappa_b \frac{\Delta_b}{\lambda_b^{sl}} = J = Nu \frac{\kappa_m \Delta}{L}. \tag{4.12}$$

In analogy to the ratio χ of the temperature drops (cf. eq. (4.4)) we also introduce the ratio of the slope BL thicknesses

$$\chi_{\lambda^{sl}} = \frac{\lambda_b^{sl}}{\lambda_t^{sl}} = \frac{\kappa_b}{\kappa_t} \frac{\Delta_b}{\Delta_t} = \frac{\kappa_b}{\kappa_t} \chi = \chi_\kappa \chi, \tag{4.13}$$

which is another measure characterizing NOB effects. Here χ_κ is the ratio

$$\chi_\kappa = \kappa_b / \kappa_t \,, \tag{4.14}$$

and χ_ν, χ_β, etc. are similarly defined.

For the thicknesses of the BLs themselves one has from eqs. (4.12) and (4.6),(4.7)

$$\frac{\lambda_b^{sl}}{L} = \frac{\Delta_b}{\Delta} \frac{\kappa_b}{\kappa_m} \frac{1}{Nu} = \frac{\chi}{1+\chi} \frac{\kappa_b}{\kappa_m} \frac{1}{Nu}, \tag{4.15}$$

$$\frac{\lambda_t^{sl}}{L} = \frac{\Delta_t}{\Delta} \frac{\kappa_t}{\kappa_m} \frac{1}{Nu} = \frac{1}{1+\chi} \frac{\kappa_t}{\kappa_m} \frac{1}{Nu}. \tag{4.16}$$

By adding these two equations one easily obtains for the Nusselt number

$$Nu = \frac{L}{\lambda_t^{sl} + \lambda_b^{sl}} \frac{\kappa_t \Delta_t + \kappa_b \Delta_b}{\kappa_m \Delta}. \tag{4.17}$$

Another way to define the thermal BL thickness takes the full temperature profile of the BL into account. It defines the thermal BL thickness $\lambda^{99\%}$ as the distance from, say, the bottom plate to the position at which the temperature T is given by $T = T_b - 0.99\Delta_b$. This definition is in analogy to the definition of the thickness δ of the kinetic BL, as the distance distance from the plate where, say, 99% of the bulk velocity is achieved.

In the OB case this profile-based thickness δ of the kinetic BL follows from the classical Prandtl-Blasius theory [27, 28],

$$\delta = a L / Re^{1/2} \,. \tag{4.18}$$

In [29] we have determined the prefactor a for the case of flow in RB cells from the experimental results of ref. [30], leading to $a = 0.483$. (This

value differs, of course, from the Blasius factor, valid for flow along infinite plates.) Under OB conditions the profile-based thermal boundary-layer thickness $\lambda^{99\%}$ can be calculated according to the Prandtl-Blasius BL theory (cf. [31, 32]. It is (cf. also [33])

$$\frac{\lambda^{99\%}}{L} = \frac{a' C(Pr)}{Re^{1/2} Pr^{1/3}}, \tag{4.19}$$

with a function $C(Pr)$ given by Meksyn [31]. For large Pr numbers one has $C(Pr) \to 1$, whereas for small Pr one finds $C(Pr) \propto Pr^{-1/6}$. The prefactor a' in principle can be different from the prefactor a of eq. (4.18).

While $\lambda^{99\%}/\delta \propto C(Pr)/Pr^{1/3}$ depends on Pr only, the corresponding ratio $\lambda^{sl}/\delta \propto \sqrt{Re}/Nu$ depends on both Pr *and* Ra in general. From the above profile discussion we expect $\lambda^{99\%} > \lambda^{sl}$. In section 4.6 this expectation will be shown to be correct.

Apparently the flow in the BLs of large-Ra convection will be time dependent. There are lots of BL separations and plume formations. Thus also the terms $\partial_t \theta$ in the heat conservation equation (4.8) and $\partial_t u_i$ in the Navier-Stokes equation for momentum conservation

$$\partial_t u_i + u_j \partial_j u_i = -\frac{1}{\rho} \partial_i P + \partial_j (\nu \partial_j u_i) \tag{4.20}$$

will contribute. The flow is no longer laminar time independent. But apparently the overwhelming amount of RB data is consistent with the assumption that still the characteristic Prandtl scaling of the wall normal quantities holds, $z \propto L/\sqrt{Re}$ and $u_z \propto U/\sqrt{Re}$. The boundary layer flow is not yet fluctuation dominated as it is in fully developed turbulence, where the profile is expected to be adequately described by a logarithmic profile.

The formulas (4.4), (4.5), (4.6), and (4.7) represent our description of the basic features of the temperature profile. Equations (4.8), (4.9), (4.10), and (4.11) are consequences of the local conservation of heat. Equations (4.12) and (4.15),(4.16) contain additional physics, namely the definition of the BL thicknesses λ_b^{sl} and λ_t^{sl}. They reflect the fact that the heat transport into the liquid at the entrance $z = 0$ and out of the liquid at the exit $z = L$ is purely molecular and convection does not yet contribute. Note that the profile thicknesses $\lambda_{b,t}^{99\%}$ instead contain the influence of convection, represented by $\langle u_z \theta \rangle_A$.

4.3 Experimental results

4.3.1 Experimental setup

The experiments were done using three cylindrical cells filled with water. In each cell we made measurements of the quantities characterizing NOB effects at constant mean temperature T_m and thus constant mean Pr. In each case the aspect ratio $\Gamma \equiv D/L$ was close to one. The cells had heights $L = 50.62,\ 24.76$, and $9.52\ cm$, and diameters $D = 49.70, 24.81$, and $9.21\ cm$, corresponding to $\Gamma = 0.982$, 1.002, and 0.967. We will refer to them as the large, medium, and small cell, respectively. For most of the measurements the mean temperature was $T_m = 40.00°C$ where $Pr = 4.38$; for some it was 29°C where $Pr = 5.55$. We varied Ra by varying Δ at fixed T_m thus keeping all other parameters in the definition (4.1) of Ra fixed. Therefore Ra here means $Ra = \Delta/\Delta_{m,i}$, with $\Delta_{m,i} = \nu_m \kappa_m/\beta_m g L_i^3$ where the label i means "large", "medium", or "small" cell. Time-averaged values of the top-plate temperature T_t, the bottom-plate temperature T_b, and the heat current Q were obtained at each Ra. For the medium and large cell we also determined T_c by measuring the side-wall temperature at half-height using 8 thermometers at uniformly distributed azimuthal locations. All measurements were averaged over time periods ranging from slightly less than a day to several days. For each Ra value the side-wall temperatures were averaged over the eight locations. Since there is virtually no heat flow laterally through the wall, we expect the side-wall temperature to be equal to the temperature of the fluid adjacent to it. Because of the large-scale circulation (LSC), the fluid temperature varies along a diameter of the horizontal mid-plane, being higher where the fluid rises and lower where it falls. Qiu & Tong [34] made temperature measurements for a slightly tilted cell with $\Gamma = 1.07$ and $L = 20.3\ cm$ in which the LSC had a preferred angular orientation determined by the tilt direction. Along a diameter oriented to coincide with the tilt direction they showed that the temperature variation is linear. For a Rayleigh number of 3.3×10^9 ($\Delta = 16$ K) they found it to be $\delta T \simeq 0.12$ K across the radius, giving $\delta T/\Delta \simeq 0.0075$. Because of the linear variation of T along the diameter, we expected the average of the temperatures given at two opposite locations to be equal to the center temperature T_c to better than 0.1% of Δ. Since we averaged the readings of eight thermometers uniformly distributed around the azimuth, we believe that our side-wall temperature-readings give an accurate determination of T_c. We note that such a determination can not be done accurately with a single thermometer, as was

attempted by Chilla *et al.* [35]. For details regarding the experimental apparatus and procedures, see [36].

4.3.2 Temperature measurements

The ratios $\chi_\kappa, \chi_\nu, \chi_\beta, \ldots$ (see e.g. equation (4.14)) characterize the strength of the NOB effects in terms of the material properties. For the Δ range covered in the medium and small cell, these effects can be considerable, as seen from Fig. 4.2. In particular, this holds for the kinematic viscosity, which at the top wall is more than twice as large than at the bottom wall, and for the thermal expansion coefficient β, which at the top wall is less than 1/2 of its value at the bottom wall. The effect on χ_κ and χ_Λ is up to 8%, whereas it is negligibly small for the density ρ and the specific heat capacity c_p. Figure 4.3 displays the *relative* deviations $2(X_b - X_t)/(X_b + X_t)$ of the various material properties. A similar analysis of the properties of the helium gas used for Nusselt-number measurements in cryogenic experiments was carried out by Niemela & Sreenivasan [12] (see their Fig. 6). In the helium case the major contribution to NOB effects comes from c_p and β; unlike for water, the viscosity plays only a minor role.

In Fig. 4.4 we show the temperature differences $\Delta_b = T_b - T_c$ (circles) and $\Delta_t = T_c - T_t$ (squares) for $Pr = 4.38$. The open (solid) symbols are for the medium (large) cell. The increasing difference between Δ_b and Δ_t with increasing Δ reflects the growing deviation from the Oberbeck-Boussinesq approximation; for OB conditions one would have $\Delta_b = \Delta_t = \Delta/2$. In Fig. 4.5 we show half this difference, equal to $T_c - T_m$, as a function of Δ for $Pr = 4.38$ as well as for $Pr = 5.55$. Figure 4.6 gives the experimental results for $\chi = (T_b - T_c)/(T_c - T_t) = \Delta_b/\Delta_t$ for the large (solid symbols) and medium (open symbols) cell for $Pr = 4.38$ (circles) and for $Pr = 5.55$ (squares). In Fig. 4.7 we replot χ as a function of Ra for the medium cell and $Pr = 4.38$. In Figs. 4.5 and 4.6 equations for polynomial fits to the data are given in the caption. In section 4.5 we will compare our experimental results for χ with the prediction of Wu & Libchaber [3], based on the assumption of equal temperature scales at the bottom and the top boundary layers. As can be seen already from Fig. 4.6, this prediction does not agree very well with our data.

4.3.3 NOB effects on Nu and Re

We now come to the NOB effects on the Nusselt number Nu and on the Reynolds number Re. For each L the data covered about 1.5 decades of Ra.

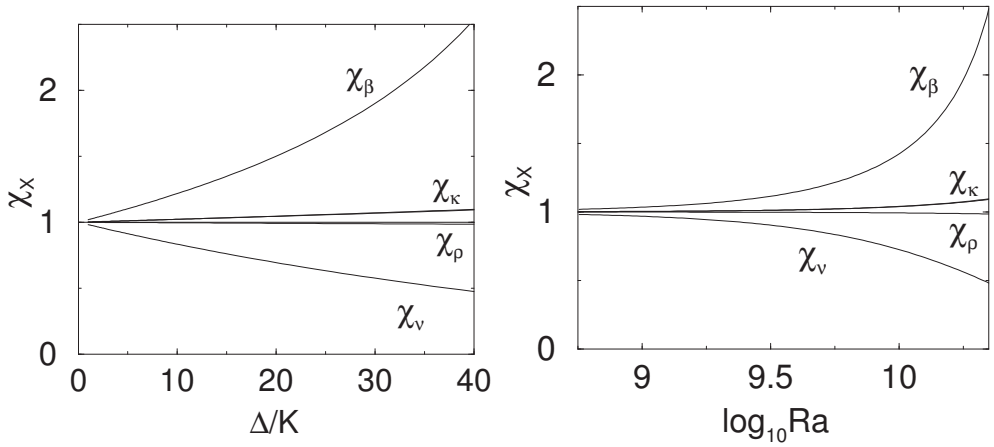

Figure 4.2: The ratios χ_X of the material parameters for $T_m = 40°C$ at the bottom and top walls as functions of Δ (left), or as functions of $Ra = \Delta/\Delta_{m,medium}$ (right) for the medium cell. It is $\Delta_{m,medium} = 1.772 \times 10^{-9}K$. The symbol X stands for β, κ, ρ, or ν. χ_Λ is indistinguishable from χ_κ, and both χ_ρ and χ_{c_p} are basically equal to 1. Deviations from $\chi_X = 1$ signal NOB effects. The ratio can be larger than 2 (smaller than 1/2) for χ_β (χ_ν). Evident consequences are significant differences of the buoyancy force, of the viscous drag, and thus of the BL thickness near the bottom as compared with the top region. A nonlinear dependence of the various χ_X's on Δ seems apparent.

However, since $Ra \propto L^3\Delta$, the Ra-range of each cell was shifted relative to the next larger or smaller one by about a decade. The measurements at the largest Ra of a smaller cell, which might be expected to show departures of Nu and Re from the OB approximation, overlapped with results at the smallest Ra of a larger cell which in turn would be expected to conform well to the OB approximation. Thus a comparison between any two cells in the overlapping range of Ra can be expected to reveal NOB effects.

The Reynolds number Re of the large-scale circulation, deduced from plume transit times, was measured via temperature auto- and cross-correlations, as detailed by Brown *et al.* [37]. The velocity U, on which Re is based via eq. (4.3), was measured as a distance, proportional to the cell height L, divided by the turnover time of the plumes. In the OB case Re is found to scale like $Ra^{0.46}$ up to $Ra \simeq 2 \cdot 10^9$, and beyond that critical Rayleigh number like $Ra^{1/2}$. Here we focus only on possible NOB effects on Re. For that we show in figure 4.8 the experimental results for $Re/Ra^{1/2}$

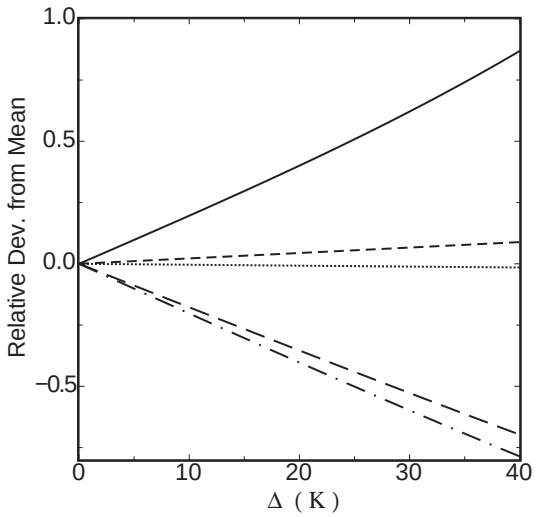

Figure 4.3: The relative deviation $2(X_b - X_t)/(X_b + X_t)$ of a property X from its mean value $(X_b + X_t)/2$ as a function of the temperature difference Δ for a mean temperature $T_m = 40°C$. Solid line: expansion coefficient β. Short dashed line: heat conductivity λ and thermal diffusivity κ. Dotted line: density ρ. Long dashed line: kinematic viscosity ν. Dash-dotted line: Prandtl number Pr.

vs Ra. The solid squares (medium cell) near $Ra = 2.1 \cdot 10^{10}$ are for $\Delta =$ 38K and should show NOB effects, whereas those for the large cell (open symbols) at the same Ra are for $\Delta \approx 4.4$K, clearly in the OB range. For each of the two cells, the extent of departures of T_c from the OB approximation T_m is illustrated in the lower figure by the temperature ratio

$$\chi = \frac{\Delta_b}{\Delta_t} = \frac{\Delta/2 - (T_c - T_m)}{\Delta/2 + (T_c - T_m)}.$$

As the two sets of data for Re agree within the experimental precision (about 2%), it can be concluded that NOB effects on Re for $\chi \simeq 0.84$ are at most a percent or two.

The Nu data for the large and medium cells were corrected for the effect of the finite conductivity of the copper top and bottom plates [36, 38–40] on the heat transport in the fluid (no correction was needed for the small cell). The influence of the finite wall conductivity [10, 12, 41, 42] was negligible, except for the small cell where a correction of order one

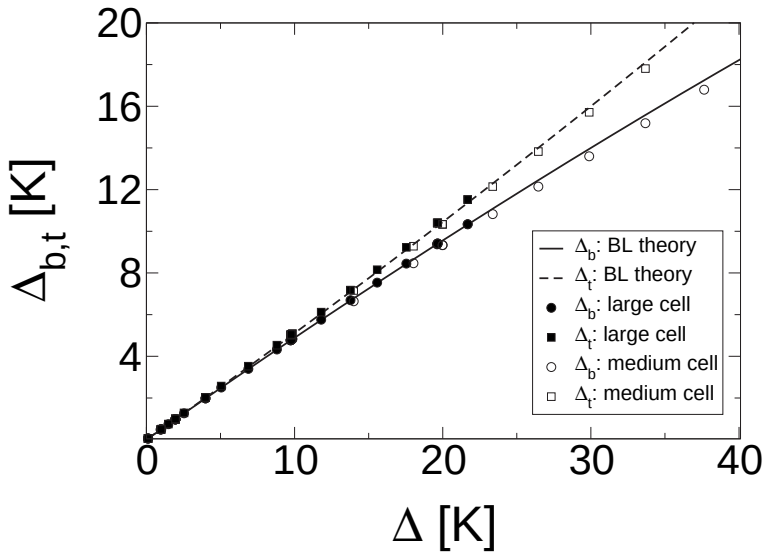

Figure 4.4: The measured temperature differences $\Delta_b = T_b - T_c$ (circles) across the bottom and $\Delta_t = T_c - T_t$ (squares) across the top BL for $T_m = 40°C$ ($Pr = 4.38$) as a function of the total applied temperature difference Δ. Solid symbols: large cell. Open symbols: medium cell. The solid and the dashed lines originate from our theory presented in section 4.6.

percent was applied. These experiments are described in detail by Brown *et al.* [36]. Data for $Nu(Ra)$ under strictly Boussinesq conditions were reported by Funfschilling *et al.* [43]. Here we concentrate on the results relevant to deviations from the OB approximation.

One may wonder whether the weak deviation of the aspect ratio from 1 ($\Gamma = 0.982, 1.002, 0.967$ for the large, medium, and small cell, respectively) may affect our results on the Nusselt number, as Shraiman & Siggia [44] had suggested a relatively strong aspect ratio dependence $Nu \sim \Gamma^{-3/7}$. However, note that the actual dependence is much weaker as demonstrated experimentally by the work of Funfschilling *et al.* [43]. There it is shown for instance that the $\Gamma = 6$ results for Nu are only about 4% below the $\Gamma = 1$ results. The extremely small Γ dependence was confirmed more recently also by Sun *et al.* [45]. It can not influence the present data over the range $0.967 \leqslant \Gamma \leqslant 1.002$ by a measurable amount. Note also that the experimental analysis of the Γ-dependence also included many Γ-values close to $\Gamma = 1$, where one would only expect a deformation of the

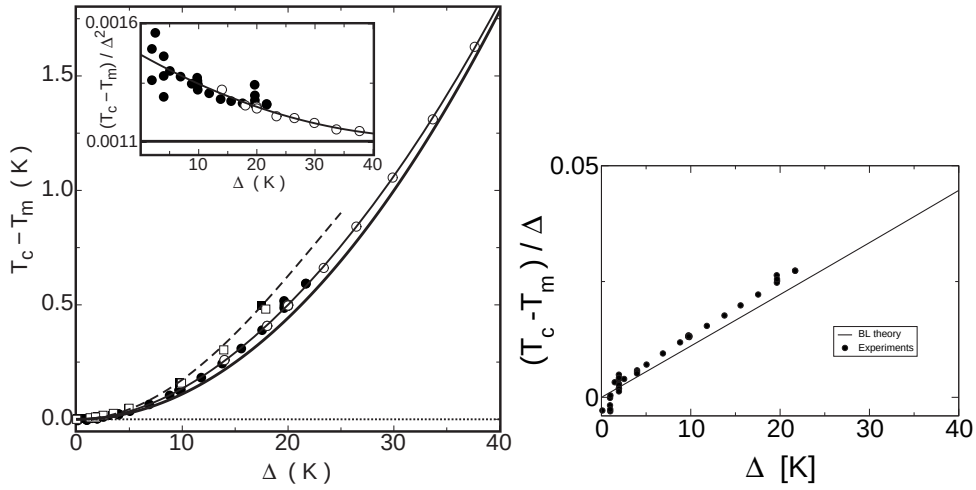

Figure 4.5: (a) The difference between the measured temperature T_c at half-height and the mean (control) temperature $T_m = (T_b + T_t)/2$. Solid symbols: large cell. Open symbols: medium cell. Circles: $T_m = 40°C$ and $Pr = 4.38$. Squares: $T_m = 29°C$ and $Pr = 5.55$. The solid (dashed) line corresponds to the polynomial fit $T_c - T_m = c_2\Delta^2 + c_3\Delta^3 + c_4\Delta^4$ to the large (medium) cell data with $c_2 = 1.47 \times 10^{-3}K^{-1}$ ($c_2 = 1.81 \times 10^{-3}K^{-1}$), $c_3 = -1.37 \times 10^{-5}K^{-2}$ ($c_3 = -1.81 \times 10^{-5}K^{-2}$), $c_4 = 1.35 \times 10^{-7}K^{-3}$ ($c_4 = 0$). The fat line results from our theory of section 4.6, applied to the large cell. Its polynomial representation yielded $c_2 = 1.105 \times 10^{-3}K^{-1}$, $c_3 = 1.09 \times 10^{-8}K^{-2}$, and $c_4 = 5.79 \times 10^{-9}K^{-3}$. Although c_3 and c_4 are much smaller than the experimental values, the overall curve is in quite good agreement with the data. The center temperature T_c deviates from T_m by 1.822K for $\Delta = 40K$, i.e., by less then 5%. Thus the comparison between theory and experiment is easier if one plots the quantity $(T_c - T_m)/\Delta^2$, in K^{-1}, vs. Δ, as done in the inset (again the solid and the fat line are the fits to the data and the theory respectively). Figure (b) displays the dimensionless quantity $(T_c - T_m)/\Delta$ vs. Δ for the large cell only.

large scale convection roll, but no extra roll: E.g., Funfschilling *et al.* [40] analysed $\Gamma = 0.98$, 0.67, 0.43, and 0.275, Funfschilling *et al.* [43] analysed $\Gamma = 0.967$, 0.982, 1.003, 1.506, 2.006, 3.010, and 6.020, and Sun *et al.* [45] analysed $\Gamma = 0.67$, 1.0, 2.0, 5.0, 10, and 20, all only finding minute dependences. However, we have corrected for tiny systematic errors in the data as discussed already in ref. [43] (due primarily to errors in the geometry) which can be different for different cells (by a fraction of a percent) by

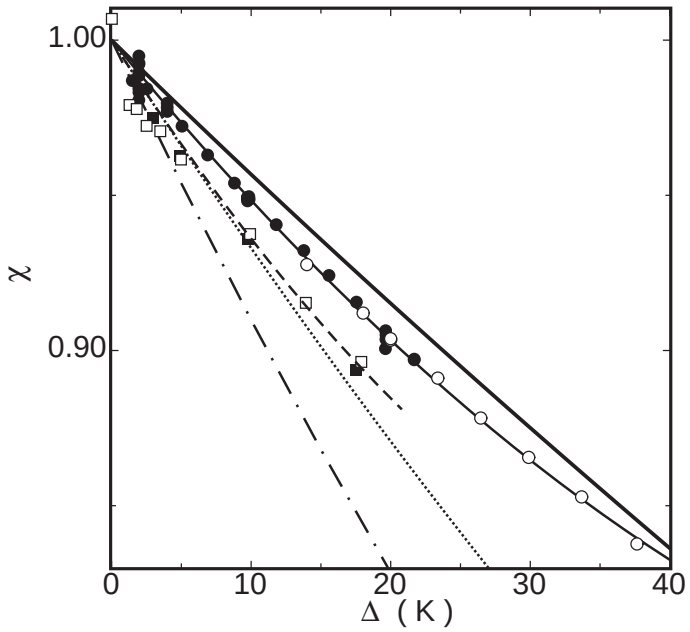

Figure 4.6: Experimental results for the ratio $\chi = (T_b - T_c)/(T_c - T_t) = \Delta_b/\Delta_t$ for the large cell (solid symbols) and medium cell (open symbols). Circles: $T_m = 40.00°C$ and $Pr = 4.38$. Squares: $T_m = 29.00°C$ and $Pr = 5.55$. The solid (dashed) line is a polynomial fit to the data that yielded $\chi = 1 + a_{\chi,1}\Delta + a_{\chi,2}\Delta^2$ with $a_{\chi,1} = -5.48 \times 10^{-3}K^{-1}$ and $a_{\chi,2} = 3.25 \times 10^{-5}K^{-2}$ ($a_{\chi,1} = -7 \times 10^{-3}K^{-1}$ and $a_{\chi,2} = 6 \times 10^{-5}K^{-2}$). The dotted and dash-dotted lines are the results computed for $T_m = 40.00$ and $29.00°C$ respectively from Eq. (4.31) as suggested by Wu & Libchaber [3]. They can be represented by $\chi_{WL} = 1 - 0.00694\Delta + 2.38 \times 10^{-5}\Delta^2$ and $\chi_{WL} = 1 - 0.00945\Delta + 4.35 \times 10^{-5}\Delta^2$, respectively. In our data the linear terms seem dominant, but the nonlinear deviations are clearly visible. For $\Delta = 40K$ the contributions are -0.219 from the linear term and $+0.052$ from the quadratic term. The fat line results from our theory of section 4.6, applied to the large cell. It is in reasonable agreement with the data.

overlapping the Nusselt numbers (through tiny shifts) of the small and the medium cell and then of the medium and the large cell in their respective OB regimes.

In Fig. 4.9a we show the results for Nu in the reduced form of $Nu/Ra^{1/3}$ as a function of Ra (on a logarithmic scale). For the small and medium

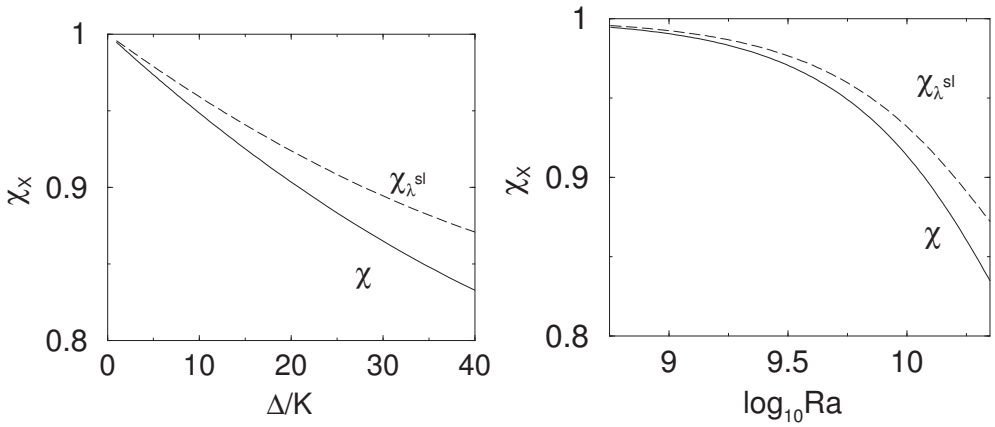

Figure 4.7: The ratios $\chi = \chi_\Delta$ (solid) and $\chi_{\lambda^{sl}}$ (dashed) at $T_m = 40°C$ and $Pr = 4.38$ as functions of Δ (left), and as functions of $Ra = \Delta/\Delta_{m,medium}$ for the medium cell (right), with $\Delta_{m,medium} = \nu_m\kappa_m/(\beta_m g L^3_{medium}) = 1.772 \times 10^{-9}$K. Deviations from $\chi_X = 1$ signal NOB effects.

cell, one sees that Nu in the NOB region is slightly smaller, but only by a percent or so, than the data in the strictly Boussinesq range.

In order to show the NOB effect more clearly, we fitted the strictly Oberbeck-Boussinesq data [43] to the empirical function

$$Nu/Ra^{0.3} = \sum_{i=0}^{4} b_i[\log_{10}(Ra)]^i \tag{4.21}$$

and obtained the coefficients $b_0 = -1.7934$,$b_1 = 0.85734$,$b_2 = -0.13992$, $b_3 = 0.009902$, $b_4 = 0.0002490$. The function fits the data within their scatter, but should not be relied upon for Ra values outside the range $10^8 < Ra < 10^{11}$ used in the fit. Relative deviations from the function are shown in Fig. 4.9b. There the deviations from the OB approximation become more clear. In figure 4.10 the same data for Nu_{NOB}/Nu_{OB} are given as a function of Δ.

Comparison with Figs. 4.6 and 4.7 shows that NOB effects on Nu are negligible in the range where $\chi \gtrsim 0.94$ but detectable in the experiment for smaller values of χ, i.e., for larger NOB deviations from $\chi = 1$. But even when χ reaches its smallest experimental value near 0.83, the data fall less than only 1.5 percent below the Boussinesq results. Even though the NOB effects on Nu are quite small, it is interesting to note that they *diminish* the heat transport.

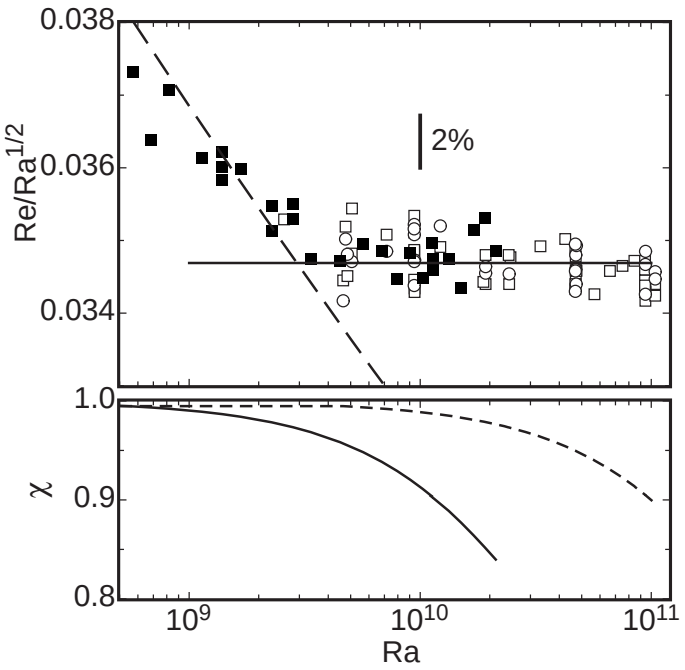

Figure 4.8: Upper figure: $Re/Ra^{1/2}$ vs Ra as measured for the medium cell (solid symbols) and the large cell (open symbols). (The dashed and solid lines indicate the change of the Ra-dependence of Re which is not discussed here.) Lower figure: $\chi = \Delta_b/\Delta_t$ as a function of Ra for the medium (solid line) and large (dashed line) cell. The square-symbols originate from the cross-correlations, the circle-symbols from auto-correlations of temperatures. The solid squares (medium cell) at the highest Ra ($Ra = 2.1 \cdot 10^{10}$) are for $\Delta = 38$K, have $\chi \simeq 0.84$, and should show NOB effects, whereas those for the large cell at the same Ra (open symbols), which are for $\Delta \approx 4.4$K, have $\chi \simeq 0.98$, , and are clearly in the OB range. As the two data sets agree within the experimental precision (2%), it can be concluded that NOB effects on Re are at most of that order of magnitude for χ near 0.84.

Measurements of χ and of Nu under NOB conditions were made previously by Wu & Libchaber [3] using ^{4}He gas at low temperatures near its critical point. For small Ra, where their cells conformed to the Oberbeck-Boussinesq approximation, they found $\chi \simeq 1.1$. It is not known why their results in this OB limit differed systematically from unity. At large Ra,

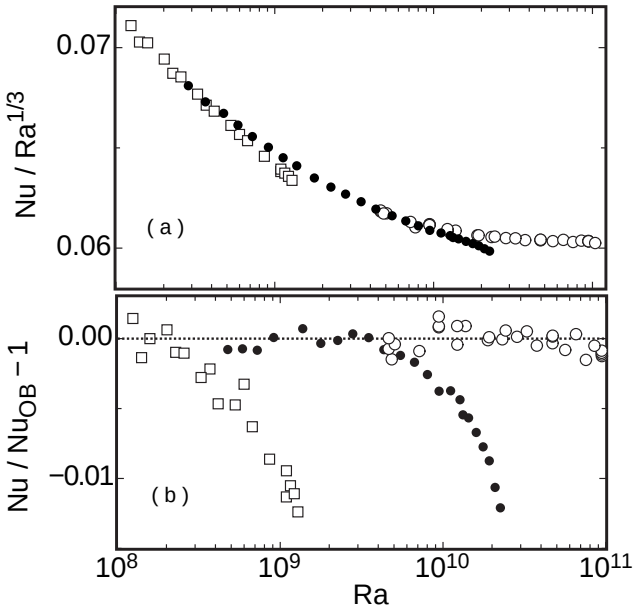

Figure 4.9: (a) The reduced Nusselt number $\mathrm{Nu}/\mathrm{Ra}^{1/3}$ on a linear scale as a function of the Rayleigh number Ra on a logarithmic scale for the small (open squares), medium (solid circles), and large (open circles) cell for $\mathrm{T_m} = 40°\mathrm{C}$ ($\mathrm{Pr} = 4.38$). For the small (medium) cell deviations from the Oberbeck-Boussinesq approximation are seen at the largest Ra and yield Nusselt numbers that are smaller than the more nearly Oberbeck-Boussinesq results obtained from the medium (large) cell. (b) The relative deviations of Nu from Eq. 4.21 as a function of Ra. This equation provides a good fit to the data taken under OB conditions in the Ra-range considered here. In Fig. 4.10 the same data for $\mathrm{Nu_{NOB}}/\mathrm{Nu_{OB}}$ are given as a function of Δ.

however, their results for χ became as large as 2.5, indicating strong NOB effects. They did not have two cells of different sizes, and thus of different departures from the OB approximation at the same Ra, for comparison. However, when their data were plotted on a log-log scale, the results at large Ra fell significantly below a straight line drawn through the results at smaller Ra. Assuming that a power-law should have fit the OB data, one

then can conclude that also in this case Nu decreased due to NOB effects.

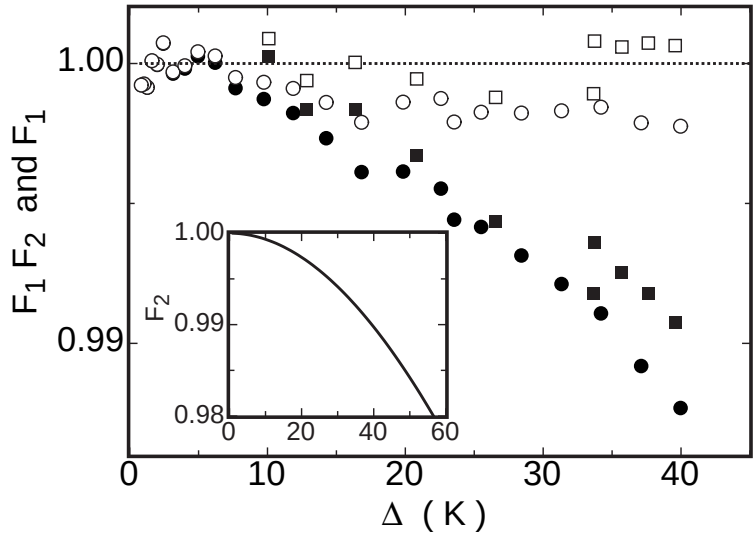

Figure 4.10: $F_1 \cdot F_2 = Nu_{NOB}/Nu_{OB}$ and F_1 (defined by equation (4.23) but calculated via eq. (4.25), second equality sign) as functions of Δ. Solid circles: $F_1 \cdot F_2$ for the medium cell. Open circles: F_1 for the medium cell. Solid squares: $F_1 \cdot F_2$ for the small cell. Open squares: F_1 for the small cell. While the product $F_1 \cdot F_2$ is the measured ratio of the heat currents Q in the NOB case and that in the OB case, the individual factors F_1 and F_2 contain the material properties, in particular F_2 depends on $\kappa(T)$ together with χ according to eq.(4.24). The inset shows the parameter $F_2 = (\kappa_t\Delta_t + \kappa_b\Delta_b)/(\kappa_m\Delta)$ as a function of Δ for $T_m = 40°C$. The input is the material parameter $\kappa(T)$ and the measured ratio $\chi = \Delta_b/\Delta_t$. The equation $F_2 = 1 + d_2\Delta^2 + d_3\Delta^3$ with $d_2 = -6.81 \times 10^{-6}K^{-2}$ and $d_3 = 0.98 \times 10^{-8}K^{-3}$ yielded a good fit to the data.

4.4 Towards understanding the NOB robustness of Nu

Can one understand the insensitivity of Nu to the NOB conditions, which so strongly contrasts with the sensitivity of the ratios χ_ν, χ_β for the material properties, or for the ratio $\chi = \Delta_b/\Delta_t$? The center temperature T_c

deviates from the mean temperature T_m by about 5% of Δ at $\Delta = 40$K, i.e., also is rather insensitive. A step towards an understanding is to divide the Nusselt number Nu in the form eq. (4.17) by its OB value $Nu_{OB} = L/(2\lambda^{sl}_{OB})$. This gives

$$\frac{Nu_{NOB}}{Nu_{OB}} = \frac{2\lambda^{sl}_{OB}}{\lambda^{sl}_t + \lambda^{sl}_b} \frac{\kappa_t\Delta_t + \kappa_b\Delta_b}{\kappa_m\Delta}. \tag{4.22}$$

(For clarity in this section we denote the measured Nusselt number Nu as Nu_{NOB}.) This ratio consists of two factors. In the first one

$$F_1 = \frac{2\lambda^{sl}_{OB}}{\lambda^{sl}_t + \lambda^{sl}_b}, \tag{4.23}$$

describing the contributions of the top and bottom thermal BL thicknesses, only the sum of the respective BL thicknesses in the OB and the NOB cases appears. Similarly, also in the second factor

$$F_2 = \frac{\kappa_t\Delta_t + \kappa_b\Delta_b}{\kappa_m\Delta} \tag{4.24}$$

the corresponding sums $\kappa_t\Delta_t + \kappa_b\Delta_b$ and $\kappa_m(\frac{\Delta}{2} + \frac{\Delta}{2})$ appear. In both factors F_1 and F_2 the NOB effects will increase one term and decrease the other term in the respective sums. If the material parameters depended on temperature only linearly, then there would be a (partial) cancellation of the NOB effects in the two terms, leading to only small NOB, order Δ^2, corrections. This point will be made quantitative in subsection 4.6.4. Thus NOB corrections of Nu depend on the nonlinear, at least quadratic contributions to the NOB deviations of the material parameters, in contrast to those of χ or $(T_c - T_m)/\Delta$, χ_ν, and χ_β, which have already linear contributions. From figure 4.2, left, and figure 4.3 we conclude that at least for not too large Δ the Δ-dependence of the material properties indeed is basically linear, and we therefore start to understand the robustness of Nu towards NOB corrections: Linear NOB contributions cancel in Nu.

Let us focus on the Δ-dependence of the factors F_1 and F_2 in eq. (4.22) in more detail. From the thermal diffusivity $\kappa(T)$ and the experimental results for Δ_t and Δ_b we obtain $F_2(\Delta)$, see the inset of Fig. 4.10. As was the case for $T_c - T_m$, the factor F_2 can be well represented by the quadratic equation $F_2 - 1 = d_2\Delta^2$, without any linear term (plus of course higher powers of Δ). A least-squares fit to the data yielded $d_2 = -6.81 \times 10^{-6}\mathrm{K}^{-2}$.

We will theoretically understand this quadratic dependence in subsection 4.6.4.

With this F_2 and using the experimental results for Nu_{NOB}/Nu_{OB} from figure 4.10 we can calculate

$$F_1 = \frac{2\lambda_{OB}^{sl}}{(\lambda_t^{sl} + \lambda_b^{sl})} = \frac{Nu_{NOB}/Nu_{OB}}{F_2} = \frac{Q/Q_{OB}}{F_2}\,, \tag{4.25}$$

the ratio of the total thermal BL thicknesses. F_1 is displayed as open symbols in fig. 4.10. We see that within an experimental uncertainty of 0.2% the BL thickness ratio F_1 is independent of Δ, namely $F_1 \approx 1$. The experimental data thus suggest that $\lambda_t^{sl} + \lambda_b^{sl} \cong 2\lambda_{OB}^{sl}$ even under strong NOB conditions, where $\lambda_t^{sl}/\lambda_b^{sl}$ differs considerably from unity. Because of our finding for thermal convection in water, that the sum of the thermal slope BL thicknesses is conserved within experimental precision,

$$\lambda_t^{sl} + \lambda_b^{sl} \cong 2\lambda_{OB}^{sl}\,, \tag{4.26}$$

the NOB corrections on Nu are only governed by F_2, and thus are quadratic in Δ to an extremely good approximation. The finding $F_2 < 1$ would then moreover explain the observed *reduction* of Nu_{NOB} as compared to Nu_{OB}.

Fig. 4.10 also shows $Nu_{NOB}/Nu_{OB} = F_1 \times F_2$ for the medium and small cell as solid circles and open squares, respectively. One sees that within 0.1% or so the data collapse onto a single curve.

We may speculate on the meaning of these results and cautiously draw some very preliminary conclusions. Consider the hypothetical case that κ (and Λ) does not depend on T i.e., $\kappa_b = \kappa_t = \kappa_m$, while ν, β vary strongly. Then $F_2 = 1$ for any distribution of the temperature drops between top and bottom BL. Since for constant κ there is no additional curvature, the temperature profile will not lose its linear form in the BLs under NOB effects. Nevertheless, λ_b^{sl} can still be different from λ_t^{sl}, resulting in $T_c \neq T_m$. As long as the sum of the new BL thicknesses will be the same as it was before, i.e., under OB conditions, F_1 is equal to $F_1 = 1$. This immediately gives $Q_{NOB} = Q_{OB}$ or $Nu_{NOB} = Nu_{OB}$, i.e., the heat flow will not change despite $T_c \neq T_m$. The shift of the bulk temperature from T_m to T_c is the sole effect of the strong variations of ν and β, but Nu needs not see this if κ is T-independent.

If, however, κ depends on T, there is additional profile curvature which will lead to a change of the heat flow Q. It seems as if F_2 takes care of that while still $F_1 \cong 1$. Then the non Oberbeck-Boussinesq heat current Q

can be calculated solely from the material properties and the temperature drops Δ_b and Δ_t,

$$\frac{Q_{NOB}}{Q_{OB}} = \frac{Nu_{NOB}}{Nu_{OB}} \cong \frac{\kappa_b \Delta_b + \kappa_t \Delta_t}{\kappa_m \Delta} \,. \tag{4.27}$$

This guarantees the robustness against NOB effects, because the linear term in the numerator is $\kappa_m\Delta$ and the cubic terms lead to corrections of order Δ^2 for the Q-ratio.

In the case of a curved profile the supposed condition $F_1 \cong 1$ could mean that the value of T_c has to adjust itself such that the sum of the BL thicknesses is invariant, i.e., that eq. (4.26) holds. The *volume* of the turbulent bulk then is invariant under deviations from OB conditions, only its time averaged temperature T_c takes notice of the NOB conditions and deviates from T_m. Certainly one has to check in further experiments (or with theoretical argument) if the constraint $\lambda_b^{sl} + \lambda_t^{sl} \cong 2\lambda_{OB}^{sl}$ also holds for other liquids than water in order to validate our finding. We do not know a physical reason why this should be the case in general; it may be incidental for water in the temperature range under investigation.

For a more thorough understanding of the robustness of Nu and also Re against NOB corrections more theoretical insight into the mechanism of the heat transport is required. Therefore we next consider RB convection models. We shall start with the first attempt to explain NOB effects, namely with the model of Wu and Libchaber (1991). It will turn out that their basic assumption is not consistent with the new data. We then, in Section 4.6, extend the Prandtl-Blasius boundary layer theory to T-dependent material parameters. It turns out that this can explain the experimental observations rather well.

4.5 Wu-Libchaber model for NOB effects

Wu & Libchaber [3] and later Zhang *et al.* [4] have studied the influence of deviations from OB conditions, both experimentally and by developing a model to cope with NOB effects on the Nusselt number. Their model extends the ideas of the Chicago scaling model for RB convection [46] by allowing for different temperature drops Δ_b and Δ_t at bottom and top. We shall briefly summarize the Wu-Libchaber (WL) results as far as relevant here, in our notation.

WL also use eq. (4.5), $\Delta_b + \Delta_t = \Delta$. Different top and bottom temperatures imply different thermal boundary-layer thicknesses, which they

introduce by employing heat flux conservation

$$Q = \Lambda_{\bar{b}} \frac{\Delta_b}{\lambda_{\bar{b}}} = \Lambda_{\bar{t}} \frac{\Delta_t}{\lambda_{\bar{t}}} \,. \tag{4.28}$$

These BL thicknesses $\lambda_{\bar{b},\bar{t}}$ are defined in terms of the material properties, *taken at the mean temperatures* $T_{\bar{b}}$ and $T_{\bar{t}}$ in the respective BLs. These temperatures are $T_{\bar{b}} = T_c + \frac{\Delta_b}{2} = \frac{T_c+T_b}{2}$ and $T_{\bar{t}} = T_c - \frac{\Delta_t}{2} = \frac{T_c+T_t}{2}$.

Next, temperature scales θ_b and θ_t are introduced, characterizing the boundary layers in a different way than by the temperature drops Δ_b and Δ_t, namely

$$\theta_b = \frac{\nu_{\bar{b}}\,\kappa_{\bar{b}}}{g\,\beta_{\bar{b}}\,\lambda_{\bar{b}}^3} \;,\; \theta_t = \frac{\nu_{\bar{t}}\,\kappa_{\bar{t}}}{g\,\beta_{\bar{t}}\,\lambda_{\bar{t}}^3} \,. \tag{4.29}$$

From their data (and later from the model of Zhang *et al.* [4]) they concluded that these temperature scales should coincide[‡]. Even more, in the framework of the model these scales are identified with the scale Δ_c of the temperature fluctuations in the bulk,

$$\theta_b = \theta_t = \Delta_c \,. \tag{4.30}$$

These equalities say that the BL thicknesses respond to the different temperature drops at bottom and top in such a way, that the thermal scales communicate through the thermal scale in the bulk. From eqs. (4.28), (4.29), and (4.30) one obtains

$$\chi = \frac{\Delta_b}{\Delta_t} = \frac{\Lambda_{\bar{t}}}{\Lambda_{\bar{b}}} \frac{\lambda_{\bar{t}}}{\lambda_{\bar{b}}} = \frac{\kappa_{\bar{t}}}{\kappa_{\bar{b}}} \left(\frac{\beta_{\bar{t}} \nu_{\bar{b}} \kappa_{\bar{b}}}{\beta_{\bar{b}} \nu_{\bar{t}} \kappa_{\bar{t}}} \right)^{1/3} . \tag{4.31}$$

All material properties are to be taken at the middle temperature of the respective BL. In eq. (4.31) we have replaced the Λ-ratio by the κ-ratio because in water the additional factors ρ, c_p are practically temperature independent.

Since the temperatures $T_{\bar{b}}$ and $T_{\bar{t}}$ which are needed to evaluate the material parameters can be expressed in terms of χ, eq. (4.31) is an implicit equation for the temperature ratio χ. It can be solved iteratively (with fast

[‡]Wu & Libchaber [3] in fact only assumed that θ_b and θ_t *scale* in the same way, and experimentally they found a ratio $\theta_b/\theta_t \neq 1$, independent of Ra, i.e., Δ. This, however, cannot be, as this ratio must become equal to 1 in the OB limit. It might be that the observed asymmetry in [3] originates from the asymmetry of the setup: While the top plate is kept at constant temperature around 5K, a constant heat flux is imposed at the bottom plate.

convergence). The resulting Wu-Libchaber χ_{WL} for the case of water is plotted in Figure 4.6 for comparison with our measured data. Clearly, χ_{WL} is considerably smaller than found in experiment.

What is the origin of this shortcoming of the Wu-Libchaber model? To answer this we have to check the basic assumption eq. (4.30), on which (4.31) is based, i.e., on

$$\chi_\theta = 1\,,\ \text{where}\ \chi_\theta \equiv \frac{\theta_b}{\theta_t} = \frac{\nu_{\bar{b}}\kappa_{\bar{b}}\beta_{\bar{t}}}{\nu_{\bar{t}}\kappa_{\bar{t}}\beta_{\bar{b}}}\cdot\chi_\lambda^{-3} = \frac{\nu_{\bar{b}}\kappa_{\bar{b}}\beta_{\bar{t}}}{\nu_{\bar{t}}\kappa_{\bar{t}}\beta_{\bar{b}}}\cdot\left(\frac{\kappa_{\bar{b}}}{\kappa_{\bar{t}}}\,\chi\right)^{-3}\,. \quad (4.32)$$

This, however, clearly is not the case, as seen from Fig. 4.11, which shows that χ_θ significantly deviates from $\chi_\theta = 1$. The idea of equal temperature scales θ_b and θ_t in the bottom and top BLs is thus not consistent with experiment. For easier comparison with the corresponding Wu-Libchaber plot we show in Fig. 4.12 all ratios also as functions of χ.

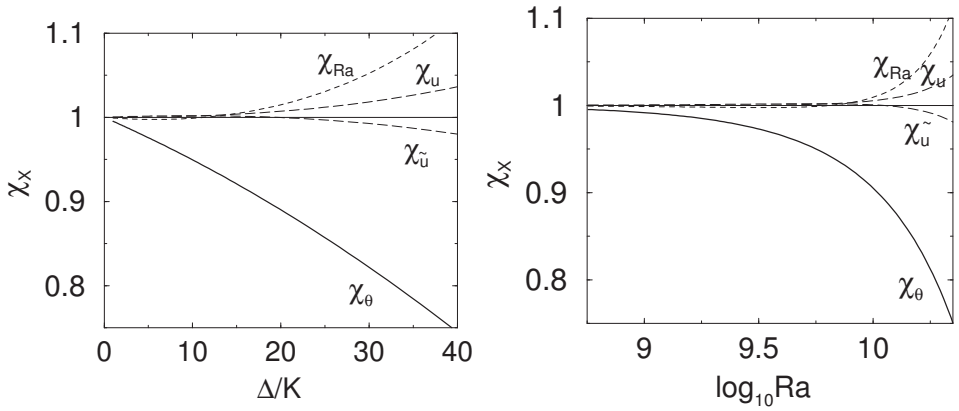

Figure 4.11: The ratios χ_θ (solid), χ_{Ra} (short-dashed), χ_u, $\chi_{\tilde{u}}$ (dashed), for water with $T_m = 40°C$ and $Pr = 4.38$ as functions of Δ (left), and as functions of $Ra = \Delta/\Delta_{m,medium}$ for the medium cell (right). Deviations from $\chi_X = 1$ signal NOB effects. One sees that $\chi_\theta \neq 1$, in conflict with the assumption of Wu & Libchaber [3] underlying their model of NOB effects.

Although the basic assumption $\chi_\theta = 1$ underlying the model of Wu & Libchaber [3] and Zhang *et al.* [4] turns out not to be valid for our experimental data for water, we briefly sketch the derivation of the Nusselt-number modification in the NOB case by these authors. In order to calculate the Nusselt number, Wu & Libchaber [3] adopt the previous hypothesis by Castaing *et al.* [46] and assume that the heat flux Q in the center

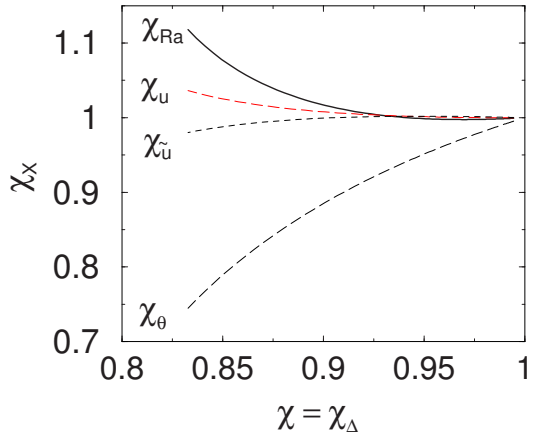

Figure 4.12: The same ratios χ_θ, χ_{Ra}, χ_u and $\chi_{\tilde{u}}$, as functions of the temperature drop ratio $\chi = \Delta_b/\Delta_t = \chi_\Delta$ for water and $T_m = 40°C$.

range is determined by the velocity fluctuation u_c and the temperature fluctuations Δ_c only:

$$Q \sim \rho c_p u_c \Delta_c. \tag{4.33}$$

With $u_c \sim \sqrt{g\beta_c \Delta_c L}$ and with furthermore assuming that the BL temperature scale $\theta_t = \theta_b$ is the same as the bulk temperature fluctuation Δ_c, cf. eq. (4.30), together with $Q = \Lambda_{\bar{t}}\Delta_t/\lambda_{\bar{t}} = \Lambda_{\bar{b}}\Delta_b/\lambda_{\bar{b}}$, cf. eq. (4.28), and the notation

$$\left(\frac{\nu\kappa}{\beta}\right)^{1/3} \frac{1}{\Lambda} \equiv S\,, \tag{4.34}$$

one finally obtains

$$Nu \sim \frac{(\nu_m/\nu_c)^{3/7}}{(\kappa_m/\kappa_c)^{6/7}} \left(\frac{\beta_c}{\beta_m}\right)^{2/7} \left(\frac{2S_c}{S_{\bar{t}} + S_{\bar{b}}}\right)^{9/7} Ra_m^{2/7} Pr_m^{-1/7}\,. \tag{4.35}$$

As in the 1989 Chicago model, one finds the scaling law $Nu \propto Ra^{2/7}$. This scalig law is not globally valid, cf. [47–49] and many other references. It is nevertheless interesting to consider the change of Nu under NOB effects,

$$\frac{Nu_{NOB}}{Nu_{OB}}|_{WL} = \left(\frac{\nu_m}{\nu_c}\right)^{3/7} \left(\frac{\kappa_m}{\kappa_c}\right)^{-6/7} \left(\frac{\beta_c}{\beta_m}\right)^{2/7} \left(\frac{2S_c}{S_{\bar{t}} + S_{\bar{b}}}\right)^{9/7}\,. \tag{4.36}$$

Note that the first three factors in eq. (4.36) $F_3 = \left(\frac{\nu_m}{\nu_c}\right)^{3/7}$, $F_4 = \left(\frac{\kappa_m}{\kappa_c}\right)^{-6/7}$, and $F_5 = \left(\frac{\beta_c}{\beta_m}\right)^{2/7}$ only originate from the fact that the Nusselt numbers are given in terms of Ra and Pr at T_m and are nondimensionalised with κ_m. These factors are not used by Wu & Libchaber [3], as the Rayleigh and Prandtl numbers in the theoretical part of that paper are defined in terms of T_c. Here we use T_m instead of T_c as the reference temperature, because T_m is the external control parameter, while T_c depends on the *a priori* unknown response of the RB flow to NOB conditions and on the material properties at this center temperature.

Although basic assumptions to derive it are not valid, equation (4.36) turns out to describe the measured ratio of the NOB and the OB Nusselt numbers surprisingly well, see Fig. 4.13. Here we calculated the ratio Nu_{NOB}/Nu_{OB} for water in the medium cell as function of Ra with the help of the experimentally determined function $\chi(Ra)$ (and not of χ_{WL}). Not only is the robustness of Nu with respect to NOB effects correctly reflected, but even the small *decrease* of Nu_{NOB} as compared to Nu_{OB} is given by expression (4.36). This holds in spite of the disagreement between the experimental and theoretical χ ratio and the violation of the basic assumption $\chi_\theta = 1$ of the model. We conclude that the value of χ has little effect on the NOB corrections to the Nusselt number, which are robustly very small. A similar conclusion seems to be valid concerning the local Ra-scaling exponent of Nu, since also 2/7 is not verified experimentally.

Let us look at the Δ-dependences of the individual factors of equation (4.36), F_3, F_4, F_5, and $F_6 = \left(\frac{2S_c}{S_{\tilde{t}}+S_{\tilde{b}}}\right)^{9/7}$ in more detail; see figure 4.14. The last factor F_6 again has the property that only the sum of the bottom and the top layer contributions of the quantity S appears. Thus, in lowest, linear order in the temperature deviations also here the NOB effects from the top and bottom BL compensate each other. Indeed, this factor F_6 is nicely described by a *quadratic* dependence on Δ, namely by $F_6 = 1 - 3.07 \cdot 10^{-5}\Delta^2$. The other factors F_i, $i = 3, 4, 5$, however introduce linear dependences on Δ.

Since ratios of bottom and top quantities are of particular interest to characterize deviations from OB conditions quantitatively, $\chi = \chi_\Delta$ in particular, but also $\chi_\kappa, \chi_\nu, \chi_\beta$ (and in the frame of the Wu-Libchaber model also χ_θ), we now check also other such ratios. Consider first the Δ or $\Delta/\Delta_{m,medium} = Ra$ dependence of the ratio of the bottom and top Ray-

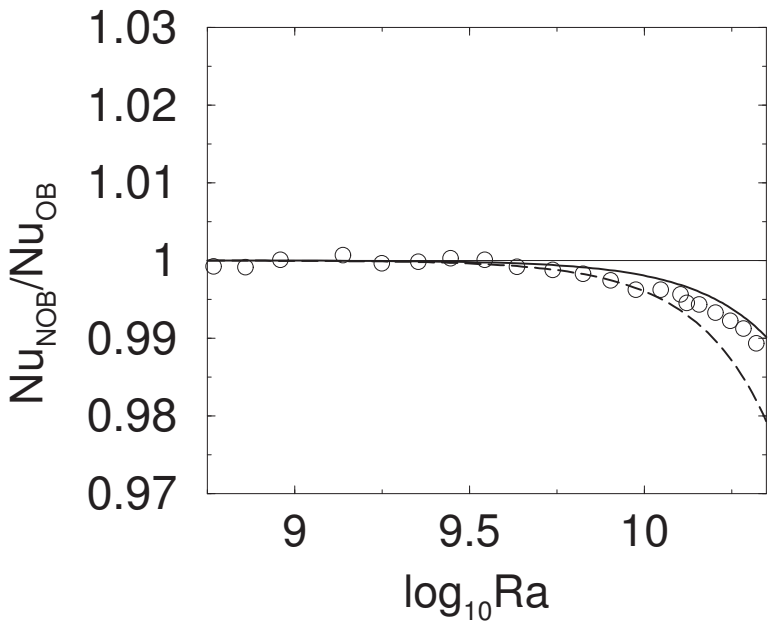

Figure 4.13: Nu_{NOB}/Nu_{OB} versus Ra for water and $T_m = 40°C$ and $Pr = 4.38$ from our measurements with the medium cell (circles), from the Wu-Libchaber model Eq. (4.36) (dashed line) but with the ratio χ as measured in our water experiments in the medium cell, and from the theory of Sect. 4.6 (solid line). Note the scale on the ordinate, as compared to the corresponding ordinate scale on the figures for the χ's: The Nusselt number is very robust to NOB effects.

leigh numbers $\chi_{Ra} = Ra_b/Ra_t$, with

$$Ra_b = \frac{g\beta_{\bar{b}}\lambda_{\bar{b}}^3\Delta_b}{\nu_{\bar{b}}\kappa_{\bar{b}}} = \frac{\Delta_b}{\theta_b} \tag{4.37}$$

and Ra_t correspondingly. We have

$$\chi_{Ra} = \frac{Ra_b}{Ra_t} = \chi\chi_\theta^{-1}. \tag{4.38}$$

The BL thickness ratio in the Wu-Libchaber approximation is $\chi_{\bar{\lambda}} = \frac{\lambda_{\bar{b}}}{\lambda_{\bar{t}}} = \frac{\kappa_{\bar{b}}}{\kappa_{\bar{t}}}\chi$. Furthermore, there are various velocity scales in the RB system. Define w_b as that velocity scale in the BL for which buoyancy is of the order

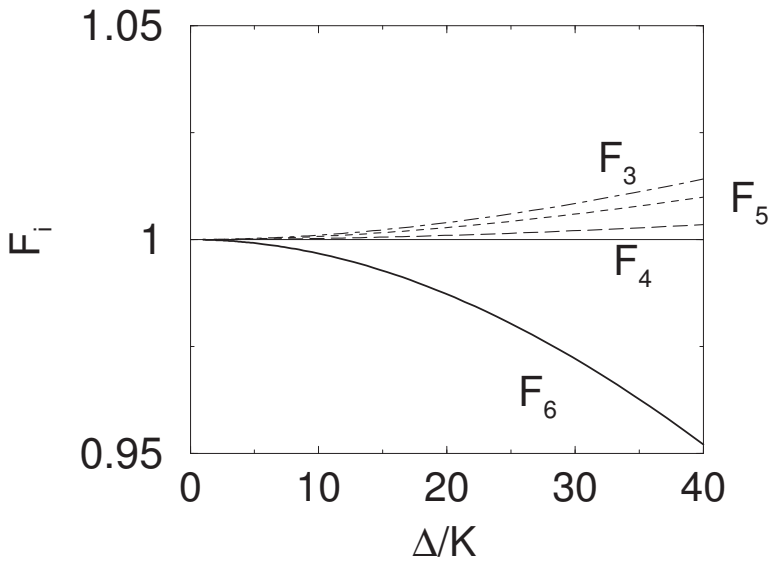

Figure 4.14: The individual factors of eq. (4.36) as functions of Δ for water and $T_m = 40°C$: $F_3(\Delta)$ (short-long-dashed), $F_4(\Delta)$ (long-dashed), $F_5(\Delta)$ (short-dashed), and $F_6(\Delta)$ (solid). The factor F_6 can be fitted by $F_6 = 1 - 3.07 \cdot 10^{-5}\Delta^2$. This fit is indistinguishable from the curve itself.

of the viscous loss, $g\,\beta_{\bar{b}}\,\Delta_b \sim \nu_{\bar{b}} w_b/\lambda_{\bar{b}}^2$, leading to

$$\chi_w = \frac{w_b}{w_t} = \frac{\beta_{\bar{b}}\nu_{\bar{t}}}{\beta_{\bar{t}}\nu_{\bar{b}}}\,\frac{\Delta_b}{\Delta_t}\,\left(\frac{\lambda_{\bar{b}}}{\lambda_{\bar{t}}}\right)^2 = \chi_\beta\,\chi_\nu^{-1}\,\chi\,\chi_\lambda^2\,. \tag{4.39}$$

Also of interest is this velocity scale in the boundary layers. In the bottom BL the relevant length scale is $\lambda_{\bar{b}}$; the relevant temperature difference either is Δ_b or θ_b. Defining thus $u_b = (\beta_{\bar{b}} g \Delta_b \lambda_{\bar{b}})^{1/2}$ and $\tilde{u}_b = (\beta_{\bar{b}} g \theta_b \lambda_{\bar{b}})^{1/2} = \left(\frac{\nu_{\bar{b}}}{\lambda_{\bar{b}}}\,\frac{\kappa_{\bar{b}}}{\lambda_{\bar{b}}}\right)^{1/2}$ one is led to

$$\chi_u = \frac{u_b}{u_t} = \left(\frac{\beta_{\bar{b}}}{\beta_{\bar{t}}}\,\chi\,\chi_\lambda\right)^{1/2} \tag{4.40}$$

and

$$\chi_{\tilde{u}} = \frac{\tilde{u}_b}{\tilde{u}_t} = \chi_\nu^{1/2}\,\chi_\kappa^{1/2}\,\chi_\lambda^{-1}\,. \tag{4.41}$$

Note that $\tilde{u}_b$ (and correspondingly $\tilde{u}_t$) is the geometric mean of the viscous and the thermal molecular velocities in the boundary layer, independent of any buoyancy.

We present various of these ratios for the case of water as working fluid in Figure 4.11 as functions of Δ and of $\Delta/\Delta_{m,medium} = Ra$. They all show prominent NOB effects. The Ra-ratio χ_{Ra} and also $\chi_{\tilde{u}}$ have only moderate deviations from the OB value $\chi_X = 1$. But apparently they too are not Δ-independent constants. For better comparison with Wu and Libchaber's curves [3] we also present the ratios of interest as functions of the preferred measure for NOB effects, the BL temperature ratio $\chi = \chi_\Delta$ (figure 4.12).

4.6 Extension of boundary layer theory to NOB conditions

4.6.1 Motivation

The previous section has shown the shortcomings of the Wu-Libchaber model in explaining the center temperature T_c and thus χ in the examined water NOB case. In this section we will present an alternative theory which will not have these shortcomings and which will be able to consistently account for all measured NOB relative to the OB data for water. It is based on the Prandtl-Blasius theory for laminar BLs [24, 27, 28, 31, 32, 50], extended to temperature dependent viscosity and thermal diffusivity [51]; see also [4, 52], which considered the case of temperature dependent viscosity only. The justification to start from the Prandtl-Blasius BL theory is that for water even for $Ra = 10^{11}$ the wall Reynolds number is not larger than about 100. Indeed, the Grossmann-Lohse unifying theory of RB convection [29, 33, 47, 48], which is able to account for the measured $Nu(Ra, Pr)$ and $Re(Ra, Pr)$ in a considerable part of the parameter space, employs the scaling of the Prandtl-Blasius BL theory as a central ingredient, although the layers certainly show plume separation and therefore time dependence. But they are not yet fully turbulent and therefore not fluctuation dominated.

In subsection 4.2.4 we have already addressed how the BL thicknesses will be modified in the NOB case. We will now calculate the full velocity and temperature profiles and from those derive the center temperature T_c and thus the ratio $\chi = \frac{\Delta_b}{\Delta_t}$ (subsection 6.2), which are found to be in very good agreement with the experimental data. No fitting parameter

has to be introduced. When in addition employing the experimental finding of figure 4.10 that for water the factor F_1 within experimental resolution is $F_1 = 1$ in the Δ-range of interest, meaning that the sum of the top and bottom thermal boundary layer widths (based on the slopes of the temperature profiles at the plates) remains unchanged in the NOB case, the theory also gives the measured small reduction of the Nusselt number for the NOB case and an at most 0.5% increase in the Reynolds number for the Δ considered here, which is also consistent with the experimental data (subsection 6.3). In subsection 6.4 we explore the origin of the NOB corrections by studying hypothetical liquids with only one of the material parameters being temperature dependent. In subsection 6.5 we apply our theory to glycerol and make predictions for the NOB effects in that liquid.

4.6.2 Viscous and thermal boundary layers with temperature dependent viscosity and thermal diffusivity

As pointed out in section 2, for water one can assume to a very good approximation that the fluid density and the isobaric specific heat capacity are constant, i.e., throughout equal to ρ_m and $c_{p,m}$, respectively. In contrast, the temperature dependences of the kinematic viscosity $\nu(T) = \eta(T)/\rho_m$, the thermal diffusivity $\kappa(T) = \Lambda(T)/(c_{p,m}\rho_m)$ are explicitly taken into consideration and calculated according to Appendix A.

In this approximation Prandtl's equation, on which Prandtl's stationary BL theory is based, reads

$$u_x \partial_x u_x + u_z \partial_z u_x = \partial_z (\nu \partial_z u_x). \tag{4.42}$$

Pressure contributions are omitted. u_x is the horizontal velocity component at the bottom or top plates in the direction of the large-scale circulation (the wind of turbulence), and u_z is the vertical velocity component. Both velocity components are taken to be uniform in the lateral, y-direction, *i.e.*, in the direction perpendicular to the wind, and are functions of x and z only. The following boundary conditions apply:

$$u_x(x,0) = 0, \tag{4.43}$$
$$u_z(x,0) = 0, \tag{4.44}$$
$$u_x(x,\infty) = U_{NOB}. \tag{4.45}$$

The longitudinal asymptotic velocity U_{NOB} outside the viscous BL is identified with the wind of turbulence. Note that U_{NOB} is not necessarily the

same as U_{OB}, since it may vary with the bulk properties, in particular with T_c, and thus with Δ. Its value is part of the boundary conditions. For solving the BL equations the only thing which matters is to fix the asymptotic ($z \to \infty$) value of $u_x(x,z)$. The difference between U_{NOB} and U_{OB} will be determined by an additional input, taken from an argument beyond boundary layer theory, namely, the experimental finding that the sum of the *physical* boundary layer thicknesses for water has been measured as independent of Δ.

Analogously, the thermal boundary layer is described by:

$$u_x \partial_x T + u_z \partial_z T = \partial_z (\kappa \partial_z T) , \tag{4.46}$$

with the boundary conditions:

$$T(x,0) = T_b \text{ or } T(x,0) = T_t, \tag{4.47}$$

$$T(x,\infty) = T_c. \tag{4.48}$$

The two possible boundary conditions describe two plates facing each other, one being the top plate and the other one the bottom plate. The asymptotic temperature of the fluid outside of each thermal BL is T_c, which under NOB conditions is not the same as T_m. Its value is part of the boundary conditions as well and will be determined by the constraint that the thermal current across the RB container is conserved, as will be explained below.

Now, the temperature is measured as the deviation from the top temperature and is non-dimensionalized[§] with Δ,

$$\tilde{\Theta} = \frac{T - T_t}{\Delta} = \frac{T - T_m}{\Delta} + \frac{1}{2} . \tag{4.49}$$

Then $\tilde{\Theta}_m = 1/2$ and the thermal boundary conditions for the bottom and top plates read $\tilde{\Theta}_b = 1$ and $\tilde{\Theta}_t = 0$. The central new element as compared to the standard laminar BL theory is that both the kinematic viscosity and the thermal diffusivity are now temperature dependent – in dimensionless form $\tilde{\nu}(\tilde{\Theta}) = \nu(T)/\nu_m$ and $\tilde{\kappa}(\tilde{\Theta}) = \kappa(T)/\kappa_m$, respectively, giving rise to extra terms when performing the z-derivatives on the right hand sides of eqs. (4.42) and (4.46), respectively.

We now reduce eqs. (4.42) and (4.46) to ODEs by introducing a stream-function Ψ and then by employing its self-similarity under x and z changes.

[§]Distinguish $\tilde{\Theta}$ from θ, the temperature in K as measured from the chosen reference temperature, usually T_m, introduced already above.

A stream-function Ψ can be introduced because Prandtl's BL theory deals with two-dimensional, incompressible flow. It satisfies $u_x = \partial_z \Psi$ and $u_z = -\partial_x \Psi$. In analogy with the OB-case, we introduce the transverse length-scale ℓ_{NOB}:

$$\ell_{NOB} \equiv \sqrt{\frac{x\nu_m}{U_{NOB}}}. \tag{4.50}$$

This length scale is defined in terms of the asymptotic velocity U_{NOB} as the velocity scale, since this choice guarantees that the boundary condition for the stream-function will always be $\tilde{\Psi}'(\infty) = 1$, independent of Δ. As U_{NOB} is a priori unknown, so is ℓ_{NOB}. Next, the similarity variable $\tilde{Z}$ is introduced,

$$\tilde{Z} \equiv z\sqrt{\frac{U_{NOB}}{x\nu_m}} = \frac{z}{\ell_{NOB}}. \tag{4.51}$$

The stream function $\Psi(x,z)$ is assumed to depend on this (x,z)-combination only, implying a self-similar solution. As in the standard Prandtl theory, Ψ is non-dimensionalized as

$$\tilde{\Psi}(\tilde{Z}) = \frac{\Psi(x,z)}{\ell_{NOB}\, U_{NOB}}. \tag{4.52}$$

With this nondimensional self-similarity ansatz for the stream function one finds from the Prandtl equation (4.42) the ODE

$$\tilde{\nu}\,\tilde{\Psi}''' + \left(\frac{1}{2}\tilde{\Psi} + \frac{d\tilde{\nu}}{d\tilde{\Theta}}\,\tilde{\Theta}'\right)\tilde{\Psi}'' = 0. \tag{4.53}$$

The boundary conditions are

$$\tilde{\Psi}(0) = 0, \tag{4.54}$$

$$\tilde{\Psi}'(0) = 0, \tag{4.55}$$

$$\tilde{\Psi}'(\infty) = 1. \tag{4.56}$$

Note that the velocity profile $\tilde{\Psi}' = u_x/U_{NOB}$ depends explicitly on viscosity and implicitly on the thermal diffusivity (since the $\tilde{\Theta}$ profile depends on Pr, as will be shown below, cf. eq.(4.57)). Therefore, the solution of the dimensionless boundary value problem (4.53)-(4.56) is *nonuniversal*. Namely, it depends on the material parameters and their respective temperature dependences.

Correspondingly, from the temperature equation (4.46) one obtains for the similarity function $\tilde{\Theta}$, describing the temperature field $\tilde{\Theta}(x,z) = \tilde{\Theta}(\tilde{Z})$

$$\tilde{\kappa}\,\tilde{\Theta}'' + \left(\frac{1}{2}\,\mathrm{Pr}\,\tilde{\Psi} + \frac{d\tilde{\kappa}}{d\tilde{\Theta}}\,\tilde{\Theta}'\right)\tilde{\Theta}' = 0. \tag{4.57}$$

There are two possible boundary conditions, either for the bottom or for the top BL

$$\tilde{\Theta}(0) = \tilde{\Theta}_b = 1 \text{ or } \tilde{\Theta}(0) = \tilde{\Theta}_t = 0\,, \tag{4.58}$$

$$\tilde{\Theta}(\infty) = \tilde{\Theta}_c\,. \tag{4.59}$$

Thus in the RB configuration, each thermal plate is associated with a boundary layer described by (4.53)-(4.56) coupled to (4.57)-(4.59). Therefore, in principle, it would be just a matter of integrating the top and bottom BL-equations, as done in the OB-case. However, the NOB-case has a subtle point: the asymptotic temperature $\tilde{\Theta}_c = \frac{T_c - T_t}{\Delta}$, with $0 < \tilde{\Theta}_c < 1$, is a *response* parameter, which has not been fixed yet. Therefore, in order to solve the BL equations, one has first to identify the centre (bulk) temperature T_c and thus the boundary-condition (4.59).

We determine $\tilde{\Theta}_c$ by the constraint that the thermal flux across the cell is conserved and therefore the influx at the bottom must be the same as the outflux at the top, $J(z=0) = J(z=L)$. This means

$$\kappa_b\, \partial_z T|_b = \kappa_t\, \partial_z T|_t \tag{4.60}$$

or in dimensionless form

$$\tilde{\kappa}_b \left|\tilde{\Theta}'_b\right| = \tilde{\kappa}_t\, \tilde{\Theta}'_t\,. \tag{4.61}$$

This determines the bulk temperature $\tilde{\Theta}_c$.

The BL equations (4.53)-(4.56) and (4.57)-(4.59) are iteratively solved until condition (4.61) is satisfied. Technically, this can e.g. be achieved with a shooting method cf. [53]. The solution gives the center temperature T_c (shown in figure 4.5), or alternatively the temperature drops Δ_t and Δ_b (shown in figure 4.4) over the top and bottom thermal BLs and of course their ratio χ (shown in figure 4.6). All these theoretical results are in good agreement with our measurements. We stress that the computation is based on two ingredients only: (i) the dimensionless BL-equations, (4.53)-(4.56) and (4.57)-(4.59), assisted by the given temperature dependences of the fluid properties and (ii) the conservation of the thermal current. No additional input or fitting parameter is needed.

The solution of the BL equations also gives the dimensionless velocity and temperature profiles, see figure 4.15. Both the kinetic and the thermal bottom BLs are thinner than the respective top BLs, as already argued in section 4.2 for the thermal BLs. In the right panel of figure 4.15 the difference in the slope-based thermal BL thicknesses λ_b^{sl} and λ_t^{sl} is explicitly

shown. It is also seen that $\tilde{\Theta}_c$ is larger than $\tilde{\Theta}_m = 1/2$. All NOB profiles are characterized by a pronounced curvature, as also already qualitatively discussed in section 5.2.

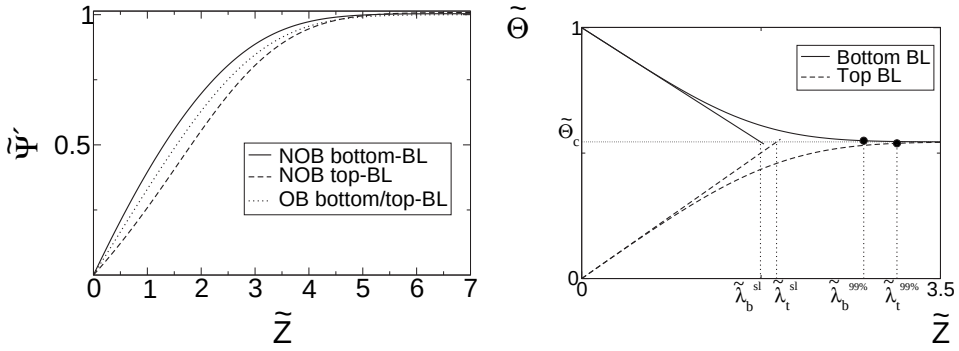

Figure 4.15: (Dimensionless) longitudinal velocity $\tilde{\Psi}' = u_x/U_{NOB}$ (left) and temperature $\tilde{\Theta}$ (right) profiles for water at $T_m = 40^o$ C and $\Delta = 40^o$ C in the NOB-case. The center temperature $\tilde{\Theta}_c$ is larger than the mean temperature $\tilde{\Theta}_m = 0.5$. The bottom slope-based thermal BL is smaller than the corresponding one at the top plate, $\lambda_b^{sl} < \lambda_t^{sl}$.

Figure 4.16 shows the moduli of the dimensionless temperature slopes $\tilde{\Theta}'$: They are different at the top and bottom plates and vary strongly with height (z), due to the temperature dependence of the thermal diffusion coefficient.

The temperature and velocity profiles remain to be measured. Note that the theory can only predict the *shape* of the profile including its nondimensional thickness, but not its absolute, physical thickness, since the yet unknown velocity U_{NOB} (and derived from this the unknown transverse length-scale ℓ_{NOB}) is involved in the nondimensionalization.

4.6.3 Application of NOB boundary layer theory to Nu and Re

The lack of knowledge of U_{NOB} (and thus of ℓ_{NOB}) also is the reason why the Nusselt number Nu_{NOB} cannot yet be calculated. This is of course not surprising as the considered BL theory does not take notice of the thermal expansion coefficient β, which is responsible for the buoyant driving of the flow. We have calculated, instead, the change of Nu_{NOB} *relative to* Nu_{OB} due to the NOB influences. The relevant formulas are eqs.

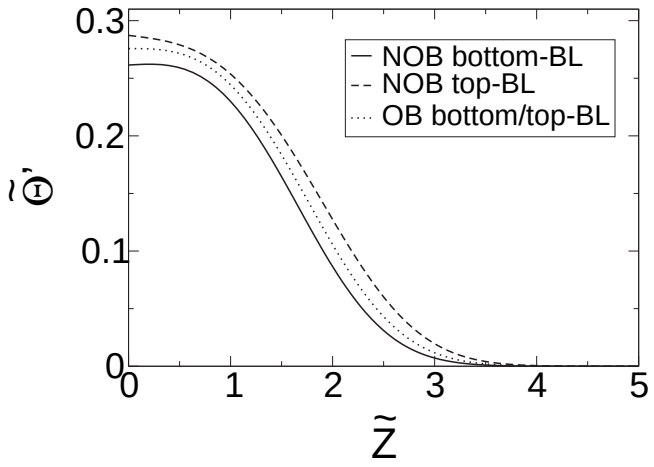

Figure 4.16: (Dimensionless) slope of the temperature profiles in the top and bottom NOB thermal BLs. The same liquid (water) and parameters T_m, and Δ as in figure 4.15 is chosen.

(4.22),(4.23),(4.24). While F_2 can be calculated from the nondimensionalized BL theory immediately, because only nondimensional NOB quantities enter, the ratio of the sum of the BL thicknesses $F_1 = 2\lambda^{sl}_{OB}/(\lambda^{sl}_t + \lambda^{sl}_b)$, cf. eq. (4.23), contains the length ratio $\ell_{OB}/\ell_{NOB} = \sqrt{U_{NOB}/U_{OB}}$. Since the velocities U_{NOB}, U_{OB} feel the buoyancy in the bulk, they are expected to be influenced by the NOB-changes of the thermal expansion coefficient from β_m to β_c.

In order to determine the ratio U_{NOB}/U_{OB} we require the thickness ratio F_1, see eq.(4.23). From our experiments with water we know for that case and within experimental resolution that $F_1 = 1$, i.e., the sum of the physical top and bottom thermal BL thicknesses remains constant under deviations from OB conditions, see figure 4.10 in section 4.4. Therefore we can use F_1, here $F_1 = 1$, as an additional ingredient from experiment to be able to calculate Nu_{NOB}/Nu_{OB} within the extended BL theory.

Write F_1 in terms of the dimensionless thicknesses and the respective length scales,

$$F_1 \;=\; \frac{2\,\tilde{\lambda}^{sl}_{OB}}{\tilde{\lambda}^{sl}_t + \tilde{\lambda}^{sl}_b}\,\frac{\ell_{OB}}{\ell_{NOB}} \;=\; \tilde{F}_1\sqrt{\frac{U_{NOB}}{U_{OB}}}\,. \tag{4.62}$$

Then one has

$$\frac{U_{NOB}}{U_{OB}} = \frac{Re_{NOB}}{Re_{OB}} = \left(\frac{F_1}{\tilde{F}_1}\right)^2. \tag{4.63}$$

The nondimensional factor $\tilde{F}_1 = 2\ \tilde{\lambda}^{sl}_{OB}/(\tilde{\lambda}^{sl}_t + \tilde{\lambda}^{sl}_b)$ is fully provided by the Prandtl-Blasius boundary layer theory, namely by the integration of (4.53)-(4.56) together with (4.57)-(4.59). F_1 is taken as an input from experiment, here $F_1 = 1$. Then eq.(4.63) determines the U or Re ratio.

With the same experimental input of F_1 (in particular $F_1 = 1$ for the water case), the Nusselt number ratio follows from the exact relation (4.22),

$$\frac{Nu_{NOB}}{Nu_{OB}} = \frac{2\lambda^{sl}_{OB}}{\lambda^{sl}_t + \lambda^{sl}_b} \cdot \frac{\kappa_t\Delta_t + \kappa_b\Delta_b}{\kappa_m\Delta} = F_1 \cdot F_2 = F_2 = \frac{\kappa_t\Delta_t + \kappa_b\Delta_b}{\kappa_m\Delta}, \tag{4.64}$$

i.e., directly from the results for Δ_t and Δ_b of the previous subsection. The resulting dependence of the heat flux ratio on Δ or on $Ra = \frac{\beta_m g L^3}{\nu_m \kappa_m}\Delta$ was shown in figure 4.13, together with the experimental data. Very good agreement is seen. Not only the robustness of the Nusselt number towards NOB corrections is found, but even the tiny 1% *decrease* of Nu_{NOB} as compared to Nu_{OB}. The Reynolds number ratio $Re_{NOB}/Re_{OB} \propto \tilde{F}_1^{-2}$, cf. eq. (4.63), is shown in figure 4.17. Also the Reynolds number turns out to be very robust towards NOB corrections. It increases by about 0.5% as compared to the OB case. This theoretical finding also is consistent with our measurements (cf. figure 4.8), showing less than 2% variation of Re_{NOB} (which is our experimental error bar) due to NOB effects.

4.6.4 Origin of NOB corrections for χ and Nu

In order to shed light on the origin of the various features of the NOB corrections, of the Nu robustness in particular, we now consider the NOB corrections for hypothetical liquids with (i) $\nu(T)$ as in water, but $\kappa = \kappa_m$ being constant and (ii) $\kappa(T)$ as in water, but $\nu = \nu_m$ being constant. The results for χ are shown in figure 4.18. For the ratios Nu_{NOB}/Nu_{OB} and Re_{NOB}/Re_{OB} as displayed in figure 4.19 we in addition assume that $F_1 = 1$ also for the hypothetical liquids. Note that Δ_b, Δ_t, χ, and F_2 can be calculated from the BL theory without any fit parameter and without any measured data, using only theory and the given material properties. But in order to determine the Nu- and Re-ratios, we again have to know F_1. Although obviously F_1 cannot be measured for hypothetical liquids, we still assume $F_1 = 1$ as an extra hypothesis. These calculations with hypothetical liquids quantify our qualitative discussions of section 4.4.

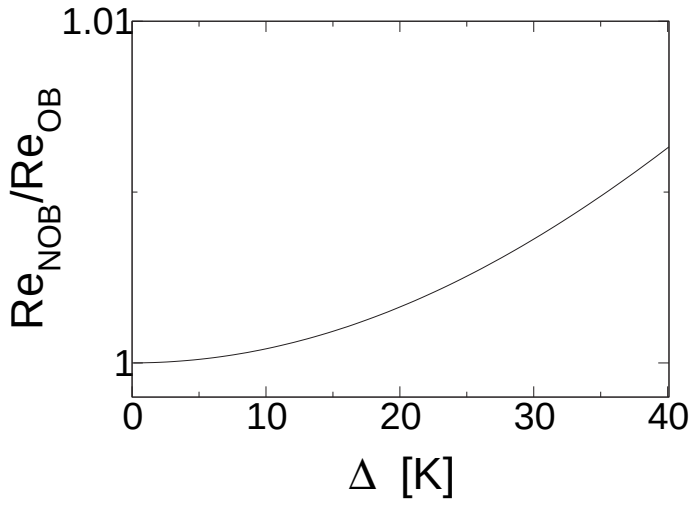

Figure 4.17: Re_{NOB}/Re_{OB} versus Δ for the medium cell with $T_m = 40°C$ and $Pr = 4.38$ from the theory of section 4.6. Note the scale of the ordinate, as compared to the ordinate scale in the figures for the χ's: Also the Reynolds number is very robust towards NOB corrections. Due to the deviations from the OB conditions the wind amplitude slightly increases, while the heat current was found to slightly decrease.

From the figures we conclude that T_c and thus Δ_b, Δ_t, and χ are mainly determined by the temperature dependence of the viscosity $\nu(T)$. The variation of the thermal diffusivity $\kappa(T)$ with T has only a small influence on these quantities. In contrast, within our theory the Nusselt number modification under NOB effects is exclusively determined by the temperature dependence of $\kappa(T)$. As can be seen easily from eq. (4.22), a temperature dependence of the viscosity $\nu(T)$ but with $\kappa = \kappa_m$ being constant, has no effect on the Nusselt number, in spite of the modification of the central temperature (remember always that $F_1 = 1$ is assumed).

The physical reason that Nu and Re are so robust under large changes of the material parameters with the temperature is that F_2 does not take notice of the linear, dominant variations of κ, ν, etc. F_2 is affected only by the higher order, nonlinear changes of the material parameters. These are visible as curvatures (or even the changes of those) of $(\kappa(T) - \kappa_m)/\kappa_m$, $(\nu(T) - \nu_m)/\nu_m$, etc., as seen in Figure 4.22. The dominant, linear contributions in the material parameters cancel by the shift of the bulk temperature $T_m \to T_c$.

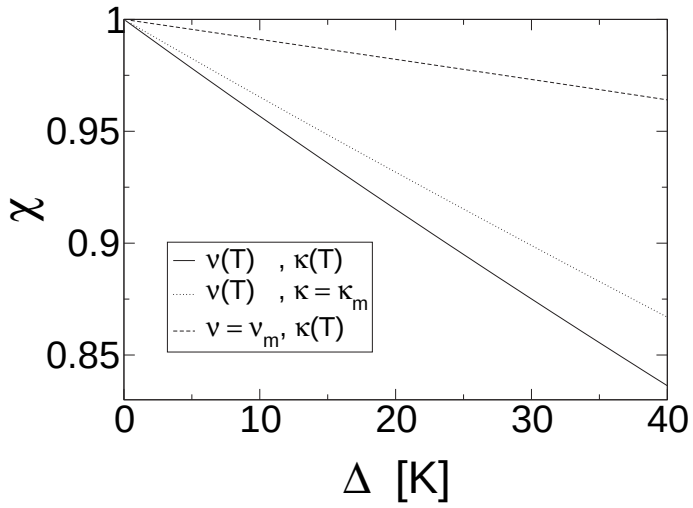

Figure 4.18: $\chi = \Delta_b/\Delta_t$ versus Δ for the medium cell with $T_m = 40°C$, but filled with hypothetical liquids. The solid line takes the full temperature dependence of both $\nu(T)$ and $\kappa(T)$ into consideration, i.e., represents real water. The dotted line shows χ for a hypothetical liquid with $\nu(T)$ as in water, but κ_m being constant. Vice versa, the dashed line shows the ratio χ for a hypothetical liquid with $\kappa(T)$ as in water, but ν_m being constant. Only the extended Prandtl-Blasius BL theory is used; there is no further experimental input.

To understand this cancellation of the bottom and top NOB effects in linear ($\propto \Delta$) order even analytically as far as F_2 is concerned, we apply a systematic expansion of the involved quantities in terms of Δ. We have from Figure 4.5, caption, that $(T_c - T_m)/\Delta = c_2\Delta + c_3\Delta^2 + c_4\Delta^3$ and from the appendix, eq. (4.67) the expansions $\kappa_{b,t}/\kappa_m = 1 \pm a_{\kappa,1}\Delta/2 + a_{\kappa,2}\Delta^2/4 \pm a_{\kappa,3}\Delta^3/8$; here $\pm$ corresponds to b, t (bottom, top). This leads to

$$F_2(\Delta) = 1 + d_2\Delta^2 + d_3\Delta^3 + d_4\Delta^4 \,. \tag{4.65}$$

One easily convinces oneself that the linear terms $\propto \Delta$ cancel. The deviation from $F_2 = 1$ starts with Δ^2. Between the contributing coefficients the following relations are valid.

$$d_2 = \frac{a_{\kappa,2}}{4} - a_{\kappa,1}\, c_2 \;,\; d_3 = -a_{\kappa,1}\, c_3 \;,\; d_4 = -(a_{\kappa,1}\, c_4 + a_{\kappa,3}\, c_2)\,. \tag{4.66}$$

With the numerical values for the $a_{\kappa,i}$ from table 4.2 and for the c_j from

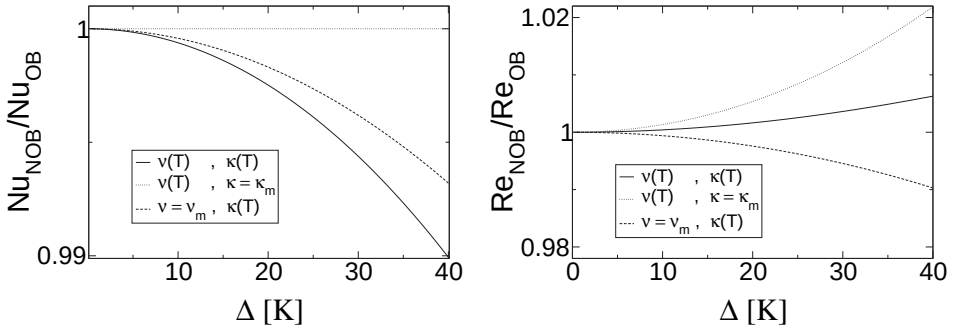

Figure 4.19: Nu_{NOB}/Nu_{OB} (left) and Re_{NOB}/Re_{OB} (right) versus Δ for the medium cell with $T_m = 40°C$, filled with either water (solid lines) or with hypothetical liquids (dashed or dotted lines). The solid lines are valid if the temperature dependence of both $\nu(T)$ and $\kappa(T)$ as in water is taken into account. The dotted lines show the Nusselt and Reynolds number changes for a hypothetical liquid with $\nu(T)$ as in water, but κ_m being constant. Vice versa, the dashed lines show these numbers for a hypothetical liquid with $\kappa(T)$ as in water, but ν_m being constant. For comparison the value $F_1 = 1$ for the factor describing the OB/NOB boundary layer thickness ratio is used also for the hypothetical liquids.

the caption of Figure 4.5 one obtains $d_2 = -7.2 \times 10^{-6} K^{-2}$, in good agreement to what had been found from the data for F_2, see inset of Figure 4.10. Both terms in the sum for d_2, the quadratic order κ-coefficient as well as the product of the linear order κ- times the linear order $\frac{T_c - T_m}{\Delta}$-contribution are negative and amplify their effects. For the next coefficient one calculates $d_3 = 3.2 \times 10^{-8} K^{-3}$. The fourth order term d_4 consists of the first term only, since according to table 4.2 one has $a_{\kappa,3} = 0$. This gives $d_4 = -3.2 \times 10^{-10} K^{-4}$. Equations (4.65) and (4.66) give a consistent analytical description of the thermal NOB effects, connecting $\kappa(T)$ with T_c. All these statements also hold for Nu_{NOB}/Nu_{OB}, as long as $F_1 = 1$, as we have measured for water in the temperature range under investigation.

The quadratic dependence of F_2 on Δ is in agreement with experiment (see figure 4.10) and has been discussed in section 4.4. We now also understand what sets the *direction* of the NOB correction to the Nusselt number (provided $F_1 = 1$): It is the sign of the sum constituting $d_2 = -a_{\kappa,1} c_2 + a_{\kappa,2}/4$. The factor $a_{\kappa,1}$ results from the temperature dependence

of the thermal diffusivity, while the factor c_2 in addition strongly depends on the temperature dependence of the viscosity $\nu(T)$; it immediately reflects whether T_c is larger than T_m (as for water) or smaller. Furthermore, the curvature coefficient $a_{\kappa,2}$ of the thermal diffusivity $\kappa(T)$ contributes to the sign of the deviation $T_c - T_m$. For water both terms in the sum are negative, thus add to the down shift of Nu_{NOB}/Nu_{OB}. As emphasized already, the effect is quadratic in Δ. The linear contributions from the top and the bottom BLs cancel.

The NOB modifications on the Reynolds number Re are more subtle, see figure 4.19, right. For water, the NOB effects of a temperature dependent viscosity with a constant thermal diffusivity (resulting in a slight enhancement of Re) and those of a temperature dependent thermal diffusivity with a constant viscosity (resulting in a slight decrease of Re) partly compensate each other, leading to only a tiny net enhancement of Re. The reason for the enhanced Reynolds number for the case $\nu(T)$, $\kappa = \kappa_m$ is the overall temperature increase in the cell, $T_c > T_m$, resulting in a smaller cell-averaged viscosity. Note again that according to our theory this does not have any effect on the Nusselt number. The reason for the reduced Reynolds number for the case $\kappa(T)$, $\nu = \nu_m$ is less obvious. Technically, it results from $\tilde{F}_1 > 1$, i.e., $2\tilde{\lambda}^{sl}_{OB} > \tilde{\lambda}^{sl}_t + \tilde{\lambda}^{sl}_b$. But remember that for this discussion we have always made the assumption $F_1 = 1$.

4.6.5 NOB effects in glycerol

We now theoretically consider NOB effects for another liquid besides water, namely for glycerol. The reason is to have an independent test for our theory, as there are data for $T_c - T_m$ available from [4]. In that work also Nusselt numbers are offered, but not the ratio Nu_{NOB}/Nu_{OB}. The glycerol case is a particularly interesting one, because this liquid shows a dramatic change of viscosity $\nu(T)$ with temperature, while the T-dependence of the thermal diffusivity $\kappa(T)$ is rather weak. Thus glycerol is a liquid that approximately behaves like one of the hypothetical liquids studied in the previous subsection.

In the RB cell of Zhang *et al.* [4], the mean operating temperature for glycerol is sometimes near $T_m = 40°C$ but is not kept fixed as in our measurements. With $\Delta = 10$ K and their cell height $L = 18.3$ cm (the cell is a cubic box, so $\Gamma = 1$) the Rayleigh number is $Ra = 1.29 \times 10^7$. The temperature dependences of the material properties for glycerol are known and can be found in appendix A, table 4.3. As we have detailed above, within our BL theory the knowledge of the temperature dependent viscos-

ity $\nu(T)$ and and thermal diffusivity $\kappa(T)$ is enough to calculate the shift of the center temperature $T_c - T_m$ as a function of Δ, without any fit parameter. Our result is shown in figure 4.20 and compared with the measured data from ref. [4]. Indeed, our theory is able to reasonably describe the considerable deviation of T_c from T_m also for this case. Fig. 4.20b shows the corresponding temperature drop ratio $\chi = \Delta_b/\Delta_t$. The increase in T_c as compared to T_m and therefore the deviation from $\chi = 1$ is much more pronounced than for water, shown in Fig. 4.6. Instead of $\chi = 0.83$ for water we find $\chi = 0.52$ for glycerol, both for $\Delta = 40$K. Apparently the deviations from linearity are also stronger than for the water case in Fig. 4.6.

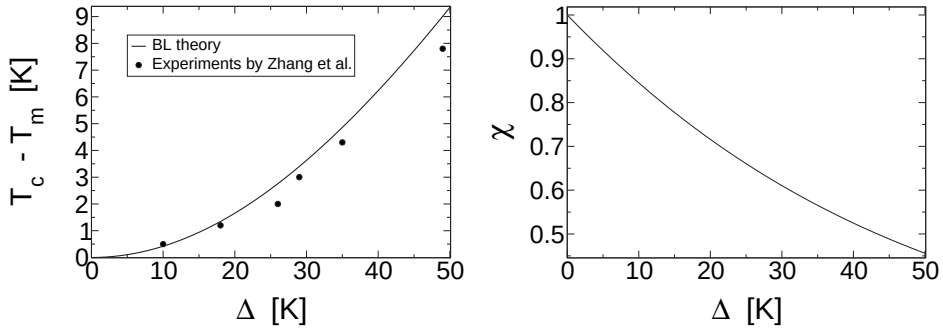

Figure 4.20: (a) The temperature shift in the center of the cylinder filled with glycerol at $T_m = 40°$C as a function of Δ. Some experimental values measured by Zhang *et al.* [4] are also displayed, although for them constant T_m is not valid. Thus the data can only serve for an approximate comparison. This still is reasonably promising. (b) The ratio $\chi = \Delta_b/\Delta_t$ as a function of Δ for glycerol; $T_m = 40°$C. Note that $T_c - T_m$ is much larger (about 6.5 K) in glycerol than in water (about 1.8 K), both for $\Delta = 40$ K. The temperature drop ratio χ for glycerol varies by about 50%.

We finally present the Nusselt number ratio under NOB conditions in terms of F_1 in Fig. 4.21. Note that F_1 is still unknown for glycerol. If also for glycerol the conservation of the sum of thicknesses of the thermal BLs under NOB deviations held, $F_1 = 1$, the plot would show the Nusselt number ratio directly. For a temperature difference $\Delta = 40$K the relative shift is less than about 0.3%, even much less than for water. This is in agreement with the small temperature dependence of $\kappa(T)$, which leads to a factor $F_2 = \frac{\kappa_t}{\kappa_m}\frac{\Delta_t}{\Delta} + \frac{\kappa_b}{\kappa_m}\frac{\Delta_b}{\Delta} \approx 1$.

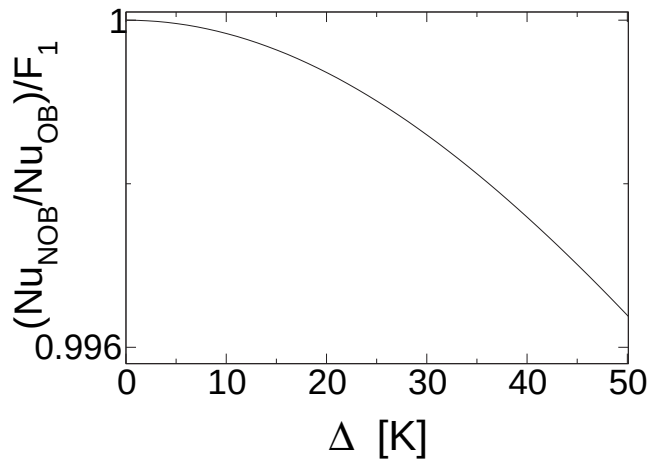

Figure 4.21: The change of the Nusselt number for glycerol under NOB effects. Since no experimental information on the ratio of the total boundary layer thicknesses $F_1 = 2\lambda^{sl}_{OB}/(\lambda^{sl}_b + \lambda^{sl}_t)$ is available, we have plotted the Nusselt number divided by F_1, i.e., the factor F_2. If we assume that $F_1 \approx 1$ as in water, then the NOB shift in the Nusselt number will be tiny, as anticipated from the hypothetical liquid with temperature dependent $\nu(T)$ while κ is (for glycerol only nearly) constant.

Clearly, it is of high interest to measure the Nu shift under NOB conditions also in glycerol, in order to confirm whether the BL layer thickness sum rule holds. With the then available function F_1 also the Reynolds number modification, Re_{NOB}/Re_{OB}, would also follow. Both results will shed light on the respective roles of the temperature dependences of the viscosity $\nu(T)$ and of the thermal diffusivity $\kappa(T)$. Also the nontrivial validity of the extended Prandtl-Blasius BL theory for the NOB case could be confirmed.

4.7 Summary and conclusions

We have measured NOB effects on the ratio χ of the bottom and top temperature drops across the thermal BLs and on the Nusselt number Nu and the Reynolds number Re for turbulent Rayleigh-Bénard convection in water. While χ can vary considerably (up to 20% in the considered case), the NOB effects on Nu and Re are very small, resulting in only a less than 2%

reduction of Nu and no modification of Re within experimental accuracy (which for Re-measurements is about 2%). This holds even though the viscosity and the thermal expansion coefficient vary by more than a factor of two between the top and bottom plates. We have theoretically accounted for this robustness of Nu and Re towards NOB effects: The NOB corrections from the top and bottom BLs compensate each other in first order by appropriately shifting the center temperature $T_m \rightarrow T_c$. We believe that this conclusion is valid beyond the assumptions of constant c_p and ρ. We also expect that it will hold more generally than for water at least for all systems with Pr larger than 1. Then always the thermal boundary layers are nested into the kinetic ones. The robustness of the Nusselt number against NOB effects because of the cancellations will thus hold more generally. We have also shown that one of the basic assumptions of the NOB model by Wu & Libchaber [3] and Zhang *et al.* [4] is in conflict with the experimental data. Nonetheless, also that model shows the robustness of Nu towards NOB effects.

An interesting, unexpected and nontrivial finding for water as the working liquid is the observation, that in the considered temperature range the sum of the slope based BL thicknesses $\lambda_b^{sl} + \lambda_t^{sl}$ seems to be invariant under deviations from OB conditions. Within experimental precision it turned out to be constant for even strong NOB effects. The ratio of the NOB and OB heat fluxes Q_{NOB}/Q_{OB} can then be calculated on the basis of the thermal diffusivities κ_b and κ_t at bottom and top and on that of the measured or theoretically evaluated (BL theory) temperature drops Δ_b and Δ_t, cf. eq. (4.27). This ratio is of second order in Δ and thus in NOB effects.

The employed theory is based on the Prandt-Blasius theory for laminar BLs, extended to temperature dependent viscosity and thermal diffusivity. Remarkably, we do not have to make any use of the temperature dependence of the thermal expansion coefficient. The theory gives a center temperature T_c in very good agreement with the experimental data, without employing any free parameter. With the experimental finding that for water the sum of the slope based thermal BL thicknesses seems to be invariant under deviations from OB, the theory also gives Nusselt and Reynolds number modifications consistent with the measurements. The theory offers the opportunity to discuss hypothetical liquids with only *one* material parameter being temperature dependent, thus shedding light on the mechanism of the NOB corrections: Whereas the NOB correction on χ mainly originates from the temperature dependence of the viscosity, the NOB correction on the Nusselt number exclusively (if $F_1 = 1$) originates

from the temperature dependence of the thermal diffusivity.

To further validate our theory, a next step would be to extend the experiments on Rayleigh-Bénard flow under NOB conditions to other liquids, such as e.g. glycerol.

An exciting extension would be to analyse NOB effects also for gases, in particular for those close to the critical point. Then one may have to take Schwarzschild corrections into consideration. Here an interesting case is when the mean temperature is above the critical temperature and the mean density corresponds to the critical value. In that case, the top and bottom boundary layers are nearly symmetric, but nonetheless the fluid properties can vary significantly within them [54]. These interesting problems go beyond the scope of the present chapter. From a theoretical point of view the challenge in the analysis of NOB effects in gases lies in the temperature dependences of the density and the specific heat capacity, which can be and have been considered as constants in the present chapter.

The role of the Grossmann-Lohse theory in the present context is to give $\mathrm{Nu}(\mathrm{Ra},\mathrm{Pr})$ and $\mathrm{Re}(\mathrm{Ra},\mathrm{Pr})$, as long as Δ is small enough to allow neglecting NOB effects. We have seen that in experiment Δ needs not be too small for OB conditions to hold due to the small effects of deviations from OB conditions, the corrections increasing only $\propto \Delta^2$. While in the present work the BL effects have been dealt with, an extension of GL theory allows one to *calculate* also $\mathrm{Nu}_{\mathrm{NOB}}$ and $\mathrm{Re}_{\mathrm{NOB}}$ immediately, without further input from experiment. This extended GL theory will be addressed separately. It in particular takes the T-dependence of the expansion coefficient $\beta(T)$ into account explicitly.

Acknowledgments

This work was initiated at the Lorentz-Center Workshop on turbulent thermal convection in Leiden in June 2003 and we would like to express our gratitude to Wim van Saarloos for making such workshop possible. We thank Alexei Nikolaenko for his contributions to the experiments and Enrico Calzavarini and Kazuyasu Sugiyama for discussion. The work in Twente is part of the research program of FOM, which is financially supported by NWO, and it was also supported (for DL and SGn) by the European Union (EU) under contract HPRN-CT-2000-00162. The work at Santa Barbara was supported by the U.S. Department of Energy through Grant DE-FG02-03ER46080.

Appendix: Physical properties of water and glycerol

The relative deviations $(X-X_m)/X_m$ from their values X_m at $T_m = 40°C$ of various physical properties X of water at a pressure of one bar are shown in Fig. 4.22. One sees immediately that the properties with significant

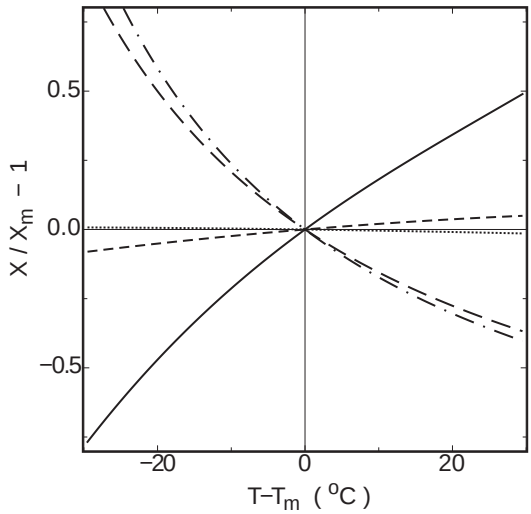

Figure 4.22: The relative deviations $(X - X_m)/X_m$ of water properties X from their values X_m at T_m for $T_m = 40°C$. Solid line: isobaric thermal expansion coefficient β. Long dashed line: kinematic viscosity ν. Short dashed line: thermal conductivity Λ. Dash-dotted line: Prandtl number Pr. Dotted line: density ρ.

temperature dependences are the thermal expansion coefficient β and the kinematic viscosity ν. The cubic polynomial

$$\frac{X - X_m}{X_m} = a_1(T - T_m) + a_2(T - T_m)^2 + a_3(T - T_m)^3 \tag{4.67}$$

gave a good fit to the data for each property. In some cases a cubic term was not even needed. The coefficients as well as the values of X_m for $T_m = 40°C$ are given in Table 4.2.

For the glycerol case, the dramatic change of viscosity with tempera-

X	X_m	a_1 $10^{-4}K^{-1}$	a_2 $10^{-6}K^{-2}$	a_3 $10^{-8}K^{-3}$
$\rho/10^3 kg\ m^{-3}$	0.9922	−3.736	−3.98	–
$c_p/10^3 J\ kg^{-1}K^{-1}$	4.1690	0.084	4.60	–
$\beta/10^{-4}K^{-1}$	3.8810	195.0	−159.8	207
$\Lambda/W m^{-1}K^{-1}$	0.6297	21.99	−17.8	–
$\kappa/10^{-6}m^2s^{-1}$	0.1528	23.52	−14.9	–
$\nu/10^{-6}m^2s^{-1}$	0.6690	−175.9	295.8	−460
Pr	4.3820	−197.6	370	−618

Table 4.2: The values of X_m at $T_m = 40°C$ of several properties X of water and the coefficients obtained by fitting the polynomial eq. (4.67) to data over the range $10 < T < 70°C$.

ture (as shown in Fig. 4.23) required a fifth-order polynomial

$$\frac{X - X_m}{X_m} = a_1(T - T_m) + a_2(T - T_m)^2 + a_3(T - T_m)^3 + a_4(T - T_m)^4 + a_5(T - T_m)^5. \quad (4.68)$$

The coefficients as well as the values of X_m for $T_m = 40°C$ are given in Table 4.3.

X	X_m	a_1 $10^{-4}K^{-1}$	a_2 $10^{-6}K^{-2}$	a_3 $10^{-8}K^{-3}$	a_4 $10^{-10}K^{-4}$	a_5 $10^{-12}K^{-5}$
ρ	1.2477	−4.789	−0.3795	–	–	–
c_p	2.5108	22.511	–	–	–	–
β	4.7893	20.639	4.664	1.0757	0.2540	–
Λ	2.9351	3.863	–	–	–	–
κ	0.0937	13.858	3.913	−0.7577	–	–
ν	238.71	−702.83	2,393.1	−6,923.0	33,131.3	−71,517.5
Pr	2,547.9	−687.68	2,325.9	−6,646.3	30,875.9	−65,996.9

Table 4.3: The values of X_m at $T_m = 40°C$ of several properties X of glycerol and the coefficients obtained by fitting the polynomial eq. (4.68) to data over the range $10 < T < 70°C$. The units are: $[\rho] = 10^3\,kg\ m^{-3}$, $[c_p] = 10^3 J\ kg^{-1}K^{-1}$, $[\beta] = 10^{-4}\,K$, $[\Lambda] = W\ m^{-1}K^{-1}$, $[\nu] = 10^{-6}m^2s^{-1}$, and $[\kappa] = 10^{-6}m^2s^{-1}$.

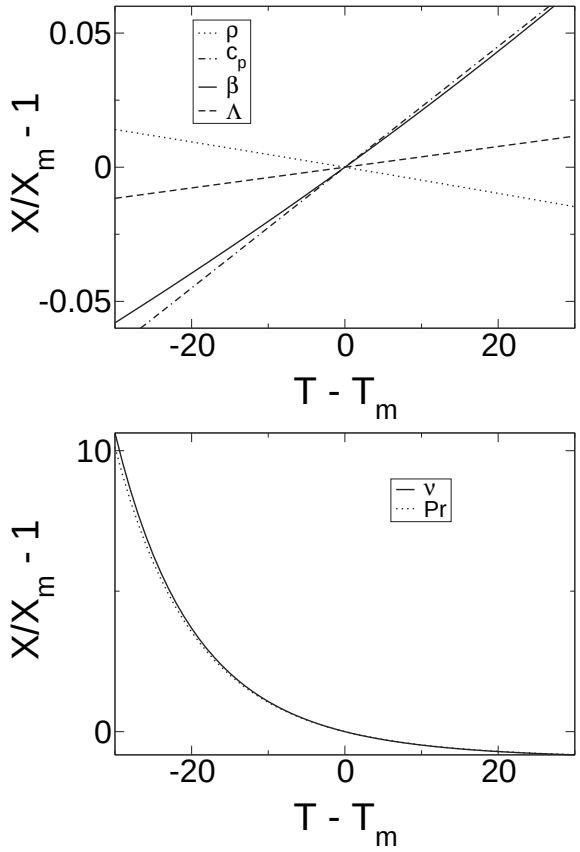

Figure 4.23: The relative deviations $(X - X_m)/X_m$ of glycerol properties X from their values X_m at T_m for $T_m = 40°C$. Upper plate: Solid line: isobaric thermal expansion coefficient β. Short dashed line: thermal conductivity Λ. Dotted line: density ρ. Double-dashed dotted line: specific heat capacity c_p. Lower plate: Solid line: kinematic viscosity ν. Dotted line: Prandtl number Pr. Note the very different scales in the upper and lower plates.

References

[1] A. OBERBECK, Über die Wärmeleitung der Flüssigkeiten bei Berücksichtigung der Strömungen infolge von Temperaturdifferenzen, *Ann. Phys. Chem.* **7**, 271 (1879).

[2] J. BOUSSINESQ, *Theorie analytique de la chaleur, Vol. 2,* Gauthier-

Villars, Paris, 1903.

[3] X. Z. WU and A. LIBCHABER, Non-Boussinesq effects in free thermal convection, *Phys. Rev. A* **43**, 2833 (1991).

[4] J. ZHANG, S. CHILDRESS, and A. LIBCHABER, Non-Boussinesq effect: Thermal convection with broken symmetry, *Phys. Fluids* **9**, 1034 (1997).

[5] R. H. KRAICHNAN, Turbulent thermal convection at arbritrary Prandtl number, *Phys. Fluids* **5**, 1374 (1962).

[6] X. CHAVANNE, F. CHILLA, B. CASTAING, B. HEBRAL, B. CHABAUD, and J. CHAUSSY, Observation of the ultimate regime in Rayleigh-Bénard convection, *Phys. Rev. Lett.* **79**, 3648 (1997).

[7] X. CHAVANNE, F. CHILLA, B. CHABAUD, B. CASTAING, and B. HEBRAL, Turbulent Rayleigh-Bénard convection in gaseous and liquid He, *Phys. Fluids* **13**, 1300 (2001).

[8] J. NIEMELA, L. SKREBEK, K. R. SREENIVASAN, and R. DONNELLY, Turbulent convection at very high Rayleigh numbers, *Nature* **404**, 837 (2000).

[9] J. NIEMELA, L. SKRBEK, K. R. SREENIVASAN, and R. J. DONNELLY, The wind in confined thermal turbulence, *J. Fluid Mech.* **449**, 169 (2001).

[10] P. E. ROCHE, B. CASTAING, B. CHABAUD, and B. HEBRAL, Observation of the 1/2 power law in Rayleigh-Bénard convection, *Phys. Rev. E* **63**, 045303 (2001).

[11] P. E. ROCHE, B. CASTAING, B. CHABAUD, and B. HEBRAL, Prandtl and Rayleigh numbers dependences in Rayleigh-Bénard convection, *Europhys. Lett.* **58**, 693 (2002).

[12] J. NIEMELA and K. R. SREENIVASAN, Confined turbulent convection, *J. Fluid Mech.* **481**, 355 (2003).

[13] S. ASHKENAZI and V. STEINBERG, High Rayleigh number turbulent convection in a gas near the gas-liquid critical point, *Phys. Rev. Lett.* **83**, 3641 (1999).

[14] F. H. BUSSE, The stability of finite amplitude cellular convection and its relation to an extremum principle, *J. Fluid Mech.* **30**, 625 (1967).

[15] C. HOARD, C. ROBERTSON, and A. ACRIVOS, Experiments on the cellular structure in Bénard convection, *Int. J. Heat Mass Transfer* **13**, 849 (1970).

[16] G. AHLERS, Effect of departures from the Oberbeck-Boussinesq approximation on the heat transport of horizontal convecting fluid layers, *J. Fluid Mech.* **98**, 137 (1980).

[17] R. W. WALDEN and G. AHLERS, Non-Boussinesq and penetrative convection in a cylindrical cell, *J. Fluid Mech.* **109**, 89 (1981).

[18] S. CILIBERTO, E. PAMPALONI, and C. PEREZ-GARCIA, Competition between different symmetries in convective patterns, *Phys. Rev. Lett.* **61**, 1198 (1988).

[19] E. BODENSCHATZ, J. DEBRUYN, G. AHLERS, and D. CANNELL, Transition between patterns in thermal convection, *Phys. Rev. Lett.* **67**, 3078 (1991).

[20] E. PAMPALONI, C. PEREZ-GARCIA, L. ALBAVETTI, and S. CILIBERTO, Transition from hexagons to rolls in convection in fluids under non-Boussinesq conditions, *J. Fluid Mech.* **234**, 393 (1992).

[21] E. BODENSCHATZ, W. PESCH, and G. AHLERS, Recent developments in Rayleigh-Bénard convection, *Ann. Rev. Fluid Mech.* **32**, 709 (2000).

[22] A. FURUKAWA and A. ONUKI, Convective heat transport in compressible fluids, *Phys. Rev. E* **66**, 016302 (2002).

[23] M. GITTERMAN, Hydrodynamics of fluids near a critical point, *Rev. Mod. Phys.* **50**, 85 (1978).

[24] L. D. LANDAU and E. M. LIFSHITZ, *Fluid Mechanics*, Pergamon Press, Oxford, 1987.

[25] M. GITTERMAN and V. STEINBERG, Criteria of occurrence of free convection in a compressible viscous heat-conducting fluid, *J. Appl. Math. Mech. (USSR)* **34**, 305 (1971).

[26] A. KOGAN and H. MEYER, Heat transfer and convection onset in a compressible fluid: ^{3}He near the critical point, *Phys. Rev. E* **63**, 056310:1 (2001).

[27] L. PRANDTL, *Über Flüssigkeitsbewegung bei sehr kleiner Reibung*, pp. 484–491, Teubner, Leipzig, 1905.

[28] H. BLASIUS, Grenzschichten in Flüssigkeiten mit kleiner Reibung, *Z. Math. Phys.* **56**, 1 (1908).

[29] S. GROSSMANN and D. LOHSE, Prandtl and Rayleigh number dependence of the Reynolds number in turbulent thermal convection, *Phys. Rev. E* **66**, 016305 (2002).

[30] X. L. QIU and P. TONG, Onset of coherent oscillations in turbulent Rayleigh-Bénard convection, *Phys. Rev. Lett* **87**, 094501 (2001).

[31] D. MEKSYN, *New Methods in Laminar Boundary Layer Theory*, Pergamon Press, Oxford, 1961.

[32] H. SCHLICHTING and K. GERSTEN, *Boundary layer theory*, Springer Verlag, Berlin, 8th edition, 2000.

[33] S. GROSSMANN and D. LOHSE, Fluctuations in turbulent Rayleigh-Bénard convection: The role of plumes, *Phys. Fluids* **16**, 4462 (2004).

[34] X. L. QIU and P. TONG, Large scale velocity structures in turbulent thermal convection, *Phys. Rev. E* **64**, 036304 (2001).

[35] F. CHILLÀ, M. RASTELLO, S. CHAUMAT, and B. CASTAING, Long relaxation times and tilt sensitivity in Rayleigh-Bénard turbulence, *Euro. Phys. J. B* **40**, 223 (2004).

[36] E. BROWN, D. FUNFSCHILLING, A. NIKOLAENKO, and G. AHLERS, Heat transport by turbulent Rayleigh-Bénard convection: Effect of finite top- and bottom conductivity, *Phys. Fluids* **17**, 075108 (2005).

[37] E. BROWN, D. FUNFSCHILLING, A. NIKOLAENKO, and G. AHLERS, Reynolds numbers of the large-scale flow in turbulent Rayleigh-Bénard convection, *unpublished* (2006).

[38] S. CHAUMAT, B. CASTAING, and F. CHILLA, Rayleigh-Bénard cells: influence of plate properties, in *Advances in Turbulence IX*, edited by I. P. CASTRO and P. E. HANCOCK, Barcelona, 2002, International Center for Numerical Methods in Engineering, CIMNE.

[39] R. VERZICCO, Effect of non-perfect thermal sources in turbulent thermal convection, *Phys. Fluids* **16**, 1965 (2004).

[40] D. FUNFSCHILING, E. BROWN, A. NIKOLAENKO, and G. AHLERS, Heat transport by turbulent Rayleigh-Bénard convection in cylindrical cells with aspect ratio one and larger, *J. Fluid Mech.* **536**, 145 (2005).

[41] G. AHLERS, Effect of sidewall conductance on heat-transport measurements for turbulent Rayleigh-Bénard convection, *Phys. Rev. E* **63**, 015303 (2000).

[42] R. VERZICCO, Sidewall finite conductivity effects in confined turbulent thermal convection, *J. Fluid Mech.* **473**, 201 (2002).

[43] D. FUNFSCHILLING, E. BROWN, A. NIKOLAENKO, and G. AHLERS, Heat transport by turbulent Rayleigh-Bénard convection in cylindrical cells with aspect ratio one and larger, *J. Fluid Mech.* **536**, 145 (2005).

[44] B. I. SHRAIMAN and E. D. SIGGIA, Heat transport in high-Rayleigh number convection, *Phys. Rev. A* **42**, 3650 (1990).

[45] C. SUN, K. Q. XIA, and P. TONG, Three-dimensional flow structures and dynamics of turbulent thermal convection in a cylindrical cell, *Phys. Rev. E* **72**, 026302 (2005).

[46] B. CASTAING, G. GUNARATNE, F. HESLOT, L. KADANOFF, A. LIBCHABER, S. THOMAE, X. Z. WU, S. ZALESKI, and G. ZANETTI, Scaling of hard thermal turbulence in Rayleigh-Bénard convection, *J. Fluid Mech.* **204**, 1 (1989).

[47] S. GROSSMANN and D. LOHSE, Scaling in thermal convection: A unifying view, *J. Fluid. Mech.* **407**, 27 (2000).

[48] S. GROSSMANN and D. LOHSE, Thermal convection for large Prandtl number, *Phys. Rev. Lett.* **86**, 3316 (2001).

[49] X. XU, K. M. S. BAJAJ, and G. AHLERS, Heat transport in turbulent Rayleigh-Bénard convection, *Phys. Rev. Lett.* **84**, 4357 (2000).

[50] K. POHLHAUSEN, Zur nährungsweisen Integration der Differentialgleichung der laminaren Grenzschicht, *Z. Angew. Math. Mech.* **1**, 252 (1921).

[51] J. E. PLAPP, *Laminar free convection with variable fluid properties*, PhD thesis, Caltech, 1957, Available at http://resolver.caltech.edu/CaltechETD:etd-09142004-153230.

[52] D. P. WALL and S. K. WILSON, The linear stability of flat-plate boundary-layer flow of fluid with temperature-dependent viscosity, *Phys. Fluids* **9**, 2885 (1997).

[53] W. PRESS, S. TEUKOLSKY, W. VETTERLING, and B. FLANNERY, *Numerical Recipes*, Cambridge University Press, Cambridge, 1986.

[54] J. OH, J. M. ORTIZ DE ZÁRATE, J. V. SENGERS, and G. AHLERS, Dynamics of fluctuations in a fluid below the onset of Rayleigh-Bénard convection, *Phys. Rev. E* **69**, 021106 (2004).

5

Non-Oberbeck-Boussinesq effects in gaseous ethane*

Non-Oberbeck-Boussinesq (NOB) effects are measured experimentally and calculated theoretically for strongly turbulent Rayleigh-Bénard convection of *gaseous ethane* under pressure where the material properties strongly depend on the temperature. Relative to the Oberbeck-Boussinesq case we find a *decrease* of the central temperature as compared to the arithmetic mean of the top- and bottom-plate temperature and an *increase* of the Nusselt number. Both effects are of opposite sign and greater magnitude than those for NOB convection in *liquids* like water [1].

5.1 Introduction

Turbulent convection in a fluid heated from below and cooled from above (Rayleigh-Bénard convection) is an important model system in fluid dynamics [2]. The induced temperature difference Δ across a sample is represented by the Rayleigh number $\mathrm{Ra} = \beta g L^3 \Delta/(\kappa\nu)$ (β is the thermal expansion coefficient, g the acceleration of gravity, L the sample height, κ the thermal diffusivity, and ν the kinematic viscosity). The problem usually is analyzed within an approximation due to Oberbeck [3] and Boussinesq [4] (OB), where it is assumed that all fluid properties are constant within the entire sample except for the density where it induces the buoy-

*Published as: G. Ahlers, F. Fontenele Araujo, D. Funfschilling, S. Grossmann, D. Lohse. Non-Oberbeck-Boussinesq effects in gaseous Rayleigh-Bénard convection, *Phys. Rev. Lett.* **98**, 054501, (2007). F.F.A. is responsible for section 5.2.2.

ancy force. Here we address, both experimentally and theoretically, the nature of deviations from this approximation.

A central aspect of this system is an understanding of boundary layers (BLs) near the top and bottom walls. At modest Ra they remain laminar while the fluid interior is turbulent, and their instabilities impact the Nusselt number Nu. At much larger Ra it was suggested [7–9] that the BLs become turbulent as well, that they then no longer influence Nu, and that an asymptotic ("ultimate" or "Kraichnan") regime is achieved where $Nu \sim Ra^{1/2}$. In the present chapter we show, by comparing theoretical calculations with new experimental measurements, that the laminar BLs are also significantly influenced by non-Oberbeck-Boussinesq (NOB) effects. These effects can be described well by an extension of the Prandtl-Blasius boundary-layer theory [10, 11].

Though NOB effects in turbulent Rayleigh-Bénard convection were measured already 15 years ago [12, 13], a quantitative comparison between OB and NOB convection was only done recently [1]. However, such study was restricted to NOB effects in *liquids* like water and glycerol. It found a *decrease* of Nu and an *increase* of the center temperature T_c as compared to the OB case. The latter could be explained quantitatively by an extension of the Prandtl-Blasius BL theory [1]. Extending this theory to *gases* is considerably more challenging, as then also the density depends on temperature (beyond the OB dependence), leading to a density boundary layer. Moreover, all material properties such as the thermal conductivity λ, the shear viscosity η, the thermal expansivity β, and the specific heat c_p depend on both temperature and density. Here we shall show that nevertheless an extension of the Prandtl-Blasius BL theory is possible.

For ethane gas close to its critical point both our theory and experiment show that the NOB effects on T_c are much larger and *opposite* to those for liquids: We observe a considerable *decrease* of T_c as compared to the OB case. Experiment moreover reveals that also the effect on Nu is stronger and opposite to that in liquids: Nu_{NOB} is *larger* than Nu_{OB}.

5.2 Center temperature

5.2.1 Experiments

The experiments were done with a cylindrical sample of height $L = 7.62$ cm and aspect ratio $\Gamma \equiv D/L = 0.999 \pm 0.002$ (D is the sample diameter).

The cell had copper top and bottom plates and a high-tensile-strength steel side wall. We used various values of $\Delta \equiv T_b - T_t$ (T_b and T_t are the bottom- and top-plate temperatures respectively) at a mean temperature $T_m \equiv (T_b + T_t)/2 = 39.98°C$. Measurements were made at various pressures P_m that were held constant to ± 1 mBar. The temperature T_t was always kept larger than the condensation temperature or the temperature corresponding to the critical isochore (see figure 5.1). For a given P_m the values of Δ then determined Ra, which was evaluated from properties at T_m. The center temperature T_c was deduced from eight thermometers at uniformly distributed azimuthal locations on the outside of the side wall at half-height of the cell; see refs. [6, 14] for details.

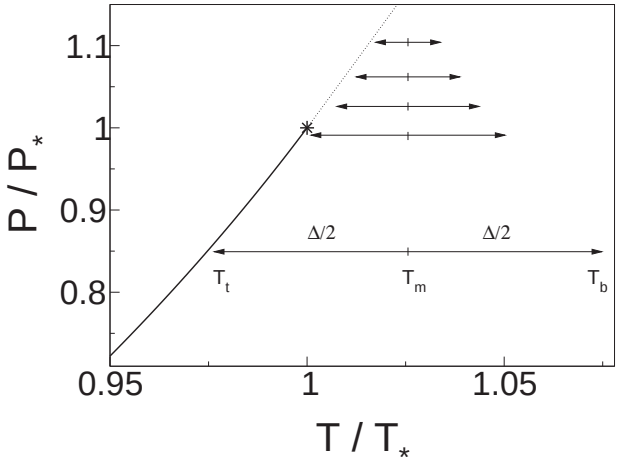

Figure 5.1: Pressure-temperature plane in reduced units. Star: critical point of ethane ($T_* = 32.18°C$, $P_* = 48.718$ bars). Heavy line: liquid-vapor coexistence curve. Dotted line: critical isochore. The horizontal arrows show the maximum temperature intervals Δ, centered about $T_m = 39.98°C$, that were used at each of the pressures $P_m/P_* = 0.849$, 0.991, 1.026, 1.062, and 1.104 (bottom to top).

The results for $T_c - T_m$ as function of Δ for various P_m are presented in figure 5.2a. Clearly, in all cases the center temperature is smaller than the arithmetic mean T_m of T_b and T_t, signaling a breaking of the top-bottom symmetry. Assuming that the time-averaged temperature in the bulk is constant with height, i.e., that the sum $\Delta_b + \Delta_t$ of the temperature drops over the bottom and the top BL equals Δ, this result can be expressed as $\chi = \Delta_b/\Delta_t$, see fig. 5.2b. Deviations from $\chi = 1$ signal NOB effects on

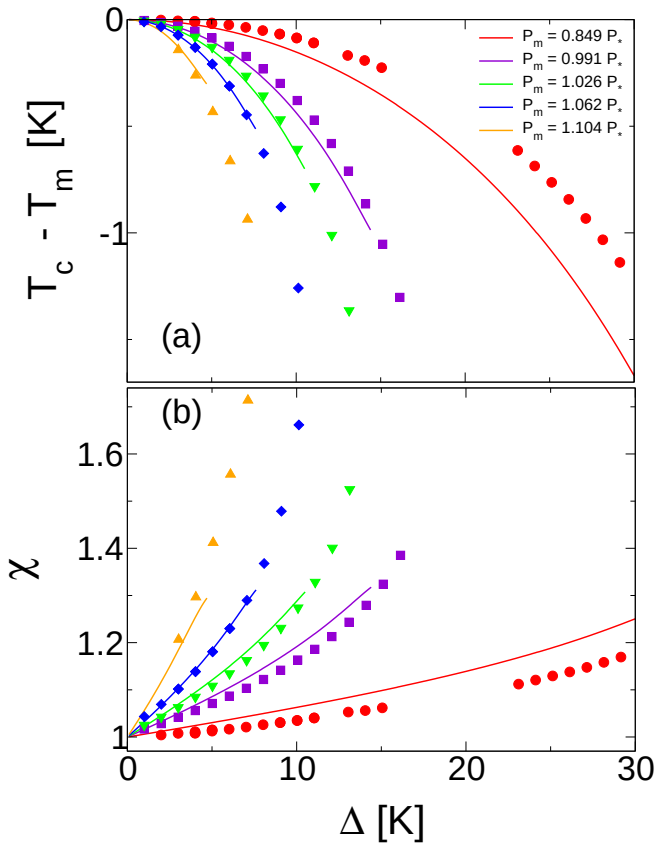

Figure 5.2: (a) Deviation $T_c - T_m$ of the center temperature T_c from T_m as function of Δ and (b) resulting ratio $\chi = \Delta_b/\Delta_t$ of the temperature drops across the bottom and the top boundary layers. Symbols: experiment. Lines: theory. As in fig. 5.1, the pressure P_m ranges from 0.849 P_* to 1.104 P_*.

T_c. Note that in the present case for ethane we not only have $\chi > 1$ as compared to $\chi < 1$ for liquids, but also that the modulus of the relative deviation from one is much larger than in the water case, i.e., NOB effects on the center temperature are opposite and much stronger in ethane as compared to the liquids analyzed in ref. [1].

5.2.2 Theory

The lines shown in fig. 5.2 are obtained by an extension of the BL theory of ref. [1], which now involves the density field ρ in addition to those of temperature T and velocity $\mathbf{u}$. In the spirit of Prandtl-Blasius theory, such fields are assumed to be stationary and only dependent on the longitudinal x and the transversal z coordinates. As shown below, this kind of BL approach reasonably describes $\rho(x,z)$, $T(x,z)$, $u_x(x,z)$, and $u_z(x,z)$.

In Prandtl's approximation, mass and momentum conservation can be expressed as:

$$\partial_x\{\rho u_x\} + \partial_z\{\rho u_z\} = 0, \tag{5.1}$$

$$\rho\,\{u_x\,\partial_x u_x + u_z\,\partial_z u_x\} = \partial_z\{\eta\,\partial_z u_x\}, \tag{5.2}$$

with the boundary conditons $u_x(x,0) = 0$, $u_z(x,0) = 0$, and $u_x(x,\infty) = U_{NOB}$. Here, U_{NOB} is the typical large-scale wind velocity [9]. From energy conservation, one can derive the following equation for the temperature field [15, 16]:

$$u_x\,\partial_x T + u_z\,\partial_z T + \frac{\gamma-1}{\beta}\{\partial_x u_x + \partial_z u_z\} = \frac{\gamma}{\rho\,c_P}\partial_z\{\Lambda\,\partial_z T\}, \tag{5.3}$$

where $\gamma = c_P/c_V$ and the boundary conditions are $T(x,0) = T_{b,t}$, $T(x,\infty) = T_c$. Just as in ref. [1], the BLs are coupled by the condition that the heat fluxes $Q_{b,t}$ through the top and bottom BLs must be equal:

$$Q_b = -\Lambda_b\,\partial_z T|_b = -\Lambda_t\,\partial_z T|_t = Q_t. \tag{5.4}$$

Equations (5.1)–(5.4) with the corresponding boundary conditions must be solved self-consistently. The dependences of the material properties such as η, Λ, c_P, and β on temperature and density are taken from ref. [17], see figure 5.3.

As in Prandtl's theory, the system of partial differential equations (5.1)–(5.3) can be reduced to ordinary differential equations (ODEs) through a stream function Ψ:

$$\tilde{\rho}\,u_x = \partial_z\Psi, \qquad \tilde{\rho}\,u_z = -\partial_x\Psi. \tag{5.5}$$

where $\tilde{\rho} \equiv \rho/\rho_m$ is the density nondimensionalized with $\rho_m = \rho(T_m, P_m)$. Since the continuity equation is automatically fulfilled by (5.5), we may introduce a self-similarity variable $\tilde{Z} \equiv z/\ell_{NOB}(x)$ and a similarity function $\tilde{\Psi}(\tilde{Z}) = \Psi(x,z)/(\ell_{NOB}\, U_{NOB})$, such that $\ell_{NOB}(x) = \sqrt{x\nu_m/U_{NOB}}$. Thus, the velocity components are:

$$u_x = U_{NOB}\,\frac{\tilde{\Psi}'}{\tilde{\rho}}, \qquad u_z = \frac{\nu_m}{2\ell_{NOB}}\left\{\tilde{Z}\,\frac{\tilde{\Psi}'}{\tilde{\rho}} - \frac{\tilde{\Psi}}{\tilde{\rho}}\right\}, \tag{5.6}$$

with boundary conditions $\tilde{\Psi}(0) = 0 = \tilde{\Psi}'(0)$ and $\tilde{\Psi}'(\infty) = \tilde{\rho}_c$.

In terms of (5.6), the viscous BL equation (5.2) can be written as:

$$\begin{aligned}\tilde{\eta}\tilde{\Psi}''' &+ \left\{\frac{1}{2}\tilde{\Psi} + \tilde{\eta}' - 2\frac{\tilde{\rho}'}{\tilde{\rho}}\,\tilde{\eta}\right\}\tilde{\Psi}'' \\ + &\left\{-\frac{1}{2}\frac{\tilde{\rho}'}{\tilde{\rho}}\tilde{\Psi} + \left[2\left(\frac{\tilde{\rho}'}{\tilde{\rho}}\right)^2 - \frac{\tilde{\rho}''}{\tilde{\rho}}\right]\tilde{\eta} - \frac{\tilde{\rho}'}{\tilde{\rho}}\tilde{\eta}'\right\}\tilde{\Psi}' = 0. \end{aligned} \tag{5.7}$$

Here, $\tilde{\eta} \equiv \eta/\eta_m$ is the dimensionless viscosity. Its gradient $\tilde{\eta}'$ is given by:

$$\tilde{\eta}' = \left(\frac{\partial\tilde{\eta}}{\partial\tilde{\Theta}}\right)_{\tilde{\rho}}\tilde{\Theta}' + \left(\frac{\partial\tilde{\eta}}{\partial\tilde{\rho}}\right)_{\tilde{\Theta}}\tilde{\rho}',$$

where $\tilde{\Theta} \equiv (T - T_t)/\Delta$ is the dimensionless temperature.

Next, assuming that the pressure is constant at P_m throughout the fluid, equation (5.1) leads to [15]:

$$\tilde{\rho}' = -\tilde{\rho}\,\tilde{\beta}\,\tilde{\Theta}', \tag{5.8}$$

with $\tilde{\beta} \equiv \beta\,\Delta$. The boundary conditions are $\tilde{\rho}(0) = \tilde{\rho}_{b,t}$, $\tilde{\rho}(\infty) = \tilde{\rho}_c$, and $\tilde{\rho}'(0) = -\tilde{\rho}_{b,t}\,\tilde{\beta}_{b,t}\,\tilde{\Theta}'_{b,t}$.

Finally, we also write the temperature equation (5.3) in self-similar form as [15]:

$$\tilde{\Lambda}\tilde{\Theta}'' + \left\{\frac{1}{2}\tilde{c}_P\,Pr\,\tilde{\Psi} + \tilde{\Lambda}'\right\}\tilde{\Theta}' = 0, \tag{5.9}$$

where $\tilde{\Lambda} \equiv \Lambda/\Lambda_m$ and $\tilde{c}_P \equiv c_P/c_{P,m}$. Equation (5.9) is subject to $\tilde{\Theta}(0) = \tilde{\Theta}_{b,t}$ and $\tilde{\Theta}(\infty) = \tilde{\Theta}_c$.

The three coupled ODEs (5.7), (5.8), and (5.9) with the respective boundary conditions and the heat-flux conservation (5.4) are solved numerically with a shooting method [15]. The integration domain is defined with the same values of T_m and P_m as those used in the experiments, but

restricted to Δ-ranges where the material properties are convex. There are no free fit parameters. As shown in fig. 5.2, the agreement between theory and experiment is reasonable, in particular for the pressures larger than P_*. Further theoretical results, such as temperature and density profiles, will be presented elsewhere [15].

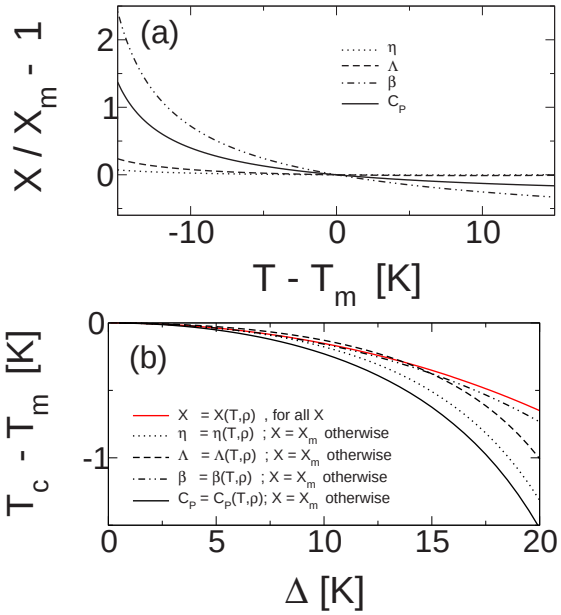

Figure 5.3: (a) Relative deviations $(X-X_m)/X_m$ of ethane properties from their values X_m at $T_m = 40^oC$ and $P_m = 0.849P_*$. The curves are based on ref. [17]. (b) Predicted $T_c - T_m$ for hypothetical gases, with one of the material parameters varying as function of temperature and all others fixed at their values X_m at $T_m = 40°C$ and $P_m = 0.849P_*$.

What material property is the main origin of the decreased T_c? To find out, we recalculated T_c for various hypothetical gases, with all material properties constant as in the OB case and evaluated at $T_m = 40°C$ except for one. The one temperature-dependent property has the same temperature dependence as ethane at $P/P_* = 0.849$. The result is shown in figure 5.3b. Remarkably, every individual temperature dependence is already strong enough to produce a NOB deviation of T_c of a size that is comparable to the full NOB effect, reflecting the complicated nonlinear dependence of T_c on the material properties and the nonlinear dependence of the material properties on temperature (Fig. 5.3a). However, we think that the center-temperature reduction observed here is a more general feature

for gases as compared to the center temperature increase in liquids [1]: In liquids $(\partial\eta/\partial T)_p < 0$ leads to a thinner bottom viscous BL in the NOB case as compared to the OB case. This thinner bottom viscous BL induces also a thinner thermal BL between the center and the hot bottom plate, implying an enhanced center temperature. For gases however the bottom viscous BL expands due to the temperature dependence of the density, inducing also an extension of the thermal BL between the hot bottom and the center, thus implying a larger temperature drop across that BL, i.e., a reduced center temperature.

5.3 Nusselt number

At present we do not have a theory for NOB effects on Nu. However, we show some experimental results in Fig. 5.4a as a function of Ra on logarithmic scales. In addition, a large number of data points with relatively small Δ and $\beta\Delta \leqslant 0.05$ were obtained over a wide range of T_m and P_m. They served as an experimental estimate of Nu_{OB} that could be represented well by $Nu_{OB} = 0.1826 Ra^{0.292}$ [†]. This is shown as a dotted line in Fig. 5.4a. Particularly at the highest pressure one sees substantial deviations of the data from the dotted line, which we interpret as strong NOB effects. The deviations become more clear in Fig. 5.4b, where the ratio Nu_{NOB}/Nu_{OB} is shown. In contrast to the measurements for water [1], where NOB effects caused a *decrease*, albeit by only a percent or so, one sees in Fig. 5.4b that NOB effects *increase* Nu by as much as 20% in the ethane case.

Although the temperature dependence of all properties seems to contribute significantly to the NOB effects, it is of interest to see whether one of them could be chosen as a surrogate to represent the effect of all in an empirical manner. To this end we plotted the data as a function of $\beta\Delta$ in Fig. 5.4c. One sees that the three data sets are nearly, but not completely, collapsed onto a single curve that can be represented by $Nu_{NOB}/Nu_{OB} = 1 + 0.125(\beta\Delta) + 1.012(\beta\Delta)^2 + 1.150(\beta\Delta)^3$. This representation is shown as solid lines in both Fig. 5.4b and c. Although not a perfect fit, it does seem to serve as a useful estimate of the approximate size of NOB effects on Nu in gases. From this analysis we conclude, for

[†]We note that this result may be affected, to the extent of a few percent, by the nonlinear influence of the side wall on the heat transport [18, 19]; only the conductance of the empty cell was subtracted. However, the side wall should not affect Nu_{NOB}/Nu_{OB} very much because its influence will, to a very large extent, cancel in the ratio.

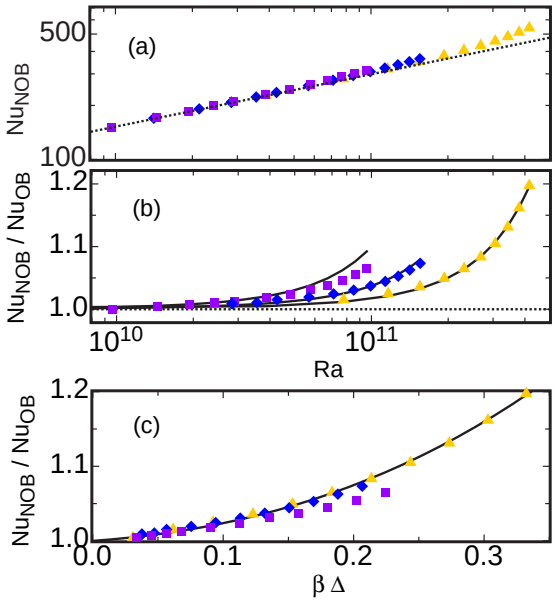

Figure 5.4: (a): Nu_{NOB} and (b): Nu_{NOB}/Nu_{OB} as function of Ra for $P/P_* = 1.104$ (triangles), 1.062 (diamonds), and 0.991 (squares). (c): Nu_{NOB}/Nu_{OB} as a function of $\beta\Delta$. Dotted lines: $Nu_{OB} = 0.1826Ra^{0.292}$. Solid lines: $Nu_{NOB}/Nu_{OB} = 1 + 0.125(\beta\Delta) + 1.012(\beta\Delta)^2 + 1.150(\beta\Delta)^3$.

instance, that Nu_{NOB} will differ from Nu_{OB} by about 3 % or less when $\beta\Delta$ is about 0.1 or less.

5.4 Conclusion

In this chapter we presented experimental data, and theoretical calculations based on an extension of the Prandtl-Blasius boundary-layer theory, for the center temperature T_c of a turbulent Rayleigh-Bénard sample under non-Oberbeck-Boussinesq (NOB) conditions. Theory and experiment agree remarkably well without the need for any adjustable parameters. We also presented new measurements of the Nusselt number Nu under NOB conditions and found strong positive deviations from the OB case. The deviations could be represented empirically by a simple function of the relative density difference $\beta\Delta$ across the sample. This function makes it possible to estimate approximately the size of deviations from

the OB case for other data. In particular, it suggests that the relatively rapid rise of Nu with Ra observed by Chavanne et al. [20] (which was interpreted by those authors as evidence for the “ultimate" regime) probably cannot be attributed to NOB effects.

Acknowledgments

The work at Santa Barbara was supported by the US National Science Foundation through Grant DMR02-43336. This work is part of the research programme of the Stichting voor Fundamenteel Onderzoek der Materie (FOM), which is financially supported by the Nederlandse Organisatie voor Wetenschappelijk Onderzoek (NWO).

References

[1] G. AHLERS, E. BROWN, F. FONTENELE ARAUJO, D. FUNFSCHILLING, S. GROSSMANN, and D. LOHSE, Non-Oberbeck-Boussinesq effects in strongly turbulent Rayleigh-Bénard convection, *J. Fluid Mech.* **569**, 409 (2006).

[2] L. P. KADANOFF, Turbulent heat flow: Structures and scaling, *Phys. Today* **54**, 34 (2001).

[3] A. OBERBECK, Über die Wärmeleitung der Flüssigkeiten bei Berücksichtigung der Strömungen infolge von Temperaturdifferenzen, *Ann. Phys. Chem.* **7**, 271 (1879).

[4] J. BOUSSINESQ, *Theorie analytique de la chaleur, Vol. 2,* Gauthier-Villars, Paris, 1903.

[5] S. CILIBERTO, S. CIONI, and C. LAROCHE, Large-scale flow properties of turbulent thermal convection, *Phys. Rev. E* **54**, R5901 (1996).

[6] G. AHLERS, E. BROWN, and A. NIKOLAENKO, The search for slow transients, and the effect of imperfect vertical alignment, in turbulent Rayleigh-Benard convection, *J. Fluid Mech.* **557**, 347 (2006).

[7] R. H. KRAICHNAN, Turbulent thermal convection at arbritrary Prandtl number, *Phys. Fluids* **5**, 1374 (1962).

[8] E. A. SPIEGEL, Convection in stars, *Ann. Rev. Astron. Astrophys.* **9**, 323 (1971).

[9] S. GROSSMANN and D. LOHSE, *J. Fluid Mech.* ***407****, 27 (2000). Phys. Rev. Lett.* ***86****, 3316 (2001). Phys. Rev. E* ***66****, 016305 (2002). Phys. Fluids* ***16****, 4462* (2004).

[10] H. SCHLICHTING and K. GERSTEN, *Boundary layer theory*, Springer Verlag, Berlin, 8th edition, 2000.

[11] K. STEWARTSON, *The theory of laminar boundary layers in compressible fluids*, Oxford University Press, 1964.

[12] X. Z. WU and A. LIBCHABER, Non-Boussinesq effects in free thermal convection, *Phys. Rev. A* **43**, 2833 (1991).

[13] J. ZHANG, S. CHILDRESS, and A. LIBCHABER, Non-Boussinesq effect: Thermal convection with broken symmetry, *Phys. Fluids* **9**, 1034 (1997).

[14] E. BROWN, D. FUNFSCHILLING, A. NIKOLAENKO, and G. AHLERS, Heat transport by turbulent Rayleigh-Bénard convection: Effect of finite top- and bottom conductivity, *Phys. Fluids* **17**, 075108 (2005).

[15] F. FONTENELE ARAUJO, S. GROSSMANN, and D. LOHSE, *Phys. Rev. E* (2007), To be submitted.

[16] L. D. LANDAU and E. M. LIFSHITZ, *Fluid Mechanics*, Pergamon Press, Oxford, 1987.

[17] D. G. FRIEND, H. INGHAM, and J. F. ELY, Thermophysical properties of ethane, *J. Phys. Chem. Ref. Data* **20**, 275 (1991).

[18] G. AHLERS, Effect of sidewall conductance on heat-transport measurements for turbulent Rayleigh-Bénard convection, *Phys. Rev. E* **63**, 015303 (2000).

[19] P. ROCHE, B. CASTAING, B. CHABAUD, B. HEBRAL, and J. SOMMERIA, Side wall effects in Rayleigh Benard experiments, *Eur. Phys. J. B* **24**, 405 (2001).

[20] X. CHAVANNE, F. CHILLA, B. CASTAING, B. HEBRAL, B. CHABAUD, and J. CHAUSSY, Observation of the ultimate regime in Rayleigh-Bénard convection, *Phys. Rev. Lett.* **79**, 3648 (1997).

6
Conclusions

"Work can be useless without being pointless."
Lev Davidovich Landau*

Rayleigh-Bénard convection is a very inspiring source for studies on nonlinear dissipative systems. From the beautiful hexagons on the surface of a liquid to the awkward reorientations of a vigorously driven large-scale flow, it has stimulated major advances in the theories pattern formation, chaos, and turbulence.

The present thesis touched a specific range of Rayleigh numbers ($10^8 \leqslant \mathrm{Ra} \leqslant 10^{12}$). In particular, we attempted to answer two basic questions: (i) What is the spatiotemporal structure of the large-scale circulation? (ii) How are the momentum and thermal transports modified by variations in the properties of the fluid?

Our models for wind reversals [1] and wind oscillations [2] have the merit of being *deterministic* and pedagogically appealing. However, their predictive power is disappointing. In fact, as far as the statistical properties of the wind are concerned, stochastic models have been more successful [3, 4]. Crucial ingredients in such stochastic approaches are *noise* terms, which presumably represent the turbulent fluctuations. But the dynamics and the dependences of the turbulent fluctuations on the Rayleigh and Prandtl numbers are by themselves additional problems. From these perspectives, a self-contained theory for the spatiotemporal dynamics of the large-scale circulation remains a challenge.

As for non-Oberbeck-Boussinesq (NOB) effects [5, 6], it is remarkable that boundary-layer theory works so well. Despite the two dimensional and laminar character of our analysis, the top-down symmetry breaking of the boundary-layers is reasonably described from the quantitative point of view. However, this is just a marginal contribution. The funda-

*A. Livanova, *Landau: A Great Physicist and Teacher,* p. 21, Pergamon Press, Oxford (1980).

mental issue remains: How to predict the Reynolds and Nusselt numbers in a flow under NOB conditions ? Perhaps an extension of Grossmann-Lohse theory embodying NOB effects in the boundary layers could answer this question. But one of the major difficulties involved in such phenomelogical approach is that the NOB symmetry breaking introduces additional scales in the temperature *and* velocity profiles. It is nontrivial and unclear how to incorporate these new scales in the estimation of the thermal and viscous dissipations (which are crucial ingredients in Grossmann-Lohse theory). Considerable effort is necessary to overcome such obstacles.

Aside the challenges mentioned above, variations of the classical Rayleigh-Bénard problem also pose relevant questions. For instance: How is the turbulent heat transport changed in the presence of rotation ? And in the presence of bubbles ? Questions of this nature are still open to systematic studies.

References

[1] F. FONTENELE ARAUJO, S. GROSSMANN, and D. LOHSE, Wind reversals in turbulent Rayleigh-Bénard convection, *Phys. Rev. Lett.* **95**, 084502 (2005).

[2] C. RESAGK, R. DU PUITS, A. THESS, F. V. DOLZHANSKY, S. GROSSMANN, F. FONTENELE ARAUJO, and D. LOHSE, Oscillations of the large scale wind in turbulent thermal convection, *Phys. Fluid* **18**, 095105 (2006).

[3] E. BROWN and G. AHLERS, Large-Scale Circulation Model for Turbulent Rayleigh-Bénard Convection, *Phys. Rev. Lett.* **98**, 134501 (2007).

[4] R. BENZI, Flow Reversal in a Simple Dynamical Model of Turbulence, *Phys. Rev. Lett.* **95**, 024502 (2005).

[5] G. AHLERS, E. BROWN, F. FONTENELE ARAUJO, D. FUNFSCHILLING, S. GROSSMANN, and D. LOHSE, Non-Oberbeck-Boussinesq effects in strongly turbulent Rayleigh-Bénard convection, *J. Fluid Mech.* **569**, 409 (2006).

[6] G. AHLERS, F. FONTENELE ARAUJO, D. FUNFSCHILLING, S. GROSSMANN, and D. LOHSE, Non-Oberbeck-Boussinesq Effects in Gaseous Rayleigh-Bénard Convection, *Phys. Rev. Lett.* **98**, 054501 (2007).

Summary

Convection, from the Latin *convehere* (to carry with), is the transport of a physical quantity by coupling with a velocity field. Thermal convection, in particular, is concerned with the interplay between *heat*, *buoyancy*, and *fluid motion*. A classical example is provided by the emissions of warm rising and cold falling fluid in a container heated from below and cooled from above. Depending on the strength of the thermal driving, such emissions may even induce a *large-scale circulation* of fluid. Some basic questions arising in this scenario are: How irregular is the spatiotemporal dynamics of the large-scale circulation? Does it exhibit any trace of long memory? How sensitive is the flow to variations in the intrinsic properties of the fluid? Are such changes capable of breaking the top-down symmetry of the boundary-layers? These questions are addressed in the present thesis.

In chapter 2, we propose a model for the irregular cessation and subsequent reversal of the large-scale circulation (also known as the *wind*). On the basis of a force balance between buoyancy and viscous drag, we derive a dynamical system for the motion of a single plume. Chaotic wind reversals generated by the model are then characterized in terms of the velocity fluctuations and the mean frequency of reversals.

Chapter 3 is concerned with the azimuthal dynamics of the wind. Starting from the inviscid hydrodynamic equations, we introduce phenomenological terms representing viscous dissipation and thermal forcing (boundary-layer and plume contributions are not included). Then, by numerically solving the extended equations of motion, we show that: (i) the wind azimuthally oscillates with a time scale comparable to the large eddy turnover time, and (ii) the azimuthal angle has a long memory that lasts for hundreds of eddy turnover times.

Chapters 4 and 5 are devoted to flows in which the strength of thermal driving induces changes in the properties of the fluid. On the basis of boundary-layer equations with *variable transport coefficients*, we show that the top-down symmetries of the velocity, temperature, and density profiles are broken. Two different fluids are considered: water (chapter 4) and gaseous ethane under high pressure (chapter 5). The latter exhibits a more pronounced and opposite symmetry breaking as compared to the former. In both cases, our theoretical results are in reasonable agreement with experimental measurements.

Finally, chapter 6 addresses our general conclusions, including shortcomings of our methods and questions that remain open.

Samenvatting

Convectie, van het latijnse woord *convehere* (meedragen), is het transport van een fysische grootheid door middel van een snelheidsveld. Thermische convectie, in het bijzonder, bestaat uit de interactie tussen warmte, buoyancy en vloeistofstroming. Een klassiek voorbeeld is het opstijgen van warme, en het dalen van koele vloeistof in een container die verwarmd wordt van beneden en gekoeld wordt van boven. Afhankelijk van de sterkte van de thermische aansturing kan dit zelfs een globale circulatie van de vloeistof tot gevolg hebben. Enkele elementaire vragen in dit scenario zijn: Hoe onregelmatig is de plaats- en tijdsverdeling van de dynamica van de globale circulatie? Is er sprake van een lange-termijn geheugen effect? Hoe gevoelig is de stroming voor fluctuaties van de intrinsieke eigenschappen van de vloeistof? Zijn zulke veranderingen in staat tot het breken van de boven-onder symmetrie van de grenslagen? Deze vragen worden beantwoord in dit proefschrift.

In hoofdstuk 2 introduceren wij een model voor de onregelmatige, abrupte afremming van de vloeistof en de daarop volgende omkering van de globale circulatie (bekend als de *wind*). Gebaseerd op een krachtenbalans tussen de buoyancy kracht en de visceuze weerstand leiden we een dynamisch systeem af voor de beweging van een enkele plume. Chaotische omkeringen van de wind die gegenereerd worden door het model worden dan gekarakteriseerd door de snelheidsfluctuaties en de gemiddelde frequentie van de omkeringen.

Hoofdstuk 3 beschrijft de azimuthale dynamica van de wind. Uitgaande van de niet-visceuze hydrodynamische vergelijking introduceren we fenomelogische termen die visceuze dissipatie en thermische aandrijving representeren (grenslagen en plumes zijn niet meegerekend). Door het numeriek oplossen van de bewegingsvergelijking laten we zien dat: (i) de wind azimuthalisch oscilleert met een tijdsschaal vergelijkbaar met de eddy turnover tijd, en (ii) de azimuthale hoek heeft een geheugen dat bestaat gedurende honderden eddy turnover tijden.

Hoofdstuk 4 en 5 beslaan de stromingen waarvan de sterkte van de thermische aandrijving zorgt voor veranderingen van de eigenschappen van de vloeistof. Op basis van de vergelijkingen van de grenslaag met *variabele transport coefficienten* laten we zien dat de boven-onder symmetrie van de snelheid, temperatuur en dichtheidsprofielen worden verbroken. Twee verschillende vloeistoffen worden beschouwd: water (hoofdstuk 4) en ethaan in de gasfase onder hoge druk (hoofdstuk 5). Het laatste laat een meer uitgesproken en tegengestelde breking van de symmetrie zien vergeleken met het eerste. In beide gevallen zijn onze theoretische resultaten in redelijke overeenstemming met de experimentele metingen.

Tenslotte wenden we ons in hoofdstuk 6 tot de algemene conclusies, inclusief tekortkomingen van onze methoden en vragen die open blijven staan.

Acknowledgements

Learning processes are among the most fascinating and rewarding experiences that a human being can have. After all, artistic expressions such as literature, music, and science partially flourish from unsurpassed learning attitudes. Passionate musicians and scientists appreciate that, and, as *"professional students"*, they are always in pursuit of harmony, precision, clarity, elegance, and virtuosity. In the particular context of physics, graduate studies usually provide a first opportunity to learn and "play an instrument". As exciting as this can be for the Ph.D. student, such experience may sound not so "musical" for his family, friends, and (even for his) thesis advisors. But as long as the parts involved are sufficiently patient with the inharmonic melodies played over four years of research, the learning process by itself can be extremely rewarding. From this perspective, I would like to thank many distinguished people that have contributed to my human and academic developments.

First, and most of all, I would like to thank my mother Helena and my sisters Sandra and Helenice for teaching me exemplary lessons of *integrity*, *compassion*, and *perseverance*. Such core values have definitely shaped my personality and words cannot describe how grateful I am for the unconditional love that we have shared together. This thesis is dedicated to them.

With similar intensity, I would like to thank (in chronological order) all my academic advisors. To begin, I must say that I was very fortunate of having excellent high school teachers at Colégio Marconi. I still vividly remember the outstanding lectures on physics by Professors Evandro Melo Jr. (1993) and Francisco Mayrink Sampaio (1994–1995). They certainly inspired me to take the first steps in science. So much so that in 1996 I was admitted to the Federal University of Minas Gerais (UFMG), where I had the privilege to learn mathematics with Professor Gastão Braga (1998–2001) and theoretical physics with Professor Ronald Dickman (2001–2003). I am extremely grateful to both of them for the sincere friendship that remains between us. In the same spirit, I would like to thank Professor Detlef Lohse for giving me the opportunity to join his research group at University of Twente (2003–2007). Even today, I find quite remarkable the way by which our paths intersected. As I remember, everything began in April 2003 when I was preparing my final project for a course on *Hydrodynamic instabilities and turbulence* taught by Ron Dickman: I was supposed to select a paper, "rewrite" it, and explain all details involved in the analysis. By checking the literature, I encountered a series of relevant papers on thermal convection, turbulence, granular flows, and sonoluminescence; all of them with a common author: Detlef Lohse.

Indeed, Professor Lohse has an incredibly good taste for physical problems! I shall be always grateful for the innumerable lessons that he has taught me. Moreover, I would like to thank him for stimulating my collaboration with Professor Siegfried Grossmann. As co-advisor of my thesis, Professor Grossmann has carefully read and corrected all my notes, always providing constructive, significant, and kind suggestions. His ability to identify key physical aspects of a problem (without spending energy on technicalities) is simply impressive. For me, it has been a real honour to learn with the complementary styles of Professors Lohse and Grossmann.

So, I have been very fortunate to be part of the Physics of Fluids group. My sincerest thanks to all its members. Since the list of current and former colleagues is considerably long, I shall devote my words of gratitude to 3 individuals in particular: Joanita Leferink, Jos de Jong, and Christian Veldhuis. Joanita, for instance, has helped me to overcome many bureaucracies. Moreover, I dare to say that part of the success of the Physics of Fluids group is due to the efficiency, commitment, good mood, and care with which she manages all the administrative work. I honestly wish her all the best. Likewise, I owe a huge debt of gratitute to my officemates Jos and Christian. During office hours or dinners that we organized every once in a while, our pleasant discussions covered a broad range of subjects, always ending up in a good laugh. Many thanks to both of you.

External collaborations were also an integral part of the present thesis. In this respect, I would like to thank Professor Guenter Ahlers, Eric Brown, Dr. Denis Funfschilling, Dr. Ronald du Puits, Dr. Christian Resagk, and Professor André Thess for sharing their experimental results with us.

Finally, I would like to thank the Foundation for Fundamental Research on Matter (FOM) for the generous financial support.

Enschede, May 2007.

Francisco Fontenele Araujo Jr.

About the author

Francisco Fontenele Araujo Jr. (1978) was born in Belo Horizonte, Brazil, the son of Helena (1939) and Francisco (1939–1979), and brother of Sandra (1961) and Helenice (1959).

His basic education took place at Colégio Municipal Marconi (a school founded by Italian immigrants in the 1930s). In 1996, he was admitted to the Federal University of Minas Gerais where he earned his B.Sc. (2001) and M.Sc. (2003) degrees in theoretical Physics under the guidance of Professors Gastão Braga and Ronald Dickman, respectively. In September 2003, he was fortunate to join the Physics of Fluids group at the University of Twente, where his Ph.D. research was supervised by Professors Detlef Lohse and Siegfried Grossmann.

Apart from his passion for Physics and Mathematics, Francisco's interests encompass music (from Bach to Jobim), literature (Bertrand Russell, in particular), and volleyball (he is a loyal supporter of Minas Tênis Clube).